DOE/ID/13331-1

DILUTE OXYGEN COMBUSTION

Phase I Report

H.M. Ryan
M.F. Riley
H. Kobayashi

October 1997

Work Performed Under Contract No. DE-FC36-95ID13331

Prepared for the
U.S. Department of Energy
Assistant Secretary for
Energy Efficiency and Renewable Energy
Washington, DC

Prepared by
Praxair, Inc.
777 Old Saw Mill River Road
Tarrytown, NY 10591

DILUTE OXYGEN COMBUSTION

Phase I Report

H.M. Ryan
M.F. Riley
H. Kobayashi

October 1997

Work Performed Under Contract No. DE-FC36-95ID13331

For
U.S. Department of Energy
Assistant Secretary for
Energy Efficiency and Renewable Energy
Washington, DC

By
Praxair, Inc.
Tarrytown, NY

DISCLAIMER

This report was prepared as an account of work sponsored by an agency of the United States Government. Neither the United States Government nor any agency thereof, nor any of their employees, make any warranty, express or implied, or assumes any legal liability or responsibility for the accuracy, completeness, or usefulness of any information, apparatus, product, or process disclosed, or represents that its use would not infringe privately owned rights. Reference herein to any specific commercial product, process, or service by trade name, trademark, manufacturer, or otherwise does not necessarily constitute or imply its endorsement, recommendation, or favoring by the United States Government or any agency thereof. The views and opinions of authors expressed herein do not necessarily state or reflect those of the United States Government or any agency thereof.

DISCLAIMER

Portions of this document may be illegible electronic image products. Images are produced from the best available original document.

DILUTE OXYGEN COMBUSTION

PHASE I REPORT

December 22, 1997

Submitted to:
U.S. DOE, Idaho Operations Office
785 DOE Place
MS 1221
Idaho Falls, ID 83401-1562

Submitted by:
Praxair, Inc.
777 Old Saw Mill River Rd.
Tarrytown, NY 10591

ABSTRACT

A novel burner, in which fuel (natural gas) and oxidant (oxygen or air) are separately injected into a furnace, shows promise for achieving very low nitrogen oxide(s) (NO_x) emissions for commercial furnace applications. The dilute oxygen combustion (DOC) burner achieves very low NO_x through in-furnace dilution of the oxidant stream prior to combustion, resulting in low flame temperatures, thus inhibiting thermal NO_x production. The results of a fundamental and applied research effort on the development of the DOC burner are presented. In addition, the results of a market survey detailing the potential commercial impact of the DOC system are disclosed.

The fundamental aspects of the burner development project involved examining the flame characteristics of a natural gas turbulent jet in a high-temperature ($\sim$1366 K) oxidant (7-27% O_2 vol. wet). Specifically, the mass entrainment rate, the flame lift-off height, the velocity field and major species field of the jet were evaluated as a function of surrounding-gas temperature and composition. The measured entrainment rate of the fuel jet decreased with increasing oxygen content in the surrounding high-temperature oxidant, and was well represented by the d^+ scaling correlation found in the literature. The measured flame lift-off height decreased with increasing oxygen content and increasing temperature of the surrounding gas. An increase in surrounding-gas oxygen content and/or temperature inhibited the velocity decay within the jet periphery as a function of axial distance as compared to isothermal turbulent jets. However, the velocity measurements were only broadly represented by the d^+ scaling correlation.

Several DOC burner configurations were tested in a laboratory-scale furnace at a nominal firing rate of 185 kW ($\sim$0.63 MMBtu/h). The flue gas composition was recorded as a function of furnace nitrogen content, furnace temperature, burner geometric arrangement, firing rate, and fuel injection velocity. NO_x emissions increased with increasing furnace nitrogen content and furnace temperature, but remained relatively insensitive to variations in fuel injection velocity and firing rate. NO_x emissions below $5 \cdot 10^{-3}$ g/MJ (10 ppm-air equivalent at 3% O_2 dry) were obtained for furnace temperatures below 1533 K (2300°F) and furnace nitrogen levels between 1 and 40%. CO emissions were typically low ($<$35 ppm). Detailed in-furnace species measurements revealed the importance of the interior furnace circulation patterns, as influenced by fuel and oxidant injection schemes, on pollutant emissions. The combustion stability traits of several DOC burner arrangements were ascertained through furnace pressure measurements, with increased stability occurring as furnace temperature increased and as the separation distance between fuel and oxidant inputs decreased.

Based on current market conditions, oxy-fuel conversion of batch steel reheat furnaces with a DOC burner is justified on the basis of lower utility costs alone. However, conversion of continuous steel reheat furnaces, which are responsible for most steel production, requires additional economic incentives, such as further fuel savings, increased furnace productivity, or emission credits.

TABLE OF CONTENTS

LIST OF FIGURES

LIST OF TABLES

ACKNOWLEDGMENTS

This research was conducted with the support of the U.S. Department of Energy (DOE) Award No. DE-FC07-95ID13331. However, any opinions, findings, conclusions, or recommendations expressed herein are those of the authors and do not necessarily reflect the views of DOE. In addition, the authors would like to thank Mr. Joe Keller of the Lockheed Idaho Technologies Company, and Mr. Mark Howard and Dr. Gideon Varga of the U.S. Department of Energy for their technical advice and guidance.

Funding by Praxair, Inc. is acknowledged, and the efforts of Praxair technicians as well as the machine and fabrication shop personnel is recognized.

NOMENCLATURE

English Symbols

a	Number of moles of carbon in mole of fuel (N)
b	Number of moles of hydrogen in mole of fuel (N)
c	Sound speed (L/T)
C	Cost ($/Q or $/M)
C_p	Constant pressure specific heat (Q/M-T)
Δh_c	Fuel heat of combustion (Q/M)
d	Diameter (L)
EI	Emissions index (--)
f	Frequency (1/t)
F	Fuel consumption (Q/M)
h	Flame lift-off height (L)
i	Imaginary number
K	Specific utility cost ($/M)
l	Length (L)
L	Laboratory-scale furnace length (L)
m	Mass flow rate (M/t) or mass (M) or integer
M	Mach number (--)
MW	Molecular weight (M/N)
n	Integer
n_z	Integer
O	Specific oxygen consumption (--)
p	Pressure
P	Improvement in fuel consumption
PI	Power emission index (=EI/Δh_c) (M/Q)
Q	Firing rate (Q/t)
r	Radial coordinate (L)
$\Re_c$	Ratio of oxygen cost to fuel cost (C_{O2} /C_f)
R	Laboratory-scale furnace radius (L)
Re	Reynolds number (=Ud/ν) (--)
S	Flame speed (L/t)
t	Time (t)
T	Temperature (T)
U	Velocity (L/t)
x	Axial position in jet measured from injector exit or space coordinate (L)
X	Mole fraction (--)
Y	Mass fraction (--)
z	Radial position or space coordinate (L)

Greek Symbols

α_{mn}	Characteristic values
η	Specific heat weighted fuel mixture fraction (mole basis)

ν	Kinematic viscosity (L^2/t)
π	Pi
ρ	Density (M/L^3)
$\bar{\rho}$	Ratio of nozzle fluid density to ambient fluid density (--)
φ	Angle (--)
Φ	Fraction of furnace firing capacity converted to oxy-fuel
ω	Angular frequency (radians/t)

Subscripts

air	Air fired case
ann	Annulus
cl	Centerline
crit	Critical
e	Equivalent
eff	Effective
f	Fuel
i	Index
in	Inner
j	Jet or index
L	Laminar
max	Maximum
o	Orifice (jet)
ou	Outer
ox	Oxidant
O2	Oxy-fuel fired case
r	Radial
s	Surrounding gas
t	Total
w	Wall
z	Coordinate

Superscripts

+	Reacting case scaling

Dimension Symbols

F	Force
L	Length
M	Mass
N	Mole
Q	Heat
t	Time
T	Temperature
$	Cost

1.0 INTRODUCTION

Effective nitrogen oxide(s) (NO_x) emission control strategies are highly sought after due to strict emission standards articulated by various regulating committees. Many current NO_x control strategies attempt to limit NO_x production through the design parameters of the particular combustion device (e.g., burner) involved. A similar approach has been taken here in the development of a very low NO_x burner for commercial furnace applications. In essence, the novel technique, termed dilute oxygen combustion (DOC), involves introducing the fuel and oxidant *separately* into a furnace and achieving sufficient in-furnace dilution of the oxidant with combustion products to lead to low flame temperatures and, consequently, low NO_x.

The ideal dilute oxygen combustion (DOC) process can be envisioned to occur as follows (see Fig. 1). The oxidant is injected into the furnace and mixes with the present combustion products (e.g., CO_2, H_2O, O_2) to generate a high-temperature, dilute-oxygen ($\sim$2-10% O_2 vol. wet) atmosphere distributed uniformly throughout the furnace volume. Care is exercised in that the injected oxidant does not directly mix with the fuel which would result in high-temperature combustion. Note that the fuel and oxidant streams potentially can be injected from opposite sides of a furnace. Upon entering the furnace, the fuel jet entrains the high-temperature, dilute-oxygen furnace gas and combustion proceeds (fuel reaction zone). Since the fuel jet is reacting with a dilute-oxygen oxidant, low flame temperatures prevail, thus curtailing thermal NO_x formation. This process has similarities to flue gas recirculation (FGR) techniques; however, dilution is achieved using the natural aspirating characteristics of turbulent jets. Implementation of the DOC concept requires that the furnace gas temperature be greater than the auto-ignition temperature of the reactants to achieve a controlled combustion event Thus, heating a furnace to above the auto-ignition temperature requires a modified DOC burner arrangement.

The dilute oxygen combustion burner system has been demonstrated to a limited extent in high-temperature furnace applications and has been patented [1]. However, a more comprehensive evaluation of the DOC system is needed to augment its applicability in the commercial environment. Consequently, a fundamental and applied research effort pertaining to the DOC system has been pursued. The fundamental issues explored include the mass entrainment, the velocity and species distributions, and the flame lift-off characteristics of a fuel jet in a high-temperature oxidant. Knowledge of these quantities is needed to develop a burner design that results in very low pollutant emissions and stable combustion. In addition, several laboratory-scale furnace tests (185 kW ($\sim$0.63 MMBtu/h)) were undertaken to primarily assess the NO_x and CO emissions associated with the DOC burner. The furnace tests involved varying the burner geometric and flow characteristics, the furnace temperature and nitrogen content, and recording the effect of these variations on pollutant emissions. Further insight into the laboratory-scale combustion process was obtained through

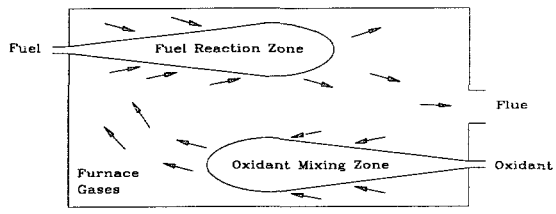

Fig. 1. Schematic diagram of the dilute oxygen combustion (DOC) concept.

detailed in-furnace species measurements and high-frequency furnace pressure measurements as a function of burner arrangement.

The primary market for the DOC burner is the steel industry, specifically batch and continuous steel reheat furnaces. The market forces necessary to convert these furnaces from air firing to oxy-fuel firing using the DOC burner were surveyed.

2.0 MARKET ASSESSMENT

This section assesses the potential market for dilute oxygen combustion (DOC) in steel reheating. Steel reheating was selected for this evaluation for two reasons. First, the steel industry in one of the largest energy consumers, and reheating is one of its largest uses. According to AISI statistics, the industry consumed $2.42 \cdot 10^{17}$ J ($2.29 \cdot 10^{14}$ Btu) of natural gas, coke oven gas, and blast furnace gas for heating and annealing in 1994 [2]. Second, steel refining processes are the largest consumers of industrial oxygen and most steel mills are supplied with a large volume of oxygen from an on-site air separation plant or from a large-scale industrial oxygen pipeline. The AISI reported an oxygen consumption of $7.19 \cdot 10^{9}$ m^3 ($2.54 \cdot 10^{11}$ ft^3) of oxygen in 1994 [3]. Thus, the industry's familiarity with the use of oxygen and the availability of relatively low-cost oxygen are expected to facilitate the application of the DOC burner in steel reheat furnaces.

2.1 Types of Furnaces

There are essentially two types of furnaces used for reheating in the steel industry, batch (or in-and-out) furnaces and continuous furnaces.

A batch furnace generally has the shape of a low, elongated box, typically 15 m long, 6 m deep, and 3 m high inside (50 ft x 20 ft x 10 ft). One long face of the furnace is the door through which the steel is charged into and removed from the furnace. Steel slabs or billets from a continuous caster or thin-section ingots are placed on the hearth floor and are heated by burners located in the short-side walls of the furnace. A flue is typically located in the center of the furnace floor. Furnace temperatures and flue gas temperatures are both typically in the range of 1200 to 1350°C (2200 - 2450°F). Batch furnaces are able to heat a variety of steel grades, lengths, and thicknesses, and so are very well suited to small special orders. Typical production rates for batch furnaces are 4.5 to 5.5 tonnes (5-6 tons) per hour.

Continuous furnaces are much larger than batch furnaces, typically 35 m long, 10 m wide, and 6 m high inside (110 ft x 30 ft x 20 ft). Steel travels through the furnace continuously along the long axis, entering through a door at one end of the furnace and exiting through a door on the opposite end. There are several methods for advancing steel through the furnace, such as pushers, walking beams, rollers, etc. [4]. Burners are arranged in several, independently controlled zones to provide a desired heating rate for the steel. Gas temperatures in the burner zones vary from 1100 to 1370°C (2000 - 2500°F). The flue is located near the charge door, so that the combustion products and the steel travel in counter-current flow. Modern continuous furnaces have a long unfired zone at the charge end that uses the sensible heat of the combustion products to preheat the cold steel entering the furnace. In this zone, the flue gas temperature can be lowered as far as 820°C (1500°F), greatly increasing the fuel efficiency of the operation. In addition, continuous furnaces have high production rates, typically 45 to 180 tonnes/hour (50 - 200 tons/hr). Because of their high productivity and fuel efficiency, these furnaces represent the vast majority of the steel reheat market.

Both types of furnace can be equipped with heat-recovery systems. Recuperators exchange heat from the flue gas to the combustion air, preheating the air to typically 200°C to 300°C (400°F - 600°F). Although a complete listing of recuperator installations is not

available, it has been estimated that roughly two-thirds of reheat furnaces have these heat-recovery systems [5].

2.2 Types of Fuel

Reheat furnaces are usually fired by either coke oven gas or natural gas.

Coke oven gas is a by-product of the manufacture of the metallurgical coke used in the iron blast furnace. Coke ovens are found in many large, integrated steel mills based on the basic oxygen furnace (BOF) for steelmaking. In 1994, the steel industry generated an estimated $8.8 \cdot 10^9$ m^3 ($3.1 \cdot 10^{11}$ ft^3) of coke oven gas, with a total heating value of $1.64 \cdot 10^{17}$ J ($1.55 \cdot 10^{14}$ Btu) [6, 7]. Table 1 lists a typical coke oven gas composition and properties [7]. Since coke oven gas is a by-product in those mills that make coke, it is the preferred fuel in those mills. When coke oven gas is available, natural gas is used only for grades, such as certain stainless steels, which react adversely with the sulfur in coke oven gas.

Table 1. Fuel Compositions and Properties

	Coke Oven Gas (typical)	Natural Gas (E. Ohio)
Composition		
Hydrogen, %	52	0.01
Methane, %	30	94
Nitrogen, %	6	1.4
Carbon Monoxide, %	6	0
Carbon Dioxide, %	2	0.7
Oxygen, %	0.5	0.01
Hydrogen Sulfide, ppm	75	---
Other, %	3.5	3.7
Net Heating Value, Btu/scf	500	935
Net Heating Value, kJ/m^3	18,600	34,800

Mills that use electric arc furnaces for steelmaking do not need coke, so they rely on natural gas for reheating. In addition, the many environmental problems and associated emission-control costs related to cokemaking [8] have led many integrated steel mills to close down coke oven batteries, reducing or eliminating coke oven gas as a fuel, and making natural gas the primary fuel for reheating furnaces. A typical natural gas composition and properties are shown for comparison in Table 1 [9].

2.3 Market Data

Table 2 is a list of steel mills operating reheat furnaces, based in part on Ref. 10. The table also lists the estimated total steel reheating capacity at each mill. Table 3 gives a summary of Table 2, showing the total number of batch and continuous furnaces.

Table 2. U.S. Reheat Furnaces

COMPANY	LOCATION	TYPE	NUMBER	CAPACITY, tph
AB Steel Mill	Cincinnati, OH	Continuous	1	30
Acme Steel Co.	Chicago, IL	Continuous	1	125
AK Steel Corporation	Middletown, OH	Continuous	4	550
American Steel & Wire Corp	Cuyahoga Hts, OH	Continuous	1	117
American Steel & Wire Corp	Joliet, IL	Continuous	1	90
Arkansas Steel Associates	Newport, AR	Continuous	1	35
Armco, Inc.	Butler, PA	Continuous	4	175
Bethlehem Steel	Burns Harbor, IN	Continuous	8	248
Bethlehem Steel	Burns Harbor, IN	Batch	4	21
Birmingham Steel Corp.	Birmingham, AL	Continuous	1	120
Birmingham Steel Corp.	Jackson, MS	Continuous	1	120
Border Steel Mills, Inc.	El Paso, TX	Continuous	1	80
BRW Steel Corp	Johnstown, PA	Continuous	1	180
Calumet Steel Co.	Chicago Heights, IL	Continuous	1	40
Carpenter Technology Corp	Reading, PA	Batch	26	40
Carpenter Technology Corp	Reading, PA	Continuous	6	96
Cascade Steel Rolling Mills, Inc.	McMinnville, OR	Continuous	2	220
Co-Steel Raritan	Perth Amboy, NJ	Continuous	1	125
Florida Steel Corp.	Charlotte, NC	Continuous	1	85
Florida Steel Corp.	Jacksonville, FL	Continuous	1	100
Florida Steel Corp.	Knoxville, TN	Continuous	1	90
Florida Steel Corp.	Jackson, TN	Continuous	1	100
Franklin Steel	Franklin, PA	Continuous	1	40
Geneva Steel	Vineyard, UT	Continuous	4	125
Georgetown Steel Corp.	Georgetown, SC	Continuous	1	120
Great Lakes Steel	Ecorse, MI	Continuous	5	250
GST Steel Co.	Kansas City, MO	Continuous	2	335
Gulf States Steel, Inc.	Gadsden, AL	Continuous	3	260
Inland Steel	E. Chicago, IN	Continuous	21	560
J-Pitt Steel	Johnstown, PA	Continuous	6	77
J&L Structural, Inc.	Aliquippa, PA	Continuous	1	90
Kankakee Steel Div.	Bourbonnais, IL	Continuous	1	100
Kankakee Steel Div.	Seattle, WA	Continuous	1	120
Laclede Steel Co.	Alton, IL	Continuous	4	337
Latrobe Steel Company	Latrobe, PA	Continuous	1	50
LTV Steel	Cleveland, OH	Continuous	3	250
LTV Steel	E.Chicago, IN	Continuous	3	315

Table 2. U.S. Reheat Furnaces - continued

COMPANY	LOCATION	TYPE	NUMBER	CAPACITY, tph
Lukens Steel Co.	Coatesville, PA	Continuous	2	150
McLouth Steel	Trenton, MI	Continuous	1	350
National Forge Co.	Irvine, PA	Continuous	5	5
New Jersey Steel Corp.	Sayreville, NJ	Continuous	1	65
Northwestern Steel & Wire Co.	Sterling, IL	Continuous	4	500
Nucor-Yamato Steel Co.	Blytheville, AR	Continuous	2	385
Oregon Steel Mills	Pueblo, CO	Continuous	9	110
Oregon Steel Mills	Pueblo, CO	Batch	1	7
Pittsburgh Flatroll Co.	Pittsburgh, PA	Continuous	2	Not Available
Republic Steel	South Chicago, IL	Continuous	7	190
Roanoke Electric Steel Corp.	Roanoke, VA	Continuous	1	92
Rouge Steel Co.	Dearborn, MI	Continuous	3	300
Sheffield Steel Corp.	Joliet, IL	Continuous	2	55
Sheffield Steel Corp.	Sand Springs, OK	Continuous	1	80
Structural Metals Inc.	Seguin, TX	Continuous	1	115
Talley Metals Technology	Hartsville, SC	Continuous	1	27
Tamco	Rancho Cucamonga, CA	Continuous	1	100
Timken Steel	Canton, OH	Continuous	16	80
Timken Steel	Canton, OH	Batch	2	4
Tuscaloosa Steel Corp.	Tuscaloosa, AL	Continuous	1	150
U.S. Steel	Fairfield, AL	Continuous	2	550
U.S. Steel	Gary, IN	Continuous	6	450
U.S. Steel	Gary, IN	Batch	6	63
U.S. Steel	Dravosburg, PA	Continuous	5	115
USS-Kobe	Lorain, OH	Continuous	6	67
Weirton Steel Corp.	Weirton, WV	Continuous	2	350
Wheeling-Pittsburgh Steel Corp.	Martins Ferry, WV	Continuous	3	250

Table 3. Reheat Furnace Summary

Furnace Type	Number	Capacity, 10^6 ton/year
Batch	39	1.2
Continuous	180	90.1
Total	219	91.3

The total annual capacity of all reheat furnaces listed is 82.8 million tonnes (91.3 million tons) which corresponds well with the industry production of 86.3 million tonnes (95.1 million tons) [11] at an operating rate of 93 percent of capacity as reported by AISI for 1994 [12].

2.4 Furnace Performance

Based on published information [13-17] and the analysis of actual furnace operating data, typical fuel consumption and NO_x emission levels can be estimated for reheating furnaces.

For cold charging in a batch furnace with recuperator, fuel consumption is about 4.6 to 5.2 GJ/tonne of steel (4.0 to 4.5 MMBtu/ton). For cold charging in a continuous furnace with recuperator, fuel consumption is about 2.1 to 2.7 GJ/tonne (1.8 to 2.3 MMBtu/ton). In both cases, the variation is caused primarily by differences in furnace productivity and in flue gas temperature. Without a recuperator, fuel consumption is about 1.5 GJ/tonne (1.3 MMBtu/ton) higher in a batch furnace and 0.7 GJ/tonne (0.6 MMBtu/ton) higher in a continuous furnace. These values represent an increase of roughly 30 to 40 percent in fuel consumption.

Combining this information with that in Table 3 allows an estimate of the total annual fuel consumption in reheat furnaces, assuming that two-thirds of batch and continuous furnaces have recuperators. Taking average values for fuel consumption for each furnace with recuperators and multiplying by two-thirds of the production capacity for that furnace gives an estimate of the fuel consumed by each type of recuperative furnace. A similar calculation gives the consumption for non-recuperative furnaces. The resulting total of $2.2 \cdot 10^{17}$ J ($2.1 \cdot 10^{14}$ Btu) compares favorably with the previously cited industry statistics.

Although nitrogen oxide emission levels are determined in various ways by different authors, in general NO_x emissions for steel reheat furnaces appear to be in the range of 85 to 130 g NO_2 /GJ (0.2-0.3 lb NO_2 /MMBtu) [16, 17]. Low NO_x burners have been reported with guaranteed emissions of 54 g NO_2 /GJ (0.125 lb NO_2 /MMBtu) under proper operating conditions [14]. A prototype burner using highly preheated air (455°C [850°F]) was tested at 2 GJ/hr (2 MMBtu/hr) in a forging furnace and achieved 20 g NO_2 /GJ (0.05 lb NO_2 per MMBtu) [18].

In a steel reheat practice, several shortcomings of this prototype burner are foreseen. While a larger scale version of this burner suitable for steel reheating is planned, the higher firing rate and lower air preheat temperatures generally available will probably lead to higher NO_x emission rates. In addition, the prototype burner relies on extensive furnace modifications to provide external flue gas recirculation into the burners. In contrast, DOC provides *in-situ* flue gas recirculation without additional equipment. However, DOC does require the installation of standard flow controls and piping for oxygen service.

2.5 Oxy-Fuel Reheating

The substitution of oxy-fuel burners for air-fuel burners has been shown to produce a dramatic drop in the fuel requirements for reheating. This is caused by the reduction in heat losses to the flue gas associated with the reduction or elimination of nitrogen from the process gas stream. Figure 2 shows the flue gas volume and associated fuel requirement to generate 1 MMBtu (1.055 GJ) of available energy within the furnace.

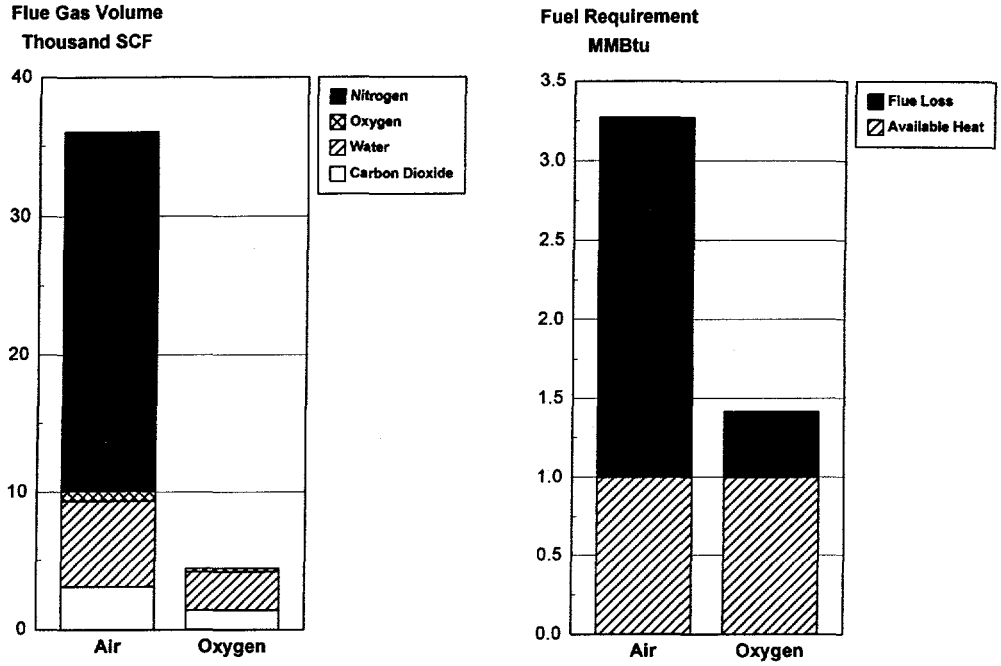

Fig. 2. Flue gas volume and fuel requirement for 1 MMBtu of available heat in the furnace with air and with oxygen.

In batch furnaces, where furnace and flue gas temperatures are essentially the same, the reduction in flue gas volume leads directly to fuel reductions of 45 to 65 percent in commercial reheat furnaces [13]. In continuous furnaces, where the flue gas temperatures are significantly lower than furnace temperatures, the potential improvement is lower. In addition, partial conversion of the furnace to oxy-fuel burners achieves most of the potential fuel savings. These decreasing marginal returns lead to an economic optimum partial conversion of about 70 percent of the furnace firing capacity to oxy-fuel burners. Thus, in practice, fuel reductions in continuous furnaces are typically 30 to 40 percent [13]. Oxygen consumption, expressed as a mass ratio of oxygen to steel, are in the range of 0.15 for batch furnaces and 0.07 for continuous furnaces [13].

Again, this information can be combined with that of Table 3 to estimate the potential fuel savings and potential oxygen volumes required in steel reheating. Taking an average improvement in fuel consumption of 55 percent for batch furnaces and 35 percent for continuous furnaces yields a saving of $7.5 \cdot 10^{16}$ J/year ($7.1 \cdot 10^{13}$ Btu/yr).

Similarly, the oxygen volume required would be $1.0 \cdot 10^{10}$ m^3/yr ($3.6 \cdot 10^{11}$ ft^3). This value is roughly 140 percent of the reported 1994 steel industry consumption of oxygen. Thus, full penetration of the steel reheating market would likely require a doubling of the current oxygen supply to the steel industry. Clearly, the time and capital associated with such an expansion could affect the actual rate of market penetration.

The goal of DOC is to achieve the fuel reduction levels typical of oxy-fuel combustion while generating NO_x emissions of less than 5 g NO_2 /GJ (0.01 lb NO_2 /MMBtu). This would represent an improvement of one order of magnitude over existing low NO_x steel reheating

burners and a factor of at least four improvement over the prototype burner described in section 2.4. It is important that the DOC burner achieve this NO_x goal in furnaces having high nitrogen levels, since, in continuous furnaces, 30 percent of the firing capacity will come from air-fuel burners.

2.6 Economic Analysis

The utility cost for operating an oxy-fuel combustion system, such as a DOC burner, is best analyzed in terms of two parameters, the percent improvement in fuel consumption and the ratio of oxygen cost to fuel cost. The basis for this type of analysis is given below.

The specific utility cost, K_{air}, (dollars/tonne of steel [$/ton]) for an air-fuel system is simply

$$K_{air} = F_{air} C_f \qquad (1)$$

where F_{air} is the fuel consumption (GJ/tonne of steel [MMBtu/ton]), and C_f is the cost of fuel (dollars/GJ [$/Btu]). Similarly, in an oxy-fuel system, the specific utility cost, K_{O2}, is

$$K_{O2} = F_{O2} C_f + O_{O2} C_{O2} \qquad (2)$$

where F_{O2} is the fuel consumption, O_{O2} is the specific oxygen consumption (tonne/tonne [ton/ton]), and C_{O2} is the cost of oxygen (dollars per tonne of oxygen [$/ton]).

To justify oxy-fuel burners on operating economics alone, the ratio K_{O2} / K_{air} must be less than one, so that

$$\frac{F_{O2} C_f + O_{O2} C_{O2}}{F_{air} C_f} < 1 \qquad (3)$$

If P is the improvement in fuel consumption with oxy-fuel burners (expressed as a fraction), then

$$F_{O2} = (1 - P) F_{air} \qquad (4)$$

All the improvement occurs in the furnace zones which are converted to oxy-fuel. If Φ is the fraction of the furnace firing capacity converted to oxy-fuel burners, then within the converted zones

$$F_{O2} = (\Phi - P) F_{air} \qquad (5)$$

For natural gas combustion with 2 percent excess oxygen in the flue, the oxygen requirement is 0.080 tonne/GJ (0.093 ton/MMBtu), therefore

$$O_{O2} = 0.080\,(\text{tonne/GJ})\,(\Phi - P) F_{air} = 0.093\,(\text{ton/MMBtu})\,(\Phi - P) F_{air} \qquad (6)$$

(The corresponding coefficients for the coke oven gas composition given in Table 1 are 0.067 tonne/GJ and 0.078 ton/MMBtu.) If $\Re_c$ is the ratio of oxygen cost to fuel cost, C_{O2} / C_f, then substituting Eqs. 4 and 6 into Eq. 3 and rearranging yields for natural gas

$$\Re_c(NG) < \frac{12.5P}{(\Phi - P)}\left[\frac{\$/\text{tonne}}{\$/\text{GJ}}\right] = \frac{10.7P}{(\Phi - P)}\left[\frac{\$/\text{ton}}{\$/\text{MMBtu}}\right] \quad (7)$$

and for coke oven gas

$$\Re_c(COG) < \frac{15.0P}{(\Phi - P)}\left[\frac{\$/\text{tonne}}{\$/\text{GJ}}\right] = \frac{12.9P}{(\Phi - P)}\left[\frac{\$/\text{ton}}{\$/\text{MMBtu}}\right] \quad (8)$$

Figure 3 shows the critical oxygen cost/fuel cost ratio, $\Re_{c,crit}$, which represents break-even economics, as a function of P for both fuels with $\Phi = 1$ (complete conversion to oxy-fuel).

Also shown in Fig. 3 is the expected range of improvement in fuel rate for batch furnaces. For complete conversion of a batch furnace operating on coke oven gas, the critical ratio varies from 12.3 ($/tonne)/($/GJ) at 45 percent improvement in fuel consumption to 27.9 ($/tonne)/($/GJ) at 65 percent. With an oxygen cost of $33/tonne ($30/ton), oxy-fuel conversion will be economical at a fuel cost of $1.08/GJ ($1.14/MMBtu) for 65 percent improvement and $2.44/GJ ($2.57/MMBtu) for 45 percent improvement.

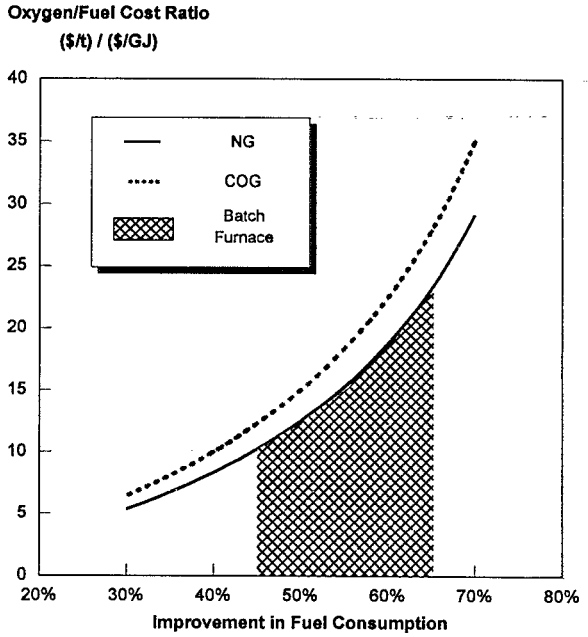

Fig. 3. Oxygen/fuel cost ratio for break-even economics with full conversion to oxy-fuel burners.

As noted in section 2.5, continuous furnaces achieve 30 to 40 percent improvements in fuel consumption at roughly 70 percent conversion. Thus, a continuous furnace operating on natural gas would have a critical ratio between 9.4 and 16.7 ($/tonne)/($/GJ), according to Eq. 7. With the same oxygen cost as before, oxy-fuel conversion will be economical at a fuel cost of $1.98/GJ ($2.09/MMBtu) to $3.51/GJ ($3.70/MMBtu).

In practice, the fuel costs will need to be higher than these critical values to provide payback for the capital (piping and controls) and installation costs associated with oxygen conversion. To provide a two-year payback, for example, a continuous furnace would need a net operating cost improvement on the order of $0.83/tonne ($0.75/ton). This corresponds to an increase in the break-even fuel cost of roughly $0.85/GJ ($0.90/MMBtu). A batch furnace, because of its lower productivity, would need a net operating cost improvement on the order of $3.30/tonne ($3.00/ton), corresponding to a roughly $1.00/MJ ($1.05/MMBtu) higher critical fuel cost.

Thus, at current fuel prices, significant market penetration is expected for batch furnaces, but oxy-fuel conversion of continuous furnaces will be difficult to justify on operating costs alone.

2.7 Emission Requirements

Significant penetration by DOC into continuous furnaces, which represent the bulk of the reheating market, will require other benefits in addition to fuel savings. Reduction of pollutant emissions is a significant potential benefit.

In furnaces using coke oven gas, oxy-fuel burners should lower sulfur emissions in proportion to the reduction in fuel consumption. Since coke oven gas is a by-product, however, this benefits the steelmaker only if there is another process, such as electrical generation, that can use coke oven gas as a fuel. Otherwise, the by-product gas is flared.

Carbon dioxide emissions from reheat furnaces will also be reduced in proportion to fuel consumption for both natural gas and coke oven gas fired furnaces. This gross reduction in CO_2 emissions is cut by about one-half because of the CO_2 released by the generation of electricity consumed at the air separation plant to make oxygen. The net effect, however, is a lowering of CO_2 emissions at roughly half the rate of energy improvement. Efforts to scale CO_2 emissions back to 1990 levels by the year 2000 are currently being debated, and any such limitations could significantly enhance market penetration.

A coarse estimate of the magnitude of these emission reductions can be made by assuming that the industry total fuel consumption for reheating comes half from coke oven gas and half from natural gas. Using the data from Table 1, SO_2 emissions would fall by 400 tonne/yr (450 ton/yr) and CO_2 emissions by 1.6 million tonne/yr (1.8 million ton/yr).

State NO_x emission standards are currently in the range of 0.1-0.2 lb NO_2/MMBtu (43-86 g/GJ) [14]. Meeting the more strict current standards (and any stricter, future standards) requires improvements beyond those of current low NO_x air-fuel burners as described in section 2.4. The goal of the DOC project is to attain NO_x emissions below 5 g/GJ (0.01 lb/MMBtu), well below current and likely future standards. The total amount of NO_x emitted would be reduced further by the improved fuel efficiency of the furnaces. If the current average furnace emits 0.24 lb/MMBtu (100 g/GJ), achieving the DOC goal with the

fuel saving estimated in section 2.5 translates to an annual reduction of 22,000 tonnes (24,000 tons) of NO_x from steel reheating.

Emission Reduction Credits (ERCs) are used to facilitate NO_x reductions in non-attainment areas in California and are under consideration by regulators in other non-attainment areas [19]. The "market value" of these credits ranges from $1.10-$5.50/kg of NO_x reduced ($0.50-$2.50/lb) [19]. Assume a recuperative batch furnace emits 100 g of NO_2/GJ (0.233 lb NO_2 /MMBtu) and consumes 4.9 GJ/tonne of steel (4.25 MMBtu/ton). In a DOC system achieving 5 g of NO_2/GJ (0.012 lb NO_2 /MMBtu) and 2.2 GJ/tonne (1.95 MMBtu/ton) (55 percent improvement in fuel consumption), these credits would have a value of $0.53-2.65/tonne ($0.48-$2.40/ton). If the corresponding numbers for a recuperative continuous furnace are 100 g of NO_2 /GJ (0.233 lb NO_2 /MMBtu) and 2.4 GJ/tonne of steel (2.05 MMBtu/ton) with air and 5 g of NO_2/GJ (0.012 lb NO_2 /MMBtu) and 1.56 GJ/tonne (1.33 MMBtu/ton) (35 percent improvement in fuel consumption), the credits have a value of $0.26-$1.28/tonne ($0.23-$1.15/ton). In both cases, these credits are similar in magnitude to the capital costs discussed in the previous section.

2.8 Increasing Furnace Productivity

There is a continuing drive in the steel industry to increase the productivity of all assets to keep individual mills competitive in the market and to keep steel competitive with alternate materials. Increasing the productivity of reheat furnaces offers savings in capital costs for furnace equipment and lower fuel consumption from reduced furnace heat losses per unit of steel.

The easiest way to increase productivity in a reheat furnace is to raise the furnace temperature. However, in an air-fuel system, this can lead to sharply higher heat losses to the flue gases, resulting in a net increase in fuel consumption per unit of steel. Because flue gas volumes are much lower in an oxy-fuel system, flue gas temperatures and heat losses do not increase as sharply with higher furnace temperatures. This makes it is possible with oxy-fuel to raise productivity and lower specific fuel consumption. Thus, the drive for increased productivity favors conversion to oxy-fuel systems such as DOC.

Another way to increase productivity is hot-charging of the steel. In hot-charging, the steel is transferred quickly from the continuous caster to the reheat furnace to retain as much of the sensible heat from the steelmaking process as possible. Hot-charging requires that the caster and rolling mill be near each other which is not true for most sites. Schedule, inventory, and material handling issues can also limit the amount of hot-charging that can be done [15]. For example, Bethlehem Steel-Burns Harbor, Indiana, hot-charges an average of 20 percent of the slabs to its hot-strip mill at an average temperature of 500°F (260°C) and lowers their fuel rate from 1.83 MMBtu/ton (2.13 GJ/tonne) to 1.73 MMBtu/ton (2.01 GJ/tonne) [15]. In comparison, LTV Steel Cleveland, Ohio, was able to closely couple the caster and hot-strip mill, creating the Direct Hot-Charge Complex. The Complex hot charges 85 percent of the steel from the mill's twin-strand slab caster. LTV charges the slabs at 1575°F (855°C) and uses only 0.9 MMBtu/ton (1.05 GJ/tonne) to heat the steel to rolling temperature [15] and requires only one hour of residence time compared with two hours for cold-charged slabs. To the extent future casters and mills are designed for hot-charging,

reheat fuel consumption will fall, making it more difficult to economically justify oxy-fuel systems like DOC.

2.9 Assessment

Oxy-fuel reheating offers reduced utility (fuel + oxidant) costs for batch reheat furnaces at current fuel prices. Thus, conversion of these furnaces can be justified purely on operating economics. However, oxy-fuel conversion of continuous furnaces results in higher operating costs at current fuel prices. Penetration of this segment, which represents the vast majority of steel production will require additional incentives. Additional benefits of up to $1.50/GJ ($1.50/MMBtu) could be needed to offset the operating cost penalty of oxygen in continuous furnaces at current fuel prices.

Since oxy-fuel heating has been shown to provide significant productivity increases for continuous furnaces, industry needs for higher furnace productivity provide one additional incentive, making oxy-fuel systems such as DOC more favorable. However, hot charging represents an attractive alternative for productivity increases.

Emission Reduction Credits (ERCs) are another potential incentive. The DOC system with NO_x emissions below 5 g/GJ (0.01 lb/MMBtu) would successfully meet the more strict current state standards and likely future standards [20]. Based on the current value of ERCs, this level of NO_x improvement could generate sufficient emission-based benefits to the steelmaker to balance the capital required for piping and controls. Reduced CO_2 and SO_x emissions related to reduced fuel consumption with oxygen could be added incentives.

Even with favorable economics, the actual rate of complete market penetration could be affected by the need for significant expansion in oxygen production capabilities.

Low-NO_x air burners are potential competition for the DOC system. However, current low-NO_x air burners cannot meet the more strict standards, and prototype low-NO_x air burners require costly and complicated installations. DOC should be the preferred NO_x reduction method.

3.0 TECHNICAL SURVEY

The primary goal of the dilute oxygen combustion (DOC) project is to develop an ultra-low NO_x burner system for commercial furnace applications. Part of the research effort involved evaluating some of the fundamental issues associated with diffusion flames in dilute-oxygen, high-temperature environments. In particular, jet mass entrainment rates, flame lift-off heights, and species and velocity distributions were examined in a bench-scale apparatus. The remaining portion of the research effort involved evaluating the pollutant emissions (e.g., NO_x, CO) and the combustion stability associated with the DOC burner under a variety of conditions in a laboratory-scale furnace. Before presenting the measurement results, previous work related to the pertinent aspects of this study is detailed next.

3.1 Mass Entrainment

Entrainment phenomena have been a robust topic of research because of its importance in a variety of arenas, including the design of low-pollutant emission burners for commercial furnace applications. Examples of research include fundamental jet studies [21-24], turbulent flame studies [21, 25-27], pool fires [28-32] and shear layers [33, 34]. In addition, recent turbulent natural gas combustion modeling efforts have employed mass entrainment correlations [35]. Studies directly related to the entrainment work undertaken in this project are reviewed next.

In a classic study, the mass entrainment of both nonreacting and reacting turbulent jets were measured by Ricou and Spalding [21]. The jet under study was enclosed in a cylindrical chamber having an opening to atmosphere large enough for the jet flow to exit the chamber uninhibited. Surrounding gas was fed around the jet through a porous cylindrical ring inside the chamber. The differential pressure across the exit of the chamber was used as an indication of the entrainment capacity of the jet. When the differential pressure across the chamber opening was zero, Ricou and Spalding [21] noted that the supplied surrounding gas flow matched the mass flow that can be entrained by the jet under study.

From their experimental results, Ricou and Spalding [21] developed an expression for the mass entrained by an isothermal gas jet, given by,

$$\frac{m_t}{m_o} = \frac{m_s + m_o}{m_o} = 0.32\frac{x}{d_e} = 0.32\left[\frac{x}{d_o}\right]\sqrt{\frac{\rho_s}{\rho_o}} \qquad (9)$$

where m_t is the total mass flow rate, m_s is the surrounding-gas mass flow rate, m_o is the jet mass flow rate at the injector exit, x is the axial distance from the injector exit, d_e is the equivalent diameter, d_o is the injector diameter, ρ_s is the surrounding-gas density and ρ_o is the jet gas density. Ricou and Spalding [21] also noted that buoyancy-dominated jets have a larger entrainment rate than momentum-dominated jets, and that combustion diminished the entrainment capacity of a jet.

Often times when a jet issues into a surrounding gas of differing density, an equivalent diameter, d_e, is used, and in fact is evident in Eq. 9. The equivalent diameter is calculated from the initial jet momentum with the assumption that the jet density is that of the surrounding gas, and is given by the following relation [36]:

$$d_e = d_o\sqrt{\frac{\rho_o}{\rho_s}} \tag{10}$$

Becker and Yamazaki [25] experimentally investigated the jet spread, entrainment and momentum flux associated with turbulent diffusion flames. The reactants were commercial propane and air, and values of the mean temperature and mean axial velocity within the flame region were obtained by using a thermocouple and a slender pitot tube, respectively. Correlations were developed for a number of quantities, including the mass entrainment ratio, which had a dependency on the Richardson number (buoyancy/input momentum flux). The form of the developed mass entrainment correlation revealed an increase in the mass entrainment capacity of the jet as buoyancy became important. More specifically, the entrainment ratio in a buoyancy-dominated regime increased by a factor of 5.8 over that in a momentum-dominated regime [25]. To a great extent, the mass entrainment correlation in the momentum-dominated regime developed by Becker and Yamazaki [25] agreed with that formulated by Ricou and Spalding [21].

Zhou and Gore [28] studied the flow field associated with a 71 mm toluene pool fire using a laser Doppler velocimeter (LDV). The authors [28] noted that only a small amount of the air being entrained by the pool flame actually crossed the visible flame boundary. The detailed LDV measurements also confirmed instances of radial outflow from the flame as well as negative axial flow (towards the pool of toluene). The work brings to focus the potential importance of transient phenomena with regards to understanding entrainment behavior.

Dahm [26] developed a methodology to calculate a diameter, d^+, which addresses the heat release effects associated with turbulent diffusion flames, and can subsequently be used in existing isothermal jet scaling correlations. This scaling diameter is given by,

$$d^+ = \sqrt{\frac{\rho_o}{\rho_{s,eff}}}\, d_o \tag{11}$$

where $\rho_{s,eff}$ is the effective surrounding-gas density. When confronted with turbulent diffusion flame scaling issues, d^+ would be employed instead of the equivalent diameter, d_e.

Correct assessment of the effective surrounding-gas density involves calculating an effective surrounding gas temperature, $T_{s,eff}$. The effective surrounding-gas temperature is ascertained based on the combustion characteristics of the fuel and oxidant as well as the initial fuel and oxidant temperatures, as shown in Fig. 4.

For standard gaseous fuels and oxidants, the flame temperature is bilinear when plotted as a function of the specific heat-weighted fuel mixture fraction (mole basis), with η specifically given by,

$$\eta_i = \frac{X_i C_{p_i}}{\Sigma X_j C_{p_j}} \tag{12}$$

where X_i is a mole fraction and C_p is the constant pressure specific heat. The specific heat should be evaluated at the local temperature of the stoichiometric products and fuel. As a simplifying procedure, for several fuel and oxidant systems such as H_2/O_2 and CH_4/O_2, η can

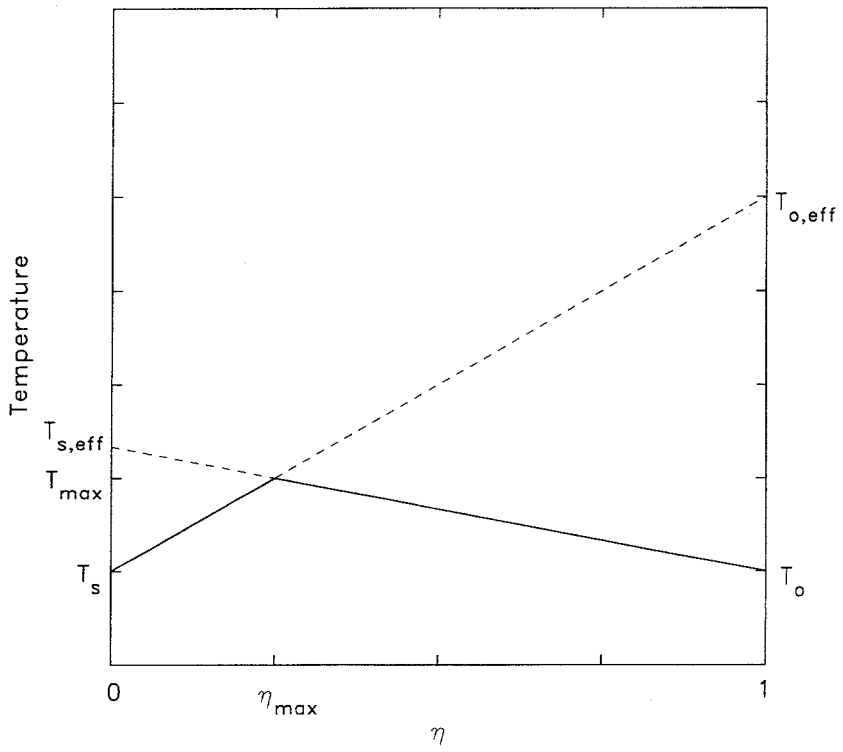

Fig. 4. Schematic diagram of flame temperature plotted as a function of the specific heat-weighted fuel mixture fraction (mole basis), η. $T_{s,eff}$ is determined from such a plot.

be calculated based solely on the fuel mixture fraction (mole basis). Note that the bilinear nature of the temperature distribution breaks down if dissociation becomes important. Of course, dissociation is encountered for fuels and oxidants having a high adiabatic flame temperature. Consequently, under these conditions, some care must be exercised in determining an appropriate effective temperature, $T_{s,eff}$.

The effective surrounding gas temperature is extrapolated from the bilinear graph of temperature versus fuel mixture fraction (see Fig. 4), as follows;

$$T_{s,eff} = T_o + \frac{T_{\max} - T_o}{1 - \eta_{\max}} \tag{13}$$

The effective surrounding gas temperature is subsequently used to calculate $\rho_{s,eff}$, which in turn can be used to calculate d^+ using Eq. 11. Incorporation of d^+ instead of d_e in the various nonreacting turbulent jet correlations allows those correlations to be used for reacting cases. For example, the mass entrainment correlation developed by Ricou and Spalding [21] would become;

$$\frac{m_s + m_o}{m_o} = 0.32\frac{x}{d^+} = 0.32\frac{x}{d_o}\sqrt{\frac{\rho_{s,eff}}{\rho_o}} \tag{14}$$

Similar modifications can be made to isothermal turbulent jet centerline velocity and mixture fraction correlations. Dahm [37] has shown that invoking d^+ scaling leads to successful prediction of centerline velocities and mixture fractions for a variety of diffusion flames.

3.2 Flame Lift-Off Heights

A number of studies treating diffusion flame lift-off heights [38-42] and blowout stability limits [43-47] have been pursued. An excellent review of previous flame lift-off and blowout behavior associated with turbulent diffusion flames along with further detailed analyses is given by Pitts [48].

Flame lift-off heights and flame lengths were measured for a variety of turbulent diffusion flames by Kalghatgi [38]. The fuels studied included hydrogen, propane, methane and ethylene, all of which were combusted in still air. Kalghatgi [38] found that the lift-off height for the turbulent diffusion flames varied linearly with exit velocity, and did not depend on the burner diameter. In addition, an expression was developed in which all of the tested flame lift-off height data collapsed to a single line for all of the different fuels tested, and is given by [38],

$$\left(\frac{hS_L}{\nu_o}\right) = 50\left(\frac{U_o}{S_L}\right)\bar{\rho}^{1.5} \qquad (15)$$

where h is the flame lift-off height from the burner base, S_L is the laminar flame speed, ν_o is the kinematic viscosity of the jet fluid, U_o is the jet velocity at the nozzle exit and $\bar{\rho}$ is the ratio of the density at the nozzle exit, ρ_o, to that of the ambient fluid, ρ_s. The correlation given by Eq. 15 is valid for density ratios, $\bar{\rho}$, between 0.5 and 2. The density ratios associated with the tests performed in this study were typically between 2.7 and 2.9.

Takahashi and Schmoll [39] characterized several flame lifting mechanisms of methane/air diffusion flames by using a three-dimensional laser Doppler velocimeter. Detailed velocity measurements were made in the vicinity of the fuel tube (both thin-walled and thick-walled tubes were considered) to ascertain what role the flow structure in this region plays in flame lifting mechanisms. Dramatic differences in the flame lift-off and blow-out behavior were observed between thin- and thick-wall tubes. The author's [39] flame lift-off observations, the detailed LDV measurements coupled with a detailed literature review were used to establish several flame lift-off criteria.

3.3 Velocity Measurements

The momentum and mass conservation equations coupled with several empirical relations can be used to develop expressions for the axial and radial velocities associated with a turbulent nonreacting jet [49, 50], with these relations being in good agreement with experimental measurements. One such expression describes the centerline velocity decay of such a jet [50];

$$\frac{U_{cl}}{U_o} = \frac{6.575}{\left(\frac{x}{d_o}\right)} \qquad (16)$$

where U_{cl} is the centerline jet velocity.

Due to the continued development of commercially-available laser Doppler velocimeters, two- and three-dimensional velocity measurements in combustion systems have become common. Measurements made using laser Doppler velocimetry (LDV) can be used to unveil important aspects of the flow including the mean velocities, the location and strength of recirculation zones, the magnitude of important turbulence quantities (e.g., turbulent kinetic energy, turbulent shear stress) and corroborating various theoretical and empirical expressions, such as Eq. 16. The ever increasing popularity and usability of LDV systems has spawned a broad range of literature. The fundamental principles of LDV systems has been catalogued by Durrani and Greated [51] and Durst et al. [52], with recent advancements and the general trends associated with the use of modern LDV systems discussed by Chigier [53]. Studies which reveal the velocity field and turbulence properties of both bench-scale [54-56] and pilot-scale [57] flames have been pursued. Two studies which compared the velocity and turbulence fields of nonreacting and reacting turbulent jets are reviewed next. .

An examination of the velocity (mean and turbulent properties), species and temperature fields associated with a reacting and nonreacting turbulent jet was carried out by Takagi et al. [54]. An H_2/N_2 turbulent jet in a co-flowing stream of air was studied under reacting and nonreacting conditions. Takagi et al. [54] observed that the axis flow velocity decay rate was inhibited by the flame, and species measurements revealed that mixing was delayed as well. The flame also was observed to suppress turbulence in the upstream portions of the jet; however, the turbulence increased with axial distance, surpassing the levels observed in the nonreacting jet.

Another detailed comparison of the various mean and turbulence properties of nonreacting and reacting round turbulent jets was completed by Sislian et al. [56]. Velocity, temperature and schilieren measurements were used to evaluate the effect of chemical reactions on the structure of round turbulent jets. Sislian et al. [56] also found that combustion inhibits the axial velocity decay rate. In addition, the turbulent kinetic energy associated with the combusting case was lower than the cold-flow case in the near-field of the jet; however, in the downstream region of the jet, the turbulent kinetic energy in the combusting case was higher than the cold-flow case. Increased viscosity due to the temperature increase as a result of reaction was used to explain the lower turbulence levels in the combusting jet near-field region. However, for the reacting jet, large velocity gradients in the downstream jet region produce turbulence over and above that suppressed by the increased viscosity.

3.4 Pollutant Emissions

The development process of any new industrial burner for commercial furnace applications must address the pollutant emissions of that burner, particularly carbon monoxide (CO) and nitrogen oxides (NO_x), due to stringent guidelines and regulations. These regulations are in place in most industrialized nations to prevent the debilitating effects of these pollutants on the environment and the health of the populace. As a result of the obvious general importance of pollutant emissions, a broad spectrum of literature on the subject exists, all of which will not be reviewed in this document. However, those interested in a broad treatment of the sources and control of NO_x emissions (e.g., NO, NO_2), in addition to its effects on the environment are referred to Refs. 58-60.

A comprehensive description of the chemical routes responsible for NO_x formation in combustion systems is given by Miller and Bowman [61]. NO_x formation in high-temperature

processes involving the combustion of a fuel (containing no nitrogen) is primarily due to the thermal or extended Zeldovich mechanism. It is the oxidation of the nitrogen contained in the oxidant (e.g., air) which contributes to NO_x production. In addition, note that, within the flame zone, O and OH concentrations much larger than equilibrium values (superequilibrium) can significantly increase the NO formation rate [58]. However, in general, by limiting the flame temperature or limiting the time in which the relevant species spend at high temperature, the NO formation rate can be inhibited. With regards to the DOC project, the flame temperatures are minimized by combusting the fuel with a dilute-oxygen oxidant.

Under certain conditions, other mechanisms can significantly alter the NO formation rate. The prompt, or Fenimore, NO mechanism involves reaction between hydrocarbon radicals and molecular nitrogen which eventually leads to NO [62]. The prompt NO mechanism is often significant during fuel-rich combustion conditions. Under fuel-lean conditions, the formation of the intermediate species N_2O, which eventually leads to NO, becomes important when ascertaining the NO formation rate [58].

In addition to the elucidation of the detailed chemical pathways responsible for NO_x formation, a great deal of work identifying the physical mechanisms responsible for NO_x formation has been pursued. For example, Turns et al. [63] have explored the effects of flame radiation, fuel type, and various fluid mechanic properties on the NO_x emissions of turbulent hydrocarbon diffusion flames. The data of Turns et al. [63] are complemented by the study of Driscoll and Dahm [64] who have evaluated the effects of flame strain and superequilibrium oxygen atom concentrations on NO_x formation.

Emissions data are often quantified in a number of ways [65], with NO_x measurements typically expressed as a concentration on a dry basis (e.g., ppm) corrected to a given oxygen level (e.g., 3% O_2 dry basis). In addition, the emission index, EI_i, is often used, and is defined as the ratio of the mass of species i emitted to the mass of fuel burned during the combustion event [65],

$$EI_i \equiv \frac{m_{i,emitted}}{m_{f,burned}} \tag{17}$$

For hydrocarbon fuels, the emission index can be calculated from concentration measurements of the pollutant of interest as well as the species containing carbon atoms (e.g., CO, CO_2) as shown below [65],

$$EI_i = \left(\frac{X_i}{X_{CO} + X_{CO_2}}\right)\left(\frac{aMW_i}{MW_f}\right) \tag{18}$$

where X is the mole fraction of the appropriate species, MW is the molecular weight of the appropriate species, and a is the number of moles of carbon in a mole of fuel, C_aH_b. Either wet or dry concentrations can be employed in Eq. 18 as long as all concentrations remain consistent. The emission index is independent of any dilution of the product stream.

The power emission index, PI_i, relates the mass of pollutant emitted to the amount of fuel energy supplied, as given by Eq. 19 [65],

$$PI_i \equiv \frac{EI_i}{\Delta h_c} \tag{19}$$

where EI_i is the emission index given by Eq. 18 and Δh_c is the fuel heat of combustion. In general, the NO_x emission data taken in this study was represented by the power emission index.

3.5 Combustion Stability

Clearly it is desirable to obtain a combustion event that is stable, and research on the subject is quite broad ranging from furnaces to rocket engines (see Refs. 66-68). Combustion stability phenomena is a complex subject since it involves the synergy between combustion and acoustics. A result of this complexity is the wide-spread use of empirical stability correlations, and of course, the pursuit of extensive hardware stability testing.

The most severe, and potentially catastrophic, stability problems occur when any pressure oscillations resulting from the combustion event couple with the resonant frequencies of the combustion chamber. This resultant coupling can result in amplitude growth of the pressure oscillations which can compromise the structural integrity of the chamber. Even pressure oscillations having smaller amplitudes can degrade the chamber components over time, and may adversely affect system performance. Thus, it is especially important to have a knowledge of the resonant frequencies of the combustion chamber under the appropriate operating conditions. Calculations of these resonant modes can be done, but may be complex depending on the geometry and the combustion environment.

Calculation of the resonant modes of a cylindrical geometry is accomplished through solving the three-dimensional wave equation [69]. The solution of this equation is given by;

$$p = \cos(m\varphi)\cos\left(\frac{\omega_z x}{c}\right) J_m\left(\frac{\omega_r r}{c}\right) e^{-2\pi i f t} \tag{20}$$

where p is the pressure, m in an integer, φ is an angle, ω is the angular frequency, c is the sound speed, J_m is the Bessel function, x is the axial distance, r is the radius, f is the frequency, i is the imaginary number and t is time. After applying the appropriate boundary conditions for a right cylinder, the following characteristic function emerges;

$$f = \left(\frac{c}{2}\right)\sqrt{\left(\frac{n_z}{l}\right)^2 + \left(\frac{\alpha_{mn}}{r}\right)^2} \tag{21}$$

where l is the cylinder length, α_{mn} is the solution of the equation $dJ_m(\pi\alpha)/d\alpha=0$ and $n_z=0, 1, 2 \ldots$ Equation 21 can be used to calculate the standing wave resonant frequencies for a cylindrical geometry as long as the cylinder dimensions and the sound speed of the environment are known.

Resonant modes having specific values of m, n and n_z can be identified as axial, radial, tangential or some combined mode. For example, with $m=n=0$, the resonant or standing wave modes are identified as axial, where the motion is parallel to the axis of the cylinder. Modes in which $n_z=m=0$ are referred to as radial modes where the pressure amplitude maximum values coincide with the chamber axis. Pure tangential modes in which $n=n_z=0$ have the greatest

pressure amplitude along the circumference of the cylinder geometry. Of course, combined modes can occur as well.

4.0 EXPERIMENTAL

The experimental program can be divided into two parts. In the first part, a series of bench-scale experiments were undertaken to enhance the understanding of the mixing and combustion characteristics of gaseous fuels and oxidants under previously unexplored conditions. The second broad set of experiments concentrated on establishing the pollutant emissions of the dilute oxygen combustion (DOC) burner in a laboratory-scale furnace. In addition, the combustion stability aspects of several burner configurations were tested. The experimental intricacies of each part are treated next, as well as elucidation of the diagnostic techniques and instruments used in the experimental project.

4.1 Reactants

Natural gas was used throughout the research project as the fuel, while either air or pure oxygen was used as the oxidant. The natural gas was analyzed using a UTI 100C mass spectrometer. The typical composition of the natural gas along with a number of important mixture properties are given in Table 4.

Table 4. Natural Gas Composition and Properties (typical)

Species	Percent by Volume
CH_4	$9.56 \cdot 10^{1}$
C_2H_4	$3.74 \cdot 10^{-1}$
C_2H_6	$2.81 \cdot 10^{0}$
CO_2	$1.06 \cdot 10^{0}$
N_2	$1.32 \cdot 10^{-1}$
O_2	$1.12 \cdot 10^{-3}$
Ar	$1.67 \cdot 10^{-2}$
Parameter	**Value**
MW, kg/kmol	16.8
C_p, kJ/kg-K	2.18
Δh_c, kJ/kg_f	53627

The house natural gas was nearly pure methane, having similar properties. In general, the natural gas composition and calculated mixture properties were used during data reduction.

4.2 Gas Sampling and Instrumentation

For both the bench-scale apparatus and the laboratory-scale furnace experiments, gas samples were extracted through water-cooled copper or water-cooled stainless steel probes using a vacuum pump-based gas sampling system. The water cooling of a particular probe enhanced its survivability in the combusting environment, and quenched any possible reactions in the extracted gas sample. In general, prior to sending the gas sample to a bank of gas analysis instruments, the water was removed from the sample. The only exception was the use

of a Hague oxygen analyzer situated in the furnace flue port. The Hague oxygen analyzer yielded the oxygen concentration of a sample on a wet basis. A list of the of the employed gas analysis instruments is given in Table 5. Prior to each testing session, all of the instruments were appropriately calibrated. Duplicate measurements of some species, such as CO_2 for example, were made to help address measurement bias.

Table 5. Gas Analysis Instruments

Description	Make and Model
O_2 Analyzers	Servomex 570A Hague OxSen 200D608
CO_2 Analyzers	Horiba VIA-510 Horiba PIR-2000
CO Analyzers	Lira MSA Horiba VIA-500
NO Analyzer	Horiba CLA-510S
Mass Spectrometer	UTI 100C

Inaccurate NO_x values can be obtained using a chemiluminescent-based analyzer due to the quenching effects of other species, such as CO_2 [70, 71]. The measurement susceptibility of the Horiba CLA-510S NO analyzer to CO_2 quenching effects was evaluated and found to be negligible for CO_2 volume fractions between 0 and 95%. It also should be noted that a NO_2 to NO converter was not used for any of the tests, hence only NO was measured. However, the density of NO_2 was used for the calculation of all of the appropriate emission indices.

4.3 Bench-Scale Apparatus

The bench-scale combustion apparatus allowed for the entrainment and combustion stability characteristics of gas jets to be studied in a variety of surrounding gas environments. Typically, the combustion traits of a natural gas jet were investigated in a high-temperature ($T \sim 1360$ K), dilute/enriched-oxygen (6-27% O_2) environment.

4.3.1 Bench-Scale Equipment

The bench-scale apparatus consisted of a coaxial-tube burner, a gas mixing chamber equipped with ten water-cooled heat sinks, an entrainment chamber and a water-cooled injector element. A schematic diagram of the bench-scale apparatus is shown in Fig. 5. A coaxial-tube burner was used to generate a high-temperature gas mixture in the mixing chamber by burning natural gas and oxygen at a given equivalence ratio. Hence, the major species in the mixing chamber were typically CO_2, H_2O and O_2. Retractable water-cooled heat sinks were used to tailor the gas temperature. The hot gas traveled to the cylindrical-shaped entrainment chamber via two pipes. Two entrainment chambers were used, one with and the other without windows (see Fig. 5). The gas subsequently passed through a porous cylinder (or a porous disk depending on which entrainment chamber was being used) and interacted with the natural gas emanating from the water-cooled injector. All of the gases subsequently exited the entrainment chamber through an Inconel insert. A fume hood withdrew the combustion gases from the laboratory.

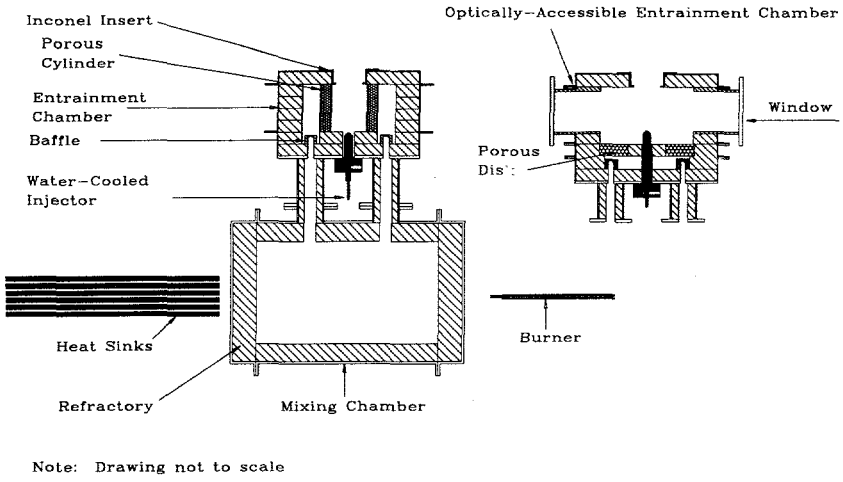

Fig. 5. Schematic diagram of the bench-scale apparatus.

Again, a coaxial-tube burner was used to generate the desired high-temperature surrounding-gas flow, and was inserted into the mixing chamber through a port in one of the endcaps. The burner consisted of two concentric stainless steel tubes, with fuel (natural gas) being supplied through the central tube, and oxidant (oxygen) flowing through the annulus. The burner was cooled by the passing fuel and oxidant gases. The inner diameter of the fuel tube was 6.35 mm, while the outer diameter was 9.53 mm. The inner diameter of the outer tube was 12.7 mm and the outer tube was recessed 44 mm from the tip of the fuel tube.

The refractory-lined mixing chamber allowed the combustion products from the coaxial-tube burner (e.g., CO_2, H_2O and O_2), as well as other input gases (e.g., N_2) to mix and acquire a target temperature prior to entering the entrainment chamber. The steel, cylindrical-shaped mixing chamber consisted of two endcaps and a midsection piece. The interior of the steel mixing chamber was lined with castable refractory ($T_{max} \sim 1800$ K), resulting in an inner diameter of 305 mm and an inner length of 775 mm. Through each endcap, up to ten 19 mm-diameter, 910 mm-long, water-cooled heat sinks could be inserted into the mixing chamber to achieve a desired gas temperature. In addition, the mixing chamber contained several ports which allowed for the entry of other gases (e.g., N_2), and the placement of thermocouples, pressure probes and sight glasses. The gases depart from the mixing chamber and feed the entrainment chamber via two 100 mm (4.0 in) diameter steel pipes. These pipes were lined with castable refractory resulting in an inner diameter of 51 mm.

The entrainment chamber consisted of a top and bottom steel endcap and a (or several) steel midsection(s). Different midsections were used to vary the chamber height. In addition, a midsection piece having three large windows (see Fig. 5) was available for visualizing the flame process under study. The entrainment chamber mimics, to a large extent, the experimental apparatus of Ricou and Spalding [21]. The entrainment chamber was lined with fiber block refractory having a maximum temperature rating of 1700 K (2600°F). Gas from the mixing chamber entered the entrainment chamber via the two pipes and impinged upon a

refractory baffle which forced the high-temperature surrounding gas to travel tangentially around the circumference of the entrainment chamber. Subsequently, the gas passed through a cylindrical-shaped, 38 mm-thick Zirconia porous ring. The high-temperature gas passing through the porous ring interacted with the jet under study and exited the top of the entrainment chamber through an Inconel insert having a circular opening. A schematic diagram portraying the jet entrainment region associated with the entrainment chamber is shown in Fig. 6.

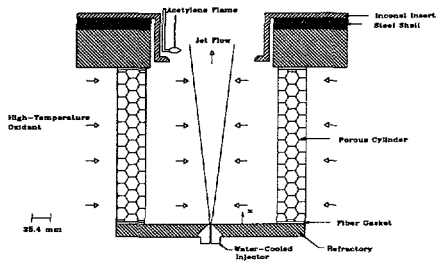

Fig. 6. Schematic diagram of the jet entrainment region.

The height of the entrainment chamber, defined as the distance between the injector exit plane and the bottom of the Inconel insert, could be varied from 51 to 220 mm since a number of porous rings, chamber midsections and Inconel inserts were available. The diameter of the Inconel insert was chosen based on the findings of Ricou and Spalding [21], who determined that the chamber exit diameter should subtend an angle of 30° to the base of the entrainment chamber to minimize any interference between the free turbulent jet and the exit orifice. In addition, this exit diameter criterion yielded good sensitivity for their mass entrainment measurement technique.

As mentioned previously, an entrainment chamber midsection piece having three large windows was available. For this piece, the gas passed through a 50.8 mm thick, 406 mm outer diameter, 102 mm inner diameter Zirconia porous disk. Note that this Zirconia porous disk replaced the Zirconia cylinders previously described. The gas interacted with the jet under study and exited the entrainment chamber through the Inconel insert. The midsection piece had three large openings, 150 mm in width and 190 mm in length, arrayed about the midsection circumference at 90° intervals. For visual access into the chamber, 6.35 mm-thick quartz windows were carefully bolted in place over the midsection openings. The viewing area of each window was often restricted by placing fiber block refractory in the chamber interior to curtail chamber heat loss. Each window could be purged with nitrogen on its inner surface to prevent condensation.

A water-cooled injector was placed in the bottom endcap of the entrainment chamber. Typically, natural gas was fed through this injector into the entrainment chamber. The water-cooled injector ensured that the injected gas temperature was constant at about 289 K (60°F). The design allowed for modification of the injector inner diameter and the capability of surrounding the primary gas flow with an annular gas flow (e.g., O_2 or H_2). The injector diameters available were 0.7938, 1.59, 3.18 and 4.72 mm (0.03125, 0.0625, 0.125, 0.186 in).

Thermocouples in the both the mixing chamber and the entrainment chamber were used to monitor the temperatures in the apparatus. The thermocouple in the entrainment chamber was embedded in the porous material in order to acquire a close approximation to the gas temperature. The temperature acquired from this thermocouple was taken as the gas temperature with no corrections performed.

4.3.2 Bench-Scale Measurement Program

The research project called for several fundamental gas jet studies which will enable optimum design and operation of future pilot- and commercial-scale DOC burners. Measurements of the jet mass entrainment rates, flame lift-off heights, gas velocities and species concentrations were made using the bench-scale apparatus (see Fig. 5) as a function of the surrounding-gas composition, the surrounding-gas temperature, and several gas jet geometric and flow parameters.

In general, mass entrainment measurements were made for nonreacting and reacting flow cases, and the Zirconia porous cylinders (instead of the porous disk) were used in the entrainment chamber. The principle behind the jet entrainment measurements was taken after the work of Ricou and Spalding [21]. As a gas jet develops, it will entrain the surrounding fluid. With respect to the bench-scale apparatus, the fluid in which the jet entrains can either come from the supplied surrounding gas emanating from the porous section or from outside the chamber through the Inconel insert. If fluid is being drawn through the chamber exit to satisfy the jet entrainment appetite, then axial pressure gradients along the jet axis would be present. However, these pressure gradients vanish as flow is fed through the porous cylinders and is entrained by the jet. For a certain surrounding-gas mass flow rate, the jet no longer draws fluid from outside the chamber, and, hence, the mass entrained by the jet is know since all flows are metered. The mass entrainment rate of turbulent gas jets was measured using several techniques, including differential pressure measurements across the exit of the entrainment chamber, helium doping of the ambient atmosphere, and observation of a small flame across the exit of the entrainment chamber.

As mentioned previously, the design of the entrainment chamber is similar to that of Ricou and Spalding [21]. In their study, the pressure across the exit of the entrainment chamber was measured using a micromanometer. When the pressure difference across the exit was zero, they [21] concluded that the jet entrained all of the supplied surrounding-gas flow. The same approach was taken in this study; however, instead of using a micromanometer, a Setra digital pressure transducer, model C264, was used, having a measurement range of +/- 0.1 in. water column with an accuracy of 0.25% of full scale. Note that very small differential pressures are being measured.

Despite the considerable effort put forth to use this entrainment measurement technique, limited benefits were achieved. The two factors which biased the differential pressure measurements were the placement of the high and low pressure pickup points of the transducer and the related heating of the gas in the pickup probes during the combusting-flow tests. Different spatial locations (in the vicinity of the entrainment chamber exit) of the high and low pressure pickup points yielded different differential pressure measurement readings. During the combusting-flow tests, the probe position issue was apparently hampered by the fact that radiative heat transfer to the pressure pickup probes caused the gas to heat and subsequently bias the measurement. The elimination of these biasing effects using the current chamber configuration proved difficult, hence this measurement scheme was not pursued.

A second mass entrainment measurement technique was attempted; helium was allowed to bleed out of a sintered stainless steel rod (12.7 mm diameter, 50.8 mm long) above the exit of the entrainment chamber (at the Inconel insert). Helium was not present in the gas emanating from the mixing chamber or the water-cooled injector. A water-cooled sample probe connected to a mass spectrometer was placed inside the entrainment chamber, just below

the lip of the Inconel insert opening. When the jet flow began to entrain more gas than supplied from the mixing chamber, outside air would be drawn into the entrainment chamber along with the helium. Once a "small" helium concentration was registered by the mass spectrometer, the jet was entraining all of the supplied surrounding gas flow.

For this technique to be successful, an arbitrary helium concentration had to be selected for a given helium doping element/sample probe geometry to represent the case of the jet entraining all of the supplied surrounding gas from the mixing chamber. After a limited amount of testing, a high confidence in the measurements was not achieved. The technique attractiveness was degraded further due to the long times necessary to obtain a measurement. Typically, a five minute waiting period was needed to purge the sampling system/mass spectrometer to yield a stable concentration reading. Hence, this mass entrainment technique was not vigorously pursued.

The final and most successful technique utilized was an acetylene torch method. A 3.18 mm (0.125 in) outer-diameter stainless steel tube distributed a low flow rate of acetylene at the exit of the entrainment chamber (see Fig. 6). The acetylene-based flame would either be pushed away from the exit or drawn into the entrainment chamber depending on the jet and surrounding-gas mass flow rates supplied. When the flame appeared balanced between the interior and exterior of the entrainment chamber, the mass flow rates of the jet and surrounding gas were measured and used to calculate the mass entrainment ratio. This technique, albeit simple, seemed to best indicate the jet entrainment rate compared to the other two tested methods, and yielded results in a timely manner. A disadvantage of the method, however, was that it required an interpretation of the status of the acetylene flame.

The acetylene flame method was subsequently used to measure the mass entrainment rate of an air jet in an air atmosphere as a function of jet Reynolds number ($1.2 \cdot 10^4$ to $5.2 \cdot 10^4$) and nondimensional (density corrected) height of the entrainment chamber (x/d_e=35 to 210). For the combusting-flow tests, the same method was used to measure the mass entrainment rate of a natural gas jet as a function of nondimensional (density corrected) chamber height (x/d_e=20 to 80) and surrounding-gas oxygen concentration (6 to 27% vol. wet). In addition, the effect of either an annular flow of hydrogen (m_{ann}/m_o=0 to 0.15) or oxygen (m_{ann}/m_o=0 to 0.15) on the mass entrainment characteristics of the natural gas jet was evaluated.

An attempt was made to evaluate the flame lift-off and blowout characteristics of a fuel jet in a high-temperature, dilute/enriched-oxygen environment. The measurements were made using the bench-scale apparatus equipped with the windowed entrainment chamber. Recall that for the windowed entrainment chamber, the high-temperature surrounding gas was delivered to the entrainment chamber through a 50.8 mm-thick porous Zirconia disk. Hence, the surrounding gas flowed coaxial with the jet flow. The supplied surrounding-gas flow to the entrainment chamber was kept constant, and the gas supplied was large enough to satisfy the entrainment appetite of the jet under study.

Difficulties arose in evaluating the blowout stability limits for a number of reasons. For surrounding-gas flows having a low oxygen content, the flame luminosity was extremely faint and contrast between this flame luminosity and the hot refractory walls was poor hampering both flame blowout as well as flame lift-off measurements. This problem was alleviated to some extent by observing the flame against a low-temperature background (e.g., observing the flame through a window). Second, the exit of the entrainment chamber acted as

a flame holder. Rarely did a flame blow out of the entrainment chamber, but instead attached to the Inconel insert opening. Visual access to the entrainment chamber exit region was limited, and made determination of when the flame transitioned from the chamber interior to becoming attached to the exit difficult.

The flame lift-off tests were more successful. Specifically, flame lift-off measurements for a natural gas jet were taken as a function of the natural gas jet velocity (M_o=0.2 to 0.9), surrounding-gas temperature (T_s=1277 and 1366 K) and surrounding-gas oxygen concentration (7 to 22% vol. wet). The lift-off distance, h, was defined as the distance from the injector exit to the luminous base of the flame. The measurements were made using a pointer inside the entrainment chamber. The pointer was attached to a translation stage, and the pointer did not noticeably affect the flame behavior.

The velocity field associated with a turbulent natural gas jet issuing into a dilute-oxygen, high-temperature environment was investigated in the bench-scale apparatus. The velocity measurements were made using laser Doppler velocimetry (LDV). This laser-based diagnostic technique is used to measure the velocity of particles at a point in space. The two-dimensional (2-D) LDV system employed in this study primarily consisted of a Coherent 5 W argon-ion laser (Innova I-70-5), an Aerometrics fiber optic transceiver, an Aerometrics frequency-domain signal processor (RSA-2000) and an IBM-compatible personal computer (486-33MHz). Note that the LDV system was used in a backscatter mode. The transceiver was mounted to a precision three-dimensional translation stage system for accurate placement of the measurement volume to the point of interest. Due to the heat produced by the flame, it was necessary to cool the exterior of the transceiver with air, and a hot mirror was placed in front of the transceiver to reflect infrared radiation. The diameter and length of the probe volume were 234 μm and 5.83 mm, respectively.

The natural gas flow was seeded with silicon carbide (SiC) particles using a fluidized bed seeder. Two different size seed particles were used, 1 μm and 21 μm diameter. Upon making various velocity measurements under cold-flow conditions and at appropriate injection velocities, similar velocity magnitudes (50-100 m/s) were acquired. It was expected that the 1 μm diameter particles would follow the flow more accurately. This observation seems to indicate that seed agglomeration within the fluidized bed and associated piping is a problem. Baking the seed in an oven for several days (300°F) to remove any moisture did not seem to alleviate any of the agglomeration problems. Future velocity measurements will require an enhanced seeder.

Velocity measurements were made as a function of surrounding-gas temperature (1255-1411 K), surrounding-gas oxygen concentration (14-23% vol. wet) and spatial position ($0<x/d<31$; $0<z/d<3$) within the natural gas jet having a Reynolds number of 19500 (U_o=82 m/s).

In order to ascertain the progress of the combustion of a fuel jet in a high-temperature, dilute/enriched-oxygen environment, detailed species measurements were undertaken using the bench-scale apparatus. Species concentration measurements were made along the flame axis (x/d_o=20 to 120) of a natural gas jet as a function of surrounding-gas oxygen concentration (12 to 23% vol. wet) and the surrounding-gas temperature (1268 and 1374 K). A water-cooled copper probe wrapped in insulating tape extracted the gas sample from the flame region via a vacuum pump-based sampling system which fed the gas sample to a bank of gas

analysis instruments previously described (see Table 5). The slender-nose sample probe orifice diameter was 1.59 mm in diameter, while the probe body diameter was 19.1 mm. The typical species measured included CO_2, CO, CH_4, O_2, N_2 and H_2. The water was extracted from the sample prior to being sent to the gas analysis instrumentation. The water-cooled probe was attached to a three-dimensional translation stage system and entered the entrainment chamber through the top (i.e., the opening of the Inconel insert).

4.4 Laboratory-Scale Furnace

Due to the novel approach of the DOC burner, a series of laboratory-scale experiments were undertaken to fully assess the characteristics of the burner prior to developing a pilot- or commercial-scale burner.

4.4.1 Laboratory-Scale Furnace Equipment

The performance of the DOC burner was examined in the laboratory-scale furnace shown in Fig. 7. The furnace consisted of nine steel sections, a 254 mm (10 in)-long front endcap, seven 457 mm (18 in)-long midsection pieces and a 229 mm (9 in)-long rear endcap. The cylindrical-shaped, castable refractory-lined furnace had an inner diameter of 914 mm (36 in) and an inner length of 3.20 m (126 in). The furnace was designed to handle firing rates up to 293 kW (1.0 MMBtu/h) and wall temperatures up to 1922 K (3000°F).

Both the furnace endcaps and the midsection pieces had a number of port openings giving access to the furnace interior to allow for variation in burner positioning, extraction of gas samples via water-cooled probes, insertion of water-cooled heat sinks, placement of suction pyrometers and, in general, the insertion of any burner device or diagnostic instrument. Each furnace port was assigned a label to facilitate their identification. The labeling regimen is given in Fig. 8.

In order to facilitate the description of the tests performed, a naming convention was devised to detail where on the furnace the fuel and oxidant lances were placed. The naming scheme is best illustrated by a few examples. If the fuel lance was placed in port 8F and the oxidant lance in port 3F, then the burner arrangement would be designated F8F-O3F. The first letter, F, means fuel, while the next two characters, 8F, designate from which port the fuel entered the furnace from. In this case, port 8F is a port on the front face of the furnace (see Fig. 8). In a like manner, the second part of the burner designation continues; O stands for oxidant, while 3F denotes which port on the furnace the oxidant emerged from. Hence, for the previous case, the fuel emanates from port 8F on the furnace front face, while the oxidant emerges from port 3F on the front furnace face. If two oxidant lances were used, one in port 3F, the other in port 1F, then the burner designation would be F8F-O1F-O3F.

The 203 mm (8 in)-diameter flue port was located in the center of the rear endcap (port 4R). There was a sample port and a Hague oxygen analyzer sensor at the flue exit (not shown in Fig. 7). A series of downstream flue vents were used to set the furnace pressure.

Water-cooled heat sinks having a diameter of 48.3 mm and a length of 1.52 m were often used to tailor the furnace wall temperature to the desired level. These heat sinks could be inserted through most of the ports in the furnace.

Each of the seven furnace midsection pieces was equipped with a thermocouple, the position of each being shown in Fig. 8. The wall temperature, T_w, of the laboratory-scale

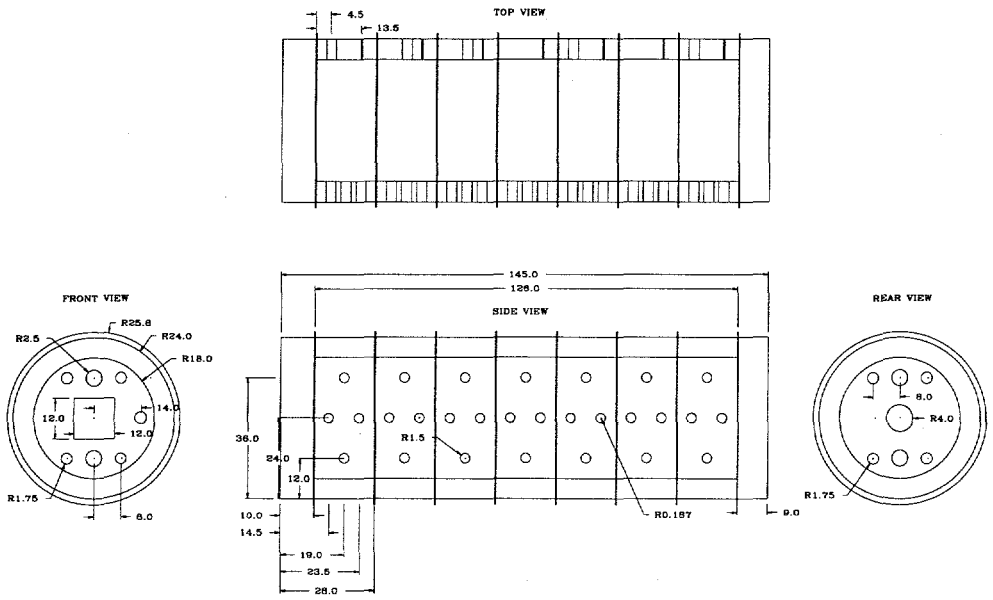

Fig. 7. Diagram of the laboratory-scale furnace. All dimensions shown are in inches, and radial measurements are preceded by a *R*.

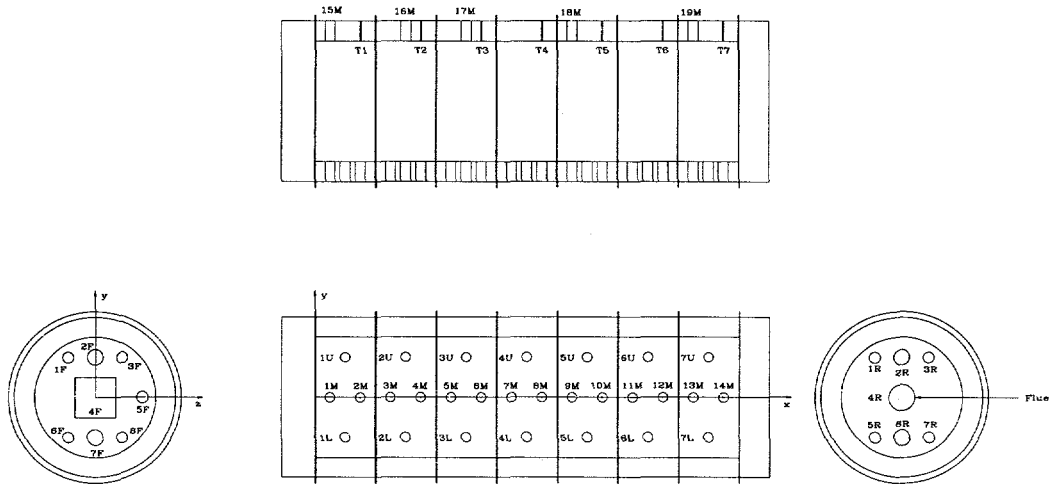

Fig. 8. Schematic diagram of the laboratory-scale furnace identifying the various port and thermocouple labels. A coordinate system is also shown.

furnace was typically ascertained by averaging five thermocouple readings (*T*1 to *T*5 - see Fig. 8) along the length of the furnace.

Several burners/lances were used to deliver the appropriate gases to the furnace. Water-cooling of the lances was employed to allow for quick operational changes and to ensure that the gas temperature of each reactant was known. Each lance consisted of a water-cooled pipe with a removable nozzle with diameters ranging from 4.0 to 17 mm. Again, only one reactant was supplied through each lance.

At times, a coaxial-tube burner was used in the testing project, either as a test burner or to heat the furnace. The coaxial-tube burner consisted of a central tube in which fuel typically flowed. The nozzle could readily be changed, if necessary, and the nozzle diameters ranged between 4.78 to 8.74 mm in this study. The central fuel tube was surrounded by another tube, with oxidant flowing between the two pipes. The flow area of the annulus was bounded by the outer diameter of the fuel tube (33.4 mm diameter) and the inner diameter of the outer pipe (66.9 mm). The coaxial-tube burner was not water-cooled, but was recessed approximately 73 mm from the furnace wall.

The last burner combination employed was the staged coaxial-tube burner which is a combination of the two aforementioned burners. Essentially, fuel was injected through the central tube of the coaxial-tube burner, and a portion of the required oxidant flow was fed through the annulus. The remaining portion of the oxidant flow (typ. 70% vol.) was delivered to the furnace through a lance.

A limited series of tests were undertaken with the DOC burner in which oxygen was preheated using a recuperative heat exchanger manufactured by Thermal Transfer Corporation. Oxygen (or air) can be preheated using the heat of the flue gases, and the heat exchanger is designed to preheat oxygen to 922 K (1200°F) for an oxygen flow rate of 0.0197 m^3/s (2500 scfh). For these tests, a refractory nozzle was employed for the preheated oxygen in place of the water-cooled pipe.

To date, an oxidant preheat temperature of 661 K (730°F) has been achieved at a firing rate of 293 kW (1.0 MMBtu/h), which is lower than the expected design temperature of 922 K. Further improvements in the operation of the recuperative heat exchanger would result in achieving the design preheat temperature. However, higher oxidant preheat temperatures (1366 K) are possible with a regenerative heat exchanger, making better use of the flue gas energy. Thus, future heat recovery work as related to the DOC burner will be concentrated on developing a regenerative system.

4.4.2 Laboratory-Scale Furnace Measurement Program

Several general statements regarding data acquisition and procedures can be made. Typically, the furnace was heated to 1144 K (1600°F), which is above the auto-ignition temperature of natural gas-oxygen, using a low-NO_x burner. During the furnace heat-up period, the furnace pressure was kept slightly positive to purge the furnace of nitrogen and to keep the NO_x formation to a minimum. Once the furnace temperature was over the auto-ignition temperature of the natural gas-oxygen, or at the target temperature for data acquisition, the furnace was briefly shut-down, and the DOC burner was installed. Once the proper firing rate, excess oxygen level, furnace wall temperature and furnace nitrogen content were achieved, data acquisition began.

A major task associated with the experimental project was to determine the burner arrangement which minimized pollutant emissions (e.g., NO_x, CO), yet produced stable combustion. The arrangements studied were representative of what may be needed in a commercial installation and covered situations which may shed light on the physics of achieving very low NO_x. Over fifteen burner arrangements were evaluated with natural gas as the fuel and either pure oxygen or air as the oxidant. For test cases involving natural gas and pure oxygen, nitrogen was injected separately into the furnace to simulate furnace leakage or a partial oxy-fuel conversion.

The effects of furnace temperature (T_w=1175 to 1550 K), furnace nitrogen content (0 to 77% vol. wet), fuel injection velocity (M_f=0.31 to 0.67), firing rate (184 and 286 kW) and oxidant composition (pure oxygen or air) on pollutant emissions were evaluated. A comparison between the DOC burner and more traditional burner designs was pursued to a limited degree.

It is important to point out that as nitrogen was introduced separately into the furnace, the oxidant flow was subsequently modified to maintain an oxygen concentration between 2 - 3% (vol. wet) at the flue. This oxygen content is typical of commercial furnaces. The increase in oxygen mass flow rate resulted in an increase in oxygen velocity through the specific lance nozzle since the nozzle diameter remained constant throughout the test run. For the conditions of this study, the increase in oxygen flow velocity was typically no more than 15% when the furnace nitrogen concentration was increased from 0 to 77%.

The nominal firing rate for most tests was 190 kW (0.650 MMBtu/h) and the nominal furnace wall temperature was held constant at 1366 K (2000°F) using water-cooled heat sinks. Note, when natural gas and oxygen were employed, nitrogen was injected from several different ports to evaluate how the nitrogen injection scheme affected NO_x formation. With reference to Fig. 8, nitrogen was either simultaneously injected through ports 1M, 3M, 5M, 7M, 9M and 11M, or port 2F, or simultaneously through ports 6M, 8M and 10M. For the cases studied, the nitrogen injection scheme did not alter the measured NO_x emissions, and nitrogen was subsequently fed through ports 6M, 8M and 10M. For this injection scheme, the nitrogen injection velocity was no greater than 4 m/s.

For several of the more interesting burner arrangement cases, gas samples were extracted from the furnace interior and analyzed. Detailed furnace probing was done for four specific burner arrangements. The selected burner arrangements represent possible commercial configurations. For each case, at least 20 gas samples were extracted, evenly distributed throughout the interior furnace volume. The gas samples were extracted using either one of two types of probes, and the probing was always done from the side of the furnace (i.e., L, M or U ports - see Fig. 8). A water-cooled, right-angle probe was typically used to extract gas samples from regions within the fuel or oxidant jet boundaries. The sampling orifice diameter for this probe was 1.59 mm and the probe was sufficiently long (0.914 m) to probe across the furnace diameter. A number of water-cooled, straight sampling probes were used to extract gas samples outside of the fuel and oxidant jet boundaries. These probes had a sampling orifice diameter of 4.57 mm, and had sufficient length (0.914 m) to probe the furnace diameter.

5.0 RESULTS AND DISCUSSION

The results of both the bench-scale apparatus and laboratory-scale furnace experiments are delineated next.

5.1 Bench-Scale Apparatus

Several fundamental issues surrounding the DOC burner were explored. These issues included evaluating the mass entrainment, flame lift-off, velocity fields and species distributions of a fuel jet in a high-temperature, dilute/enriched-oxygen environment. All of the experiments were performed in the bench-scale apparatus described in the experimental section, and shown in Fig. 5. To the authors' knowledge, these parameters have not previously been disclosed in the literature for the conditions studied here.

5.1.1 Mass Entrainment

The mass entrainment ratio of both a nonreacting and reacting jet were measured for a number of cases using the bench-scale apparatus shown in Fig. 5. Recall that the mass entrainment was measured by observing the behavior of a small acetylene flame positioned at the chamber exit. When the flame appeared balanced between the interior and exterior of the entrainment chamber, the mass flow rates of the surrounding gas and the jet were recorded. The nonreacting (isothermal) case consisted of an air jet surrounded by an air environment, while for the combusting case, a natural gas jet was surrounded by a dilute/enriched oxygen (6-26% O_2 vol. wet) gas at a temperature of 1366 K (2000°F).

The mass entrainment of a nonreacting jet was given by Eq. 9, developed by Ricou and Spalding [21]. Evaluation of this relation reveals that as x approaches zero, the total mass flow rate, m_t, approaches zero. In fact, m_t should equal the jet mass flow rate, m_o, at $x=0$. Thus, the mass entrainment relation given by Ricou and Spalding [21] was modified to take the aforementioned observation into account, and is given by,

$$\frac{m_t}{m_o} = 0.32\left(\frac{x}{d_o}\right)\sqrt{\frac{\rho_s}{\rho_o}} + 1 \qquad (22)$$

Note that the mass entrainment ratio, as given by Eqs. 9 and 22, approach similar values as x/d_o becomes large. The predictions from this relation were compared to the entrainment ratio measurements made for the air jet/air surrounding-gas case, as shown in Fig. 9. In Fig. 9, the mass entrainment ratio, $(m_s+m_o)/m_o$, is plotted as function of the nondimensional distance, x/d_e $(=(x/d_o)(\rho_s/\rho_o)^{0.5})$, where d_e is the equivalent diameter, defined by Eq. 10. The quantity m_s is the mass flow rate of the surrounding gas and m_o is the mass flow rate of the jet at the injector exit. The distance from the injector exit to a given height along the jet axis is represented by x. In terms of the bench-scale apparatus, x represents the distance from the injector exit to the entrainment chamber exit (at Inconel insert). The entrainment measurements agree well with the predictions obtained from Eq. 22, thus giving confidence in the acetylene torch measurement technique.

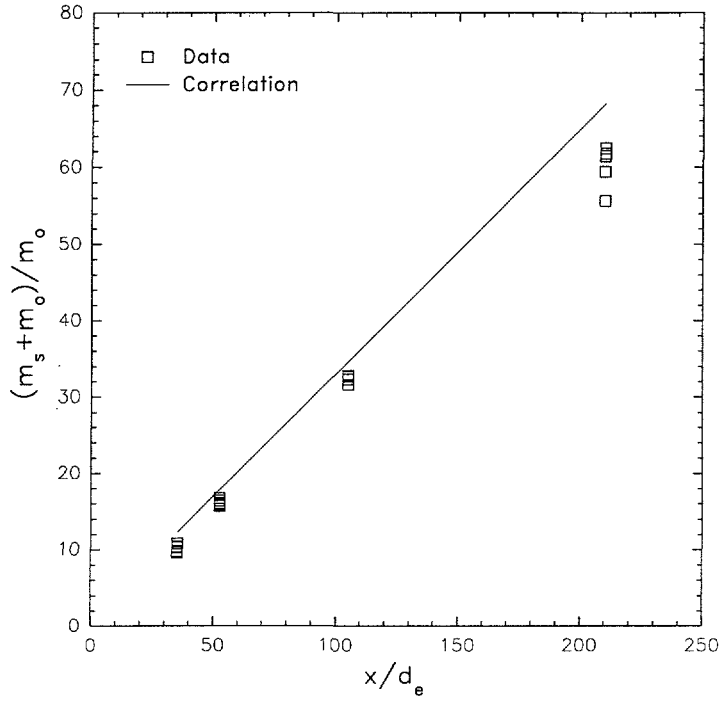

Fig. 9. The mass entrainment ratio, $(m_s+m_o)/m_o$, plotted as a function of the nondimensional distance, x/d_e, for an air jet in an air surrounding gas at ambient temperature. The entrainment measurements compare well with the correlation (Eq. 22).

The dependence of the jet entrainment rate on Reynolds number was investigated for the nonreacting case as well. Ricou and Spalding [21] reported that the ratio of the entrained mass to the jet mass decreased with increasing Reynolds number up $2.5 \cdot 10^4$, then was independent of Reynolds number. A series of isothermal tests using air as the jet and surrounding gas fluids were undertaken to confirm the observations of Ricou and Spalding [21], with the results shown in Fig. 10. The measured ratio, m_s/m_o, is plotted versus the Reynolds number, $Re_o(=U_o d_o/\nu_o)$, of the air jet for several different x/d_o values. In general, for the range of conditions studied, the entrainment ratio, m_s/m_o, was independent of jet Reynolds number. Only for the $x/d_o=210$ case did the m_s/m_o ratio vary slightly with Reynolds number. Thus, an increase in mass entrainment ratio at Reynolds numbers up to $2.5 \cdot 10^4$ was not observed, in conflict with the measurements of Ricou and Spalding [21]. To date, the reason for the discrepancy has not been determined. However, most of the mass entrainment measurements made in this study were taken at jet Reynolds numbers greater than $2.5 \cdot 10^4$.

A series of entrainment measurements were made for several combusting-flow cases. In particular, the entrainment characteristics of a natural gas jet in a high-temperature, dilute/enriched-oxygen environment were studied. Throughout the test series, the natural gas jet Reynolds number was held approximately constant at $Re_o=2.9 \cdot 10^4$, as was the surrounding gas temperature, T_s, at 1368 K (2003°F). Variation in the nondimensional height, x/d_e, was achieved through changes in the injector orifice diameter, the entrainment chamber height and the surrounding gas molecular weight.

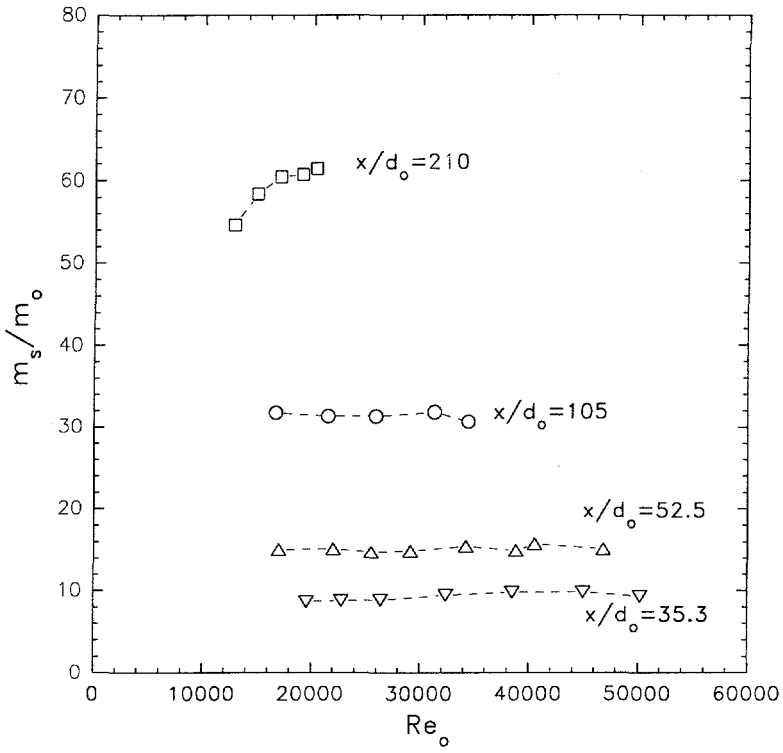

Fig. 10. The ratio of the surrounding gas mass flow rate to the jet mass flow rate, m_s/m_o, plotted as a function of jet Reynolds number, Re_o, and nondimensional height, x/d_o.

The mass entrainment ratio, $(m_s+m_o)/m_o$, plotted as a function of the oxygen content (% vol. wet) in the surrounding gas and x/d_e is shown in Fig. 11 along with the predictions made using Eq. 22. The balance species in the surrounding gas were primarily carbon dioxide and water. It is interesting to note that the mass entrainment ratio decreased with increased oxygen content in the surrounding gas. The mass entrainment predicted by Eq. 22 more closely matched the low-oxygen content results.

It was observed that as the oxygen content of the surrounding gas increased, the visible flame front moved closer to the fuel injector; the flame lift-off distance decreased with increasing oxygen content in the surrounding gas. Thus, it is not unexpected that the correlation developed for nonreacting jets matches the low-oxygen content data since chemical reactions are probably taking place well downstream of the injector. The effect is similar to having a natural gas jet entering into a hot surrounding atmosphere without chemical reactions occurring. As the oxygen level increases, the flame lift-off distance decreases, yielding a combination of a reacting and nonreacting jet inside the entrainment chamber. It is evident from the data in Fig. 11 that an increased degree of reaction leads to lower jet entrainment rates. In general, the entrainment rate decreases by about 30% with an increase in oxygen content from 6.5 to 26.5%. This observation is not unprecedented as Ricou and Spalding [21]

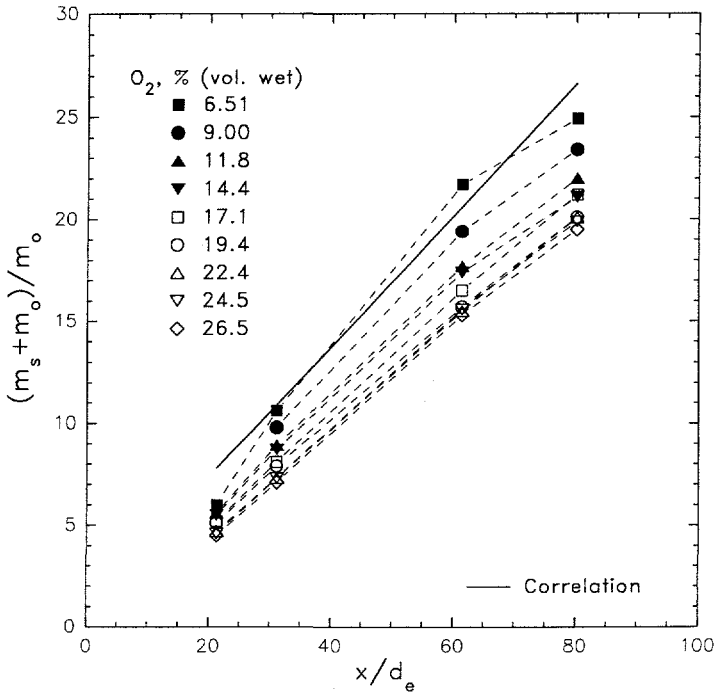

Fig. 11. The mass entrainment ratio, $(m_s+m_o)/m_o$, plotted as a function of the nondimensional height, x/d_e, and the oxygen content of the surrounding gas. The solid line represents a mass entrainment correlation (Eq. 22). The temperature of the surrounding gas was 1368 K.

noted a similar trend. Clemens and Paul [72] in their study of heat release effects on hydrogen diffusion flames provided evidence of a lengthening potential core for reacting conditions as opposed to nonreacting. A longer potential core suggests a decrease in the overall entrainment ratio. The numerical work of Takeno [73] and Yamashita et al. [74] revealed that heat release stabilizes the flow. In a study of methane/air diffusion flames, Chen et al. [75] noted that large-scale fluid motions within the jet do not engulf the reaction zone in the upstream region of the jet. In the hydrogen-nitrogen flames studied by Takagi et al. [76], the upstream jet edges were stabilized by heat release. The observation of a lowered entrainment rate with increased surrounding-gas oxygen content is consistent with the current view of turbulent diffusion flames.

The entrainment data was subsequently evaluated using the d^+ scaling law discussed previously. Recall that the d^+ scaling law allows the use of various correlations developed for nonreacting flows (e.g., Eq. 22) for reacting systems. As shown in Fig. 12, the entrainment data shown previously in Fig. 11 collapses onto the Ricou and Spalding-based correlation given by;

$$\frac{m_s + m_o}{m_o} = 0.32\frac{x}{d^+} + 1 \qquad (23)$$

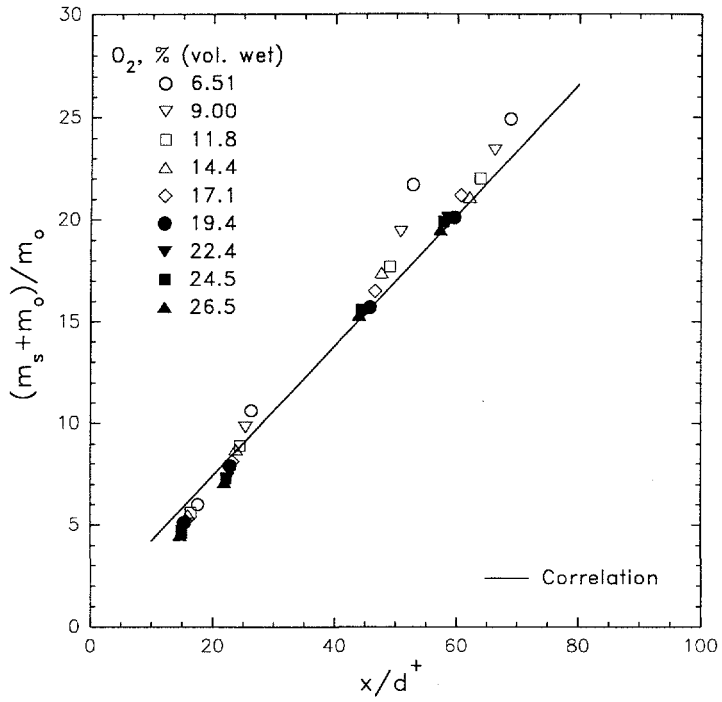

Fig. 12. The mass entrainment ratio, $(m_s+m_o)/m_o$, plotted as a function of the nondimensional height, x/d^+. Use of the d^+ scaling law collapses much of the measured entrainment data onto the correlation given by Eq. 23.

Thus, the mass entrainment of a natural gas jet reacting with a high-temperature, dilute/enriched oxidant can be calculated by incorporating d^+ into the mass entrainment correlation developed under isothermal conditions.

A related series of combusting-flow experiments were undertaken in which the effects of an annular flow of either oxygen or hydrogen on the entrainment and stability characteristics of a natural gas jet in a dilute-oxygen, high-temperature environment were evaluated. For a commercial DOC burner arrangement, it is envisioned that an annular flow of oxygen would provide flame stability under low furnace temperature conditions furnace.

Some of the parameters pertinent to these tests are given in Table 6. Note that the jet velocity of the natural gas jet remained constant (296 m/s), as did the surrounding-gas oxygen concentration (5.71%) and temperature (1388 K). Either hydrogen or oxygen was fed through an annulus coaxial with the fuel tube. Note that the annular flow was included as part of the surrounding gas flow in the entrainment ratio calculations. The effect of the annular flow on the entrainment characteristics of a natural gas jet was evaluated using the acetylene torch method, with the results shown in Fig. 13.

The correlation line in Fig. 13 is straight despite the fact that the surrounding-gas molecular weight changes as a function of the mass flow rate through the annulus. These molecular weight changes are small, hence an average value was used to calculate the mass entrainment ratio based on Eq. 22. As the annulus mass flow rate increased, the amount of surrounding gas entrained by the natural gas jet decreased (15% max).

Table 6. Mass Entrainment/Annular Flow Parameters

Parameter	Value
Jet Fluid	Natural Gas
m_o, kg/s	$4.15 \cdot 10^{-4}$
d_o, mm	1.59
U_o, m/s	296
Stabilizing Fluid	O_2 or H_2
m_{ann}, kg/s	0.0 - $7.5 \cdot 10^{-4}$ (O_2) 0.0 - $5.2 \cdot 10^{-5}$ (H_2)
$d_{ou,ann}$, mm	6.35
$d_{in,ann}$, mm	3.18
U_{ann}, m/s	0 ~ 26 (both H_2 & O_2)
O_2 (surr. gas), % (vol. wet)	5.71
T_s, K	1388

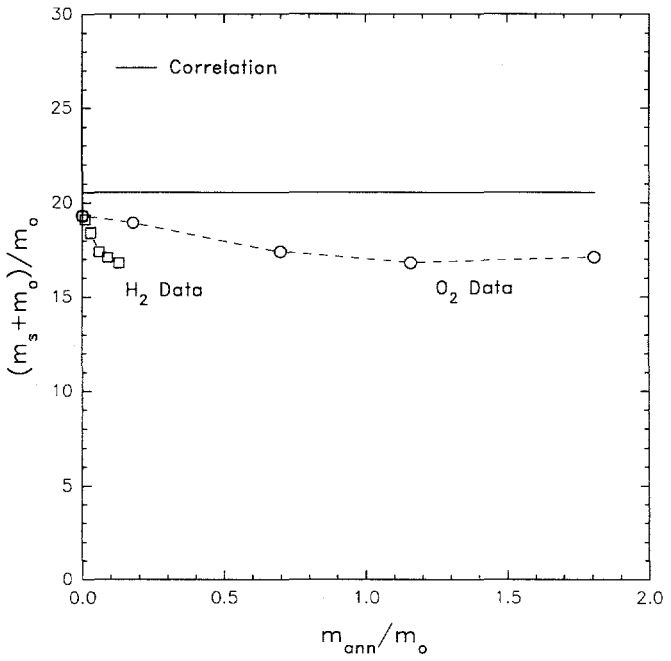

Fig. 13. The mass entrainment ratio plotted as a function of annular mass flow rate (H_2 or O_2). The surrounding-gas oxygen concentration was 5.71% and the surrounding-gas temperature was 1388 K. The solid line represents the mass entrainment correlation given by Eq. 22.

With the addition of the annulus flow of hydrogen or oxygen, a greater degree of reaction within the entrainment chamber can be expected. The increased degree of reaction lead to a decrease in the entrainment ratio; however, the results are clouded by the fact that as the annulus flow increased so did the associated annulus gas velocity potentially affecting the jet entrainment characteristics. Dahm and Dibble [44], in their study of turbulent diffusion flames, observed significant reductions in flame blowout velocities with even small co-flow velocities. Hence, the annulus flow for this study may have "pushed" the reaction zone further downstream of the nozzle as the annulus flow rate was increased. Detailed visual observations were hampered by the entrainment chamber refractory luminosity due to the high temperature. The results shown in both Figs. 11 and 13 are complimentary and suggest that the entrainment appetite of a gas jet is curtailed by the extent of chemical reactions occurring.

5.1.2 Flame Lift-Off Height

Both flame lift-off and flame blowout measurements of a natural gas jet in a high-temperature, dilute/enriched-oxygen environment were attempted; however, viable results for the flame blowout measurements were not acquired for reasons delineated in the experimental section. However, a series of flame lift-off height measurements were made under the aforementioned conditions using the bench-scale apparatus shown in Fig. 5. The windowed-entrainment chamber was employed for this test series, hence the hot surrounding-gas flow was coaxial with the natural gas jet flow.

The flame lift-off height, h, defined as the distance from the injector exit to the base of the luminous flame, was measured as a function of jet velocity, surrounding-gas oxygen content and surrounding-gas temperature. Some of the important parameters of the surrounding-gas flow and the entrainment chamber are given in Table 7.

Table 7. Flame Lift-Off Height Parameters

Parameter	Value
Surrounding Gas	NG/O_2 comb. prod.
Q_s, kW (MMBtu/h)	93.3 (0.318)
Fuel (surr. gas)	Natural Gas
$m_{f,s}$, kg/s	$1.74 \cdot 10^{-3}$
Oxidant (surr. gas)	Oxygen
$m_{ox,s}$, kg/s	$7.45 - 9.49 \cdot 10^{-3}$
T_s, K	1277, 1366
O_2 (surr. gas), % (vol. wet)	7.2 - 22
U_s, m/s	0.31 - 0.37
Jet Fluid	Natural Gas
d_o, mm	1.59
m_o, kg/s	$1.1 - 5.4 \cdot 10^{-4}$

The velocity of the surrounding gas flow, U_s, emanating from the porous disk was low ($\sim$0.35 m/s), and more than enough surrounding gas was supplied to the natural gas jet to satisfy its entrainment appetite. As a matter of reference, the height of the entrainment chamber (the distance from the injector exit to the Inconel insert opening) was 202 mm, or x/d_o=127.

The nondimensional lift-off height, h/d_o, is plotted as a function of the natural gas exit Mach number, M_o, the surrounding-gas oxygen content and the surrounding-gas temperature, T_s , in Fig. 14. The flame lift-off height increased with increasing jet velocity, decreasing oxygen concentration and decreasing gas temperature. All of the results are intuitively expected. It is interesting to note that quite high jet velocities can be achieved without blowing the flame out. For a methane/air diffusion flame, the blowout velocity for a similar injector diameter (1.59 mm) under ambient conditions ($T_s\sim$300 K) is about 25 m/s [43].

For the higher temperature case, T_s=1366 K, the flame lift-off heights were very difficult to ascertain for oxygen concentrations below 7%; hence, no measurements were made. Similarly, for the lower surrounding-gas temperature case, it was not possible to visualize the flame lift-off height for oxygen concentrations below 12%. Flame lift-off measurements for these low oxygen concentrations were hampered due to a lack of contrast

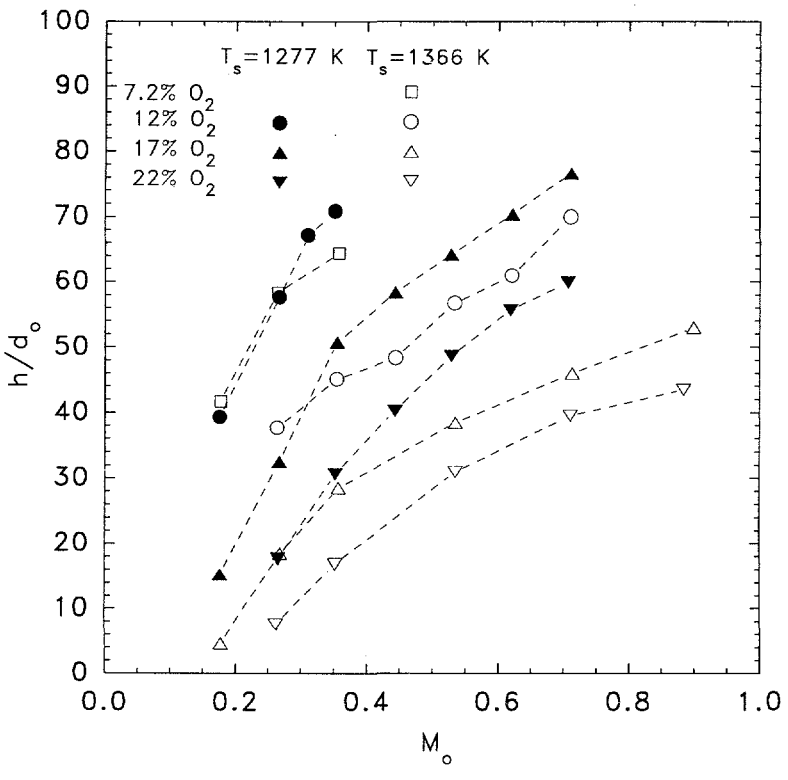

Fig. 14. Nondimensional flame lift-off height measurements, h/d_o, of a natural gas jet in a high-temperature, dilute/enriched-oxygen environment as a function of jet Mach number, M_o.

between the flame luminosity and the hot chamber walls. In addition, the flame was unstable under the aforementioned conditions.

Kalghatgi [38] studied the lift-off behavior of several hydrocarbon fuels in air and ascertained that the lift-off distance was linearly proportional to the exit jet velocity and independent of nozzle diameter. Kalghatgi [38] developed an expression which collapsed all of the hydrocarbon flame lift-off data to a single curve (see Eq. 15). For Kalghatgi's [38] methane case, a nozzle diameter range between 4 and 10 mm, and a velocity range between 25 and 100 m/s were studied. Note that only one injector diameter was tested in this study, d_o=1.59 mm. In addition, recall that Kalghatgi's flame lift-off height relation encompassed a density ratio, $\bar{\rho}$, between 0.5 and 2, while $\bar{\rho}$ for the cases in this study was typically 2.8. In any event, the methane flame lift-off height results obtained by Kalghatgi [38] were compared with the measurements made in this study, as shown in Fig. 15. The lift-off heights measured by Kalghatgi [38] are much larger than those measured in this study. The higher temperature of the surrounding gas has a stabilizing effect on the flame. Note, however, that Kalghatgi [38] performed lift-off measurements in still air, while a coflow of enriched-oxygen combustion products was the environment in this study. As noted by Dahm and Dibble [44], even small coflow velocities significantly reduce the blow-out velocity limits, thus the coflow

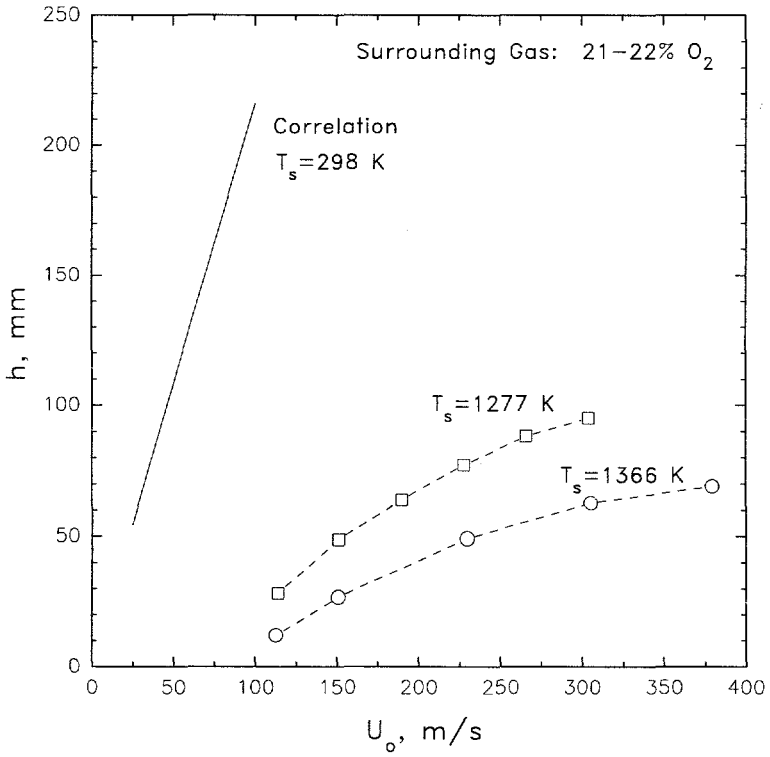

Fig. 15. Flame lift-off height, h, plotted as a function of jet velocity, U_o, and surrounding-gas temperature, T_s. The symbols represent the data acquired in this study, while the solid line represents flame lift-off correlation (methane) developed by Kalghatgi [38].

velocity ($\sim$0.35 m/s) of the hot surrounding gas may have had an influence on the lift-off height measurements in this study, and is an issue which needs further investigation.

5.1.3 Species Measurements

Detailed species measurements along the centerline of the natural gas jet were made as a function of surrounding-gas temperature and oxygen concentration. The measurements were made in the bench-scale apparatus equipped with the windowed-entrainment chamber. The species measured included CO_2, CO, CH_4, H_2, N_2 and O_2, all on a dry basis. The measurements were converted to a wet basis by calculating the amount of water present at the sampling point based on a mass balance. The dependence of CH_4, CO and O_2 mass fractions on axial distance, x/d_o, and surrounding-gas oxygen concentration is shown in Fig. 16 for a constant surrounding-gas temperature of 1370 K. The balance of the surrounding gas composition was carbon dioxide (CO_2) and water (H_2O). Other details regarding the tests are given in Table 8.

For all of the centerline species measurements, the jet mass flow rate was held constant and the surrounding-gas mass flow rate supplied was enough to satisfy the entrainment appetite of the jet. The surrounding-gas oxygen concentration was increased by increasing the flow of the oxygen relative to the fuel to the mixing chamber. This naturally caused an increase in the total surrounding-gas flow rate and the speed with which the surrounding gas flowed coaxially

Table 8. Species Measurements; Bench-Scale Apparatus

Parameter	Value
Surrounding Gas	NG/O_2 comb. prod.
Q_s, kW (MMBtu/h)	93.3 (0.318)
Fuel (surr. gas)	Natural Gas
$m_{f,s}$, kg/s	$1.74 \cdot 10^{-3}$
Oxidant (surr. gas)	Oxygen
$m_{ox,s}$, kg/s	$8.04 - 9.49 \cdot 10^{-3}$
T_s, K	1369
O_2 (surr. gas), % (vol. wet)	12.0 - 22.6
U_s, m/s	0.33 - 0.38
Jet Fluid	Natural Gas
d_o, mm	1.59
m_o, kg/s	$4.17 \cdot 10^{-4}$

with the natural gas jet. However, this variation in surrounding-gas velocity was no greater than 15% (see Table 8).

For all oxygen levels, the amount of methane decreased with distance from the nozzle and increasing oxygen concentration in the surrounding gas (see Fig. 16a). The decrease in methane is due to either mixing with the surrounding gas or chemical reaction. Evident from

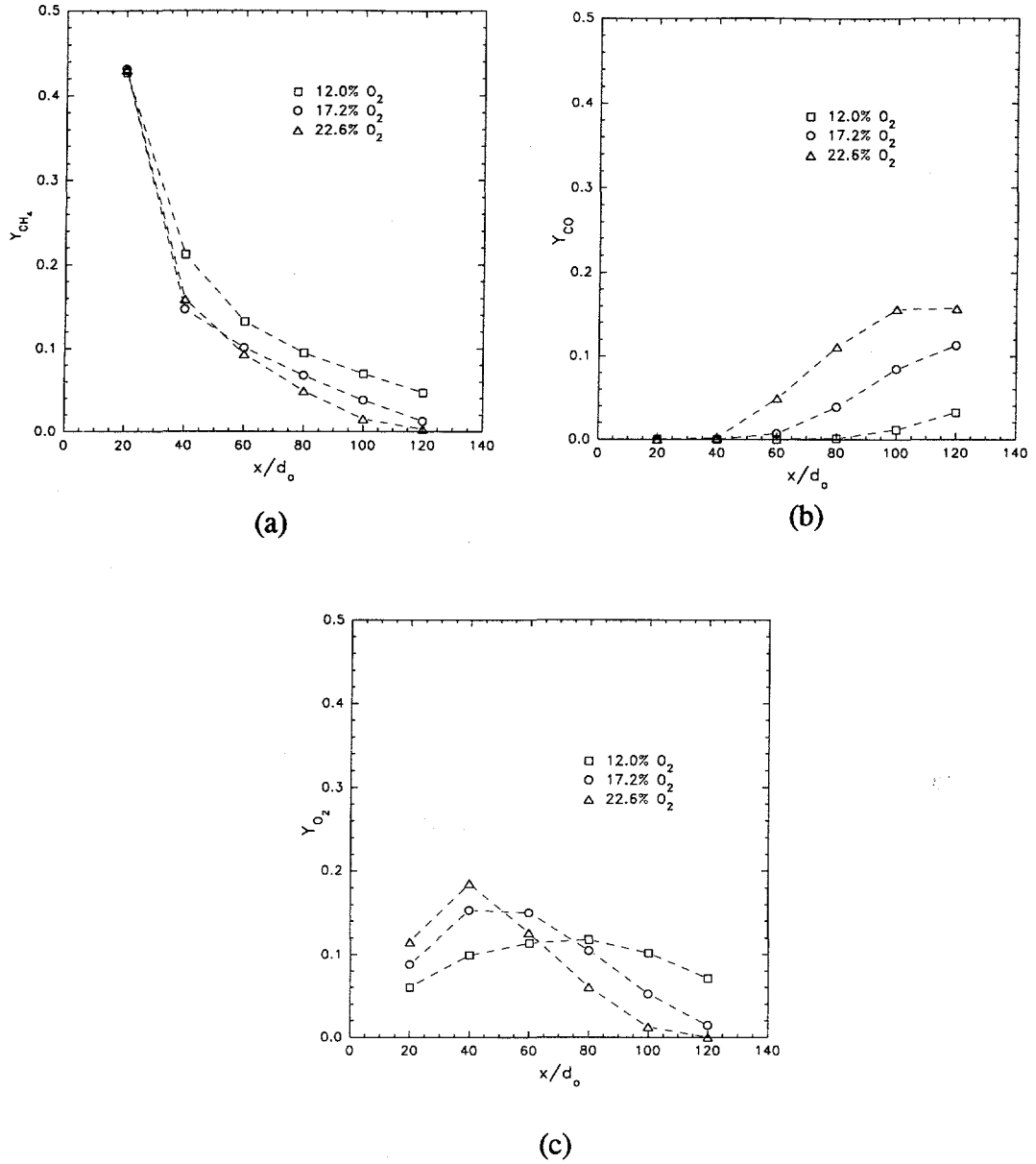

Fig. 16. Species mass fractions, Y_i, measured as a function of nondimensional axial distance along the centerline of a natural gas jet, x/d_o, and oxygen concentration of the surrounding gas. The surrounding-gas temperature was 1369 K. (a) CH_4; (b) CO; (c) O_2.

the CO mass fraction information shown in Fig. 16b is the increased degree of reaction occurring for the higher oxygen levels in the surrounding gas. At least for the 12% O_2 level, it is apparent that much of the injected natural gas is burning outside the entrainment chamber of the bench-scale apparatus.

Oxygen mass fractions are shown in Fig. 16c. In general, the oxygen content along the natural gas jet is significant in the mid-region of the natural gas jet, then decays towards zero

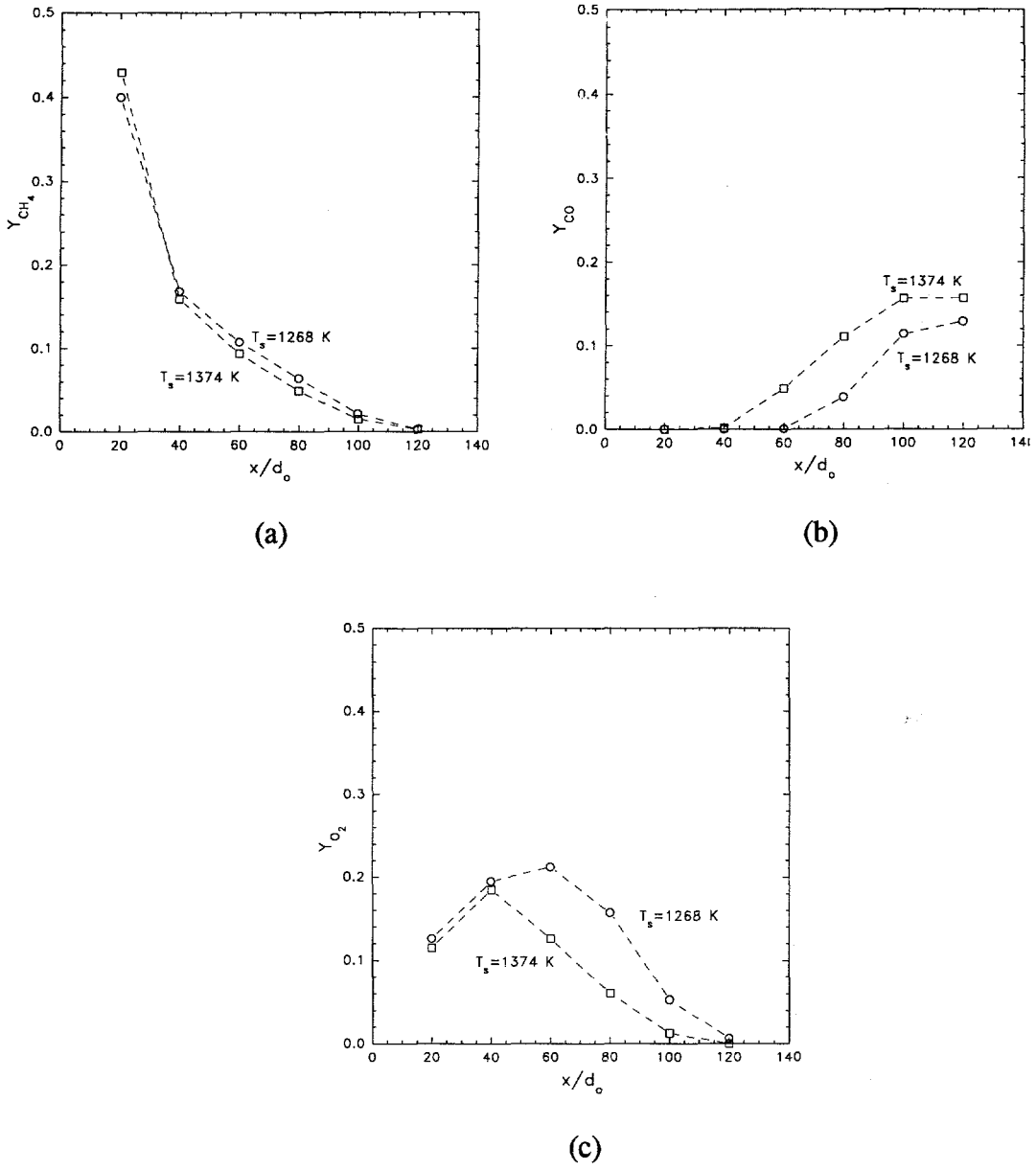

Fig. 17. Species mass fractions, Y_i, measured as a function of nondimensional axial distance along the centerline of a natural gas jet, x/d_o, and surrounding-gas temperature, T_s. The surrounding-gas oxygen concentration was 22%. (a) CH_4; (b) CO; (c) O_2.

with increasing distance from the nozzle. The rate of decrease of the oxygen along the centerline is greater for the higher surrounding-gas oxygen concentrations, indicating an increased level of chemical reactions occurring.

The mass fractions of CH_4, CO and O_2 are plotted as a function of axial distance from the jet nozzle and surrounding-gas temperature in Fig. 17. Note that the oxygen concentration of the surrounding gas was constant at about 22% (vol. wet). It is apparent from the mass fraction curves that a greater degree of chemical reaction has taken place for the higher surrounding-gas temperature case. Carbon monoxide (CO) production is greater for the higher temperature case, and the "consumption" of both methane and oxygen is greater for the higher temperature case.

Clearly, further detailed analyses and expansion of the species database is needed to allow full description of dilute-oxygen flames. In addition, issues such as the affect of the surrounding-gas flow velocity on the flame characteristics needs to be addressed.

5.1.4 Velocity Measurements

As a means of further evaluating dilute oxygen combustion flames, a series of non-intrusive velocity measurements using a laser Doppler velocimeter (LDV) were made. Measurements were made in these reacting flows while varying surrounding-gas temperature and oxygen concentration. The measurements are subsequently compared to nonreacting turbulent jet scaling laws as well as previous flame studies.

As mentioned in the experimental section, seeding the flow was not optimized due to limitations in the seeder apparatus. Seed agglomeration, thus forming large particles, was the largest problem encountered. Seed particles which are too large in size often do not accurately follow the flow [77]. Through repeated cold-flow measurements, seeder settings and seed preparation were optimized to obtain the best results; however, seed agglomeration was a problem not fully resolved.

For all of the velocity measurements, the jet geometric and flow characteristics were held constant. The orifice diameter was 3.81 mm, the jet mass flow rate of natural gas was $6.31 \cdot 10^{-4}$ kg/s which led to an injection velocity of 81.8 m/s. The corresponding surrounding flow parameters are listed in Table 9. Note that the oxygen concentration and the temperature of the surrounding gas were varied. The mass flow rate of the surrounding gas was such that it satisfied the entrainment appetite of the fuel jet. Also notice in Table 9 that the surrounding-gas mass flow rate increased with increases in surrounding-gas oxygen concentration, but varied by no more than 15%. These changing mass flow rates resulted in a varying coaxial gas velocity (0.34 - 0.39 m/s) through the porous disk.

Table. 9. Velocity Measurements; Bench-Scale Apparatus

Parameter	Case A	Case B	Case C	Case D	Case E
Surrounding Gas	CO_2, H_2O & O_2	CO_2, H_2O & O_2	CO_2, H_2O & O_2	CO_2, H_2O & O_2	CO_2, H_2O & O_2
m_s, kg/s	$9.94 \cdot 10^{-3}$	$1.05 \cdot 10^{-2}$	$1.13 \cdot 10^{-2}$	$1.14 \cdot 10^{-2}$	$1.13 \cdot 10^{-2}$
T_s, K	1364	1364	1366	1253	1411
O_2, % (vol. wet)	13.8	18.1	23.1	22.4	22.5
U_s, m/s	0.34	0.35	0.38	0.35	0.39

As mentioned in the experimental section, two-dimensional velocity measurements were made. Due to potential problems related to seed biasing, only a select sample of mean

velocity measurements will be shown here, with further analysis required to assess the appropriateness of the acquired turbulence quantities.

Often times, LDV data is corrected for velocity bias effects. Succinctly, the measured mean velocity values are expected to be unfairly weighted to higher values since a larger number of high-speed particles traverse through the probe volume over a given time interval as compared to the slower moving particles. The methods and their appropriateness for alleviating velocity bias effects for given flow situations has been treated in the literature [78-82]. As pointed out by Phillipart [78], there is not universal agreement on how best to correct for this bias, and even whether it is necessary for all flow situations. For this reason, the velocity measurements reported here were not corrected for velocity biasing effects, but this effect was examined to a limited extent. In summary, the analysis revealed that the raw velocity values were higher than the corrected velocities (time weighted average) by about 10%, with the greatest deviation occurring at the jet periphery.

Measurements of the centerline velocity as function of the surrounding-gas oxygen concentration are shown in Fig. 18, while the specific experimental parameters are listed in Table 9. For the measurements shown in Fig. 18, the surrounding-gas temperature was held constant at 1365 K (1997°F). In addition, the centerline velocity decay expected for nonreacting turbulent jets (Eq. 16) is shown in Fig. 18 for comparison. As the oxygen content of the surrounding gas increased, the centerline velocity increased as well. It is expected that

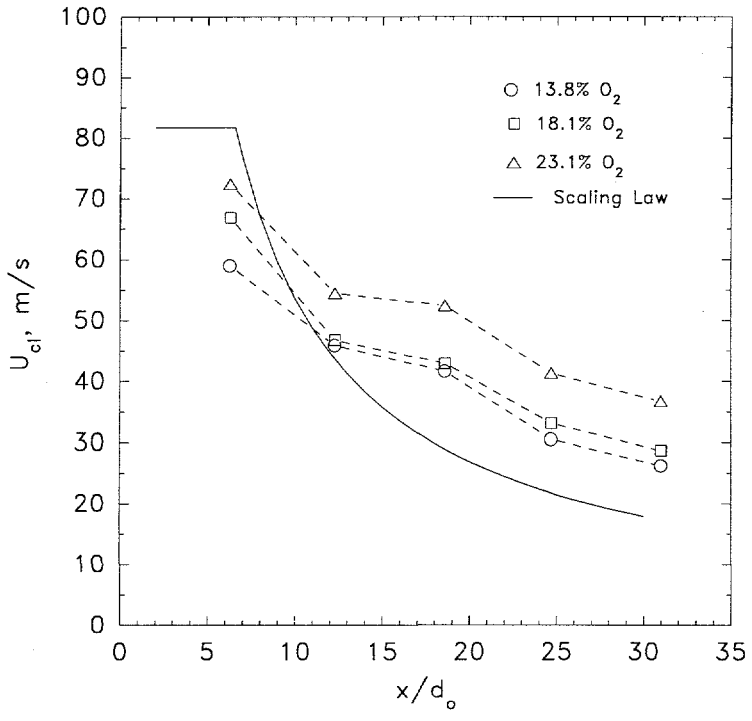

Fig. 18. The measured centerline velocity as a function of nondimensional axial height and surrounding-gas oxygen concentration. The surrounding-gas temperature was 1365 K (1997°F), and the solid line represents a velocity decay scaling law for isothermal jets.

an increase in surrounding-gas oxygen concentration leads to an increased degree of reaction closer to the injector exit plane. Thus, it seems apparent that increased chemical reaction leads to a reduction in the decay of the centerline jet velocity. This observation is supported by the work of Sislian et al. [56] in which they compared the characteristics of turbulent jets under noncombusting and combusting conditions. Sislian et al. [56] observed that the centerline velocity of a noncombusting turbulent jet decreased much more rapidly with increased axial distance than a similar jet under combusting conditions. Sislian et al. [56] attributed the lack of centerline velocity decay for the combusting situation to the expansion of the gases from the temperature rise. Also noted was the suppression of turbulence in the near field of the jet for the combusting case as compared to the nonreacting case. Turbulence is suppressed in the near field of the jet due to the increase in viscosity and the accelerating flow in this region. Similar observations were made by Takagi et al. [54]. The aforementioned trends are also evident in velocity measurements made as a function of jet radial position and surrounding-gas oxygen concentration at several different axial heights as shown in Fig. 19. In all cases, the decay of the flow velocity was reduced as the oxygen concentration in the surrounding gas increased.

A set of centerline velocity measurements were made as a function of surrounding-gas temperature, the results of which are shown in Fig. 20. Once again, the experimental parameters are shown in Table 9. It is expected that an increase in surrounding-gas temperature would result in an increase in flame stability, pushing the reaction zone closer to the fuel injection point, as shown in Fig. 14 (flame lift-off height data). Hence, lower surrounding-gas temperatures would be expected to cause a faster decay in the centerline velocity with increasing axial distance. To some degree, this is shown in Fig. 20. The centerline velocity was greatest for the 1255 K (1800°F) case; however, the velocity magnitude for the 1365 K and the 1411 K cases were quite similar. The centerline velocity decay rates for all combusting cases were slower than predicted by the isothermal jet scaling law, Eq. 16.

Similar to the analysis performed for the mass entrainment measurements, the d^+ scaling concept was evaluated for analyzing the centerline velocity measurements, with the results shown in Fig. 21. A previous study [37] revealed that both nonreacting and reacting centerline velocity data collapsed onto an isothermal jet scaling velocity law as long as the results were formulated in terms of d^+. However here, to a large extent, the measured centerline velocities did not collapse onto the modified scaling law. Agreement between the scaling law and the measurements improved with increasing distance downstream from the injector. Discrepancy between the scaling law and the measurements in the near-field region of the jet is expected due to the inappropriateness of the scaling law in treating near-field phenomena. In addition, inadequacies of seeding the flow (seed agglomeration) may have resulted in biasing the measured mean velocities to lower values.

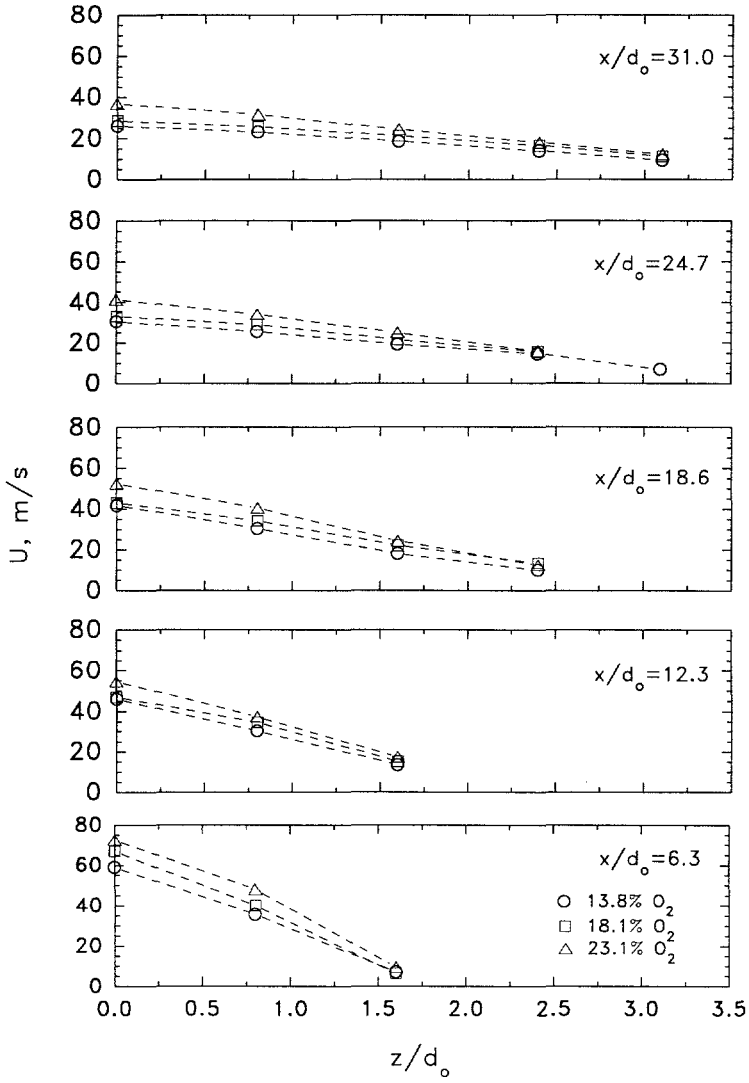

Fig. 19. The measured velocity in a diffusion flame as a function of nondimensional axial position (x/d_o), radial position (z/d_o), and oxygen concentration in the surrounding gas. The surrounding-gas temperature was 1365 K (1997°F).

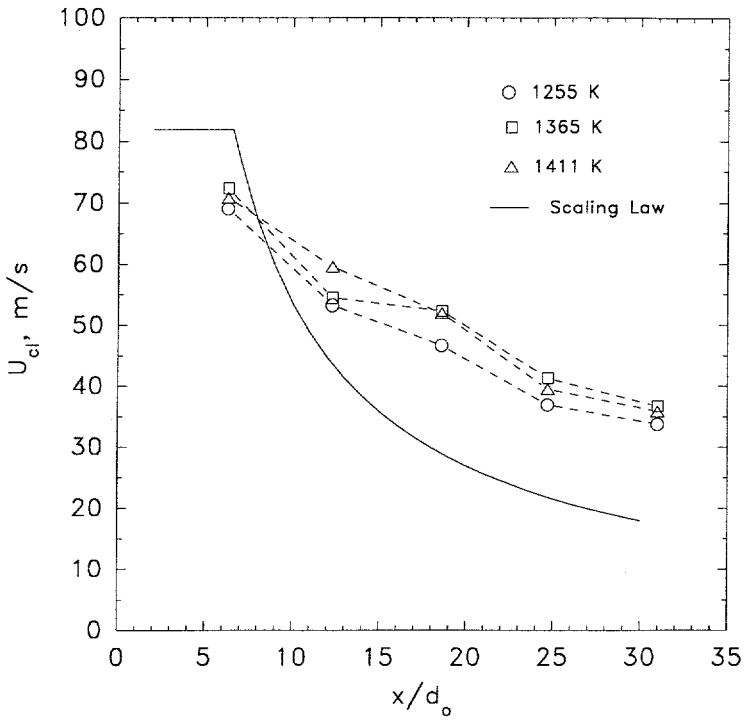

Fig. 20. The measured centerline velocity as a function of nondimensional axial height and surrounding-gas temperature. The surrounding-gas oxygen concentration was nominally 22.7%, and the solid line represents a velocity decay scaling law for isothermal jets.

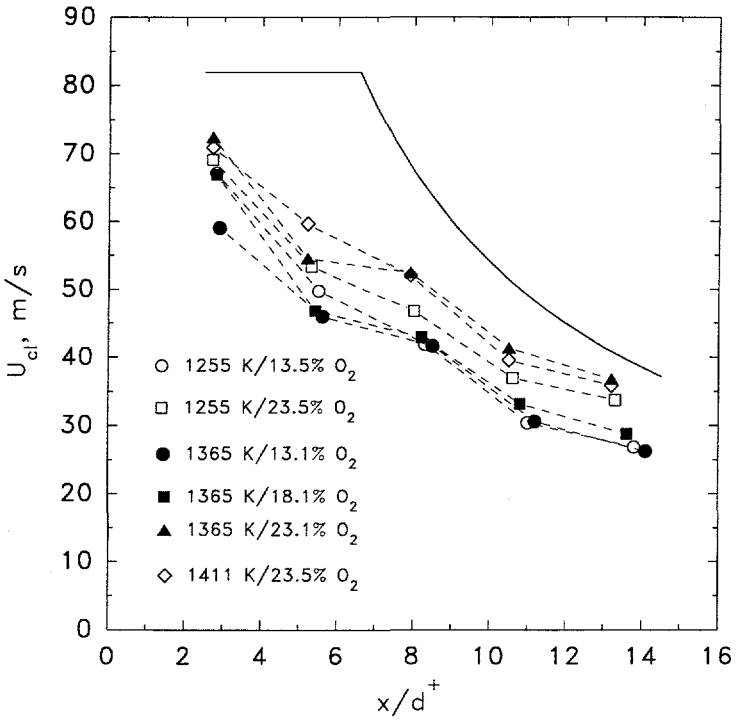

Fig. 21. The measured centerline velocity for a variety of surrounding-gas oxygen concentrations and temperatures plotted as a function of a nondimensional height calculated based on d^+. The solid line represents a centerline velocity decay scaling law for isothermal jets.

5.2 Laboratory-Scale Furnace

The goal of the DOC project is to develop a burner which yields NO_x levels in the single-digit ppm range for conditions typical of commercial high-temperature furnaces (e.g., steel reheat furnace). Prior to development of a pilot-scale or commercial-scale burner, it was evaluated in a laboratory-scale furnace (see Fig. 7) which was rated for firing rates up to 293 kW (1.0 MMBtu/h). The pollutant formation characteristics (e.g., NO_x, CO) of the DOC burner were catalogued as a function of various parameters including, furnace wall temperature, furnace nitrogen content, firing rate, fuel velocity and burner arrangement (geometric). In addition, the combustion stability characteristics of several DOC burners were evaluated.

The NO_x emissions for the tests undertaken are usually expressed on a mass basis (mass of NO_x emitted divided by the amount of fuel energy supplied - see Eq. 19) and a concentration basis. Note that the NO_x concentration values are expressed as an air equivalent value. In other words, the NO_x emissions measured for a given oxy-fuel case were used to calculate what the equivalent concentration of NO_x would be assuming combustion of natural gas and air having an oxygen concentration of 3% (vol. dry) after consumption of the fuel.

5.2.1 Burner Arrangement: Co-Firing Cases

The premise behind the DOC burner is the injection of fuel and oxidant at separate locations within the furnace to encourage reactant dilution. This dilution with combustion products leads to low flame temperatures and, hence, low thermal NO_x production. Since the in-furnace mixing of fuel, oxidant and combustion products is critical, a variety of burner arrangements were studied to ascertain which arrangements (and which general mixing patterns) would lead to low NO_x. The types of burner arrangements can be broadly classified into two categories; arrangements in which the fuel and oxidant were both injected from the front face of the furnace (co-firing) and those arrangements in which the fuel and oxidant were injected from opposite ends of the furnace (opposed-firing). For the most part, natural gas and oxygen were used as reactants; however, air was used as the oxidant for a limited number of tests.

The NO_x emissions for several DOC burner arrangements in which both the fuel and oxidant were positioned on the same face (front) of the furnace are presented first. Nine different arrangements were tested, with the some of the important experimental parameters given in Tables 10a-c. Note that for one case the oxidant stream was delivered into the furnace through two lances (F4F-O3F-O6F). The flow parameters for the oxidant for this case are given in Table 10a for a single lance. For the F7F-F7F-O1F-O3F case, the oxidant was delivered into the furnace through two lances, as was the fuel. In fact, the fuel was delivered into the furnace through the same port (port 7F) with two nozzles; however, the fuel jets were angled away from one another (30° included angle). Again, the flow parameters listed for this case in Table 10b are for a single fuel/oxidant input. For case 7 in Table 10c, the L and R in the burner designation denote the left and right side, respectively, when facing the furnace front face. In fact, the two lances were separated by 152 mm (see Fig. 34).

For the nine different burner arrangements, the furnace wall temperature was kept approximately constant at 1370 K (2007°F), while the oxygen concentration as measured in

the flue was typically between 2-3% (vol. wet). Also note that the fuel and oxidant flow velocities were quite high and that air was the oxidant for cases 8 and 9.

Table 10a. Co-Firing Burner Arrangements

Parameter	Case 1	Case 2	Case 3
Burner Arrangement	F4F-O3F-O6F	F4F-O5F	F6F-O3F
Q, kW (MMBtu/h)	193 (0.659)	185 (0.631)	184 (0.628)
Fuel	Natural Gas	Natural Gas	Natural Gas
m_f, kg/s	$3.60 \cdot 10^{-3}$	$3.45 \cdot 10^{-3}$	$3.44 \cdot 10^{-3}$
U_f, m/s	304	291	290
d_f, mm	4.62	4.62	4.62
Re_f	$9.19 \cdot 10^{4}$	$8.79 \cdot 10^{4}$	$8.77 \cdot 10^{4}$
Oxidant	Oxygen (2 noz.)	Oxygen	Oxygen
m_{ox}/noz., kg/s	$7.11 - 7.92 \cdot 10^{-3}$	$1.41 - 1.56 \cdot 10^{-2}$	$1.39 - 1.56 \cdot 10^{-2}$
U_{ox}, m/s	221-246	225 - 251	224 - 249
d_{ox}, mm	5.51	7.67	7.67
Re_{ox}	$8.21 - 9.14 \cdot 10^{5}$	$1.17 - 1.30 \cdot 10^{5}$	$1.16 - 1.29 \cdot 10^{5}$
T_w, K	1370	1369	1371
Flue O_2, % (vol. wet)	3.18	2.66	2.49
Flue N_2, % (vol. wet)	3.03 - 75.1	3.44 - 77.3	0.97 - 76.2

Table 10b. Co-Firing Burner Arrangements

Parameter	Case 4	Case 5	Case 6
Burner Arrangement	F8F-O3F	F6F-O1F	F7F-F7F-O1F-O3F
Q, kW (MMBtu/h)	184 (0.628)	184 (0.630)	183 (0.625)
Fuel	Natural Gas	Natural Gas	Natural Gas (2 noz.)
m_f/noz., kg/s	$3.43 \cdot 10^{-3}$	$3.44 \cdot 10^{-3}$	$3.42 \cdot 10^{-3}$
U_f, m/s	290	290	286
d_f, mm	4.62	4.62	3.28
Re_f	$8.76 \cdot 10^{4}$	$8.77 \cdot 10^{4}$	$6.14 \cdot 10^{4}$
Oxidant	Oxygen	Oxygen	Oxygen (2 noz.)
m_{ox}/noz., kg/s	$1.36 - 1.55 \cdot 10^{-2}$	$1.33 - 1.53 \cdot 10^{-2}$	$6.64 - 7.62 \cdot 10^{-3}$
U_{ox}, m/s	217 - 249	213 - 246	206 - 237
d_{ox}, mm	7.67	7.67	5.51
Re_{ox}	$1.12 - 1.29 \cdot 10^{5}$	$1.10 - 1.27 \cdot 10^{5}$	$7.67 - 8.80 \cdot 10^{4}$
T_w, K	1367	1370	1369
Flue O_2, % (vol. wet)	2.94	2.56	2.45
Flue N_2, % (vol. wet)	1.46 - 76.7	1.68 - 77.0	0.97 - 77.1

Table 10c. Co-Firing Burner Arrangements

Parameter	Case 7	Case 8	Case 9
Burner Arrangement	F4FL-O4FR	F5F-O7F	F3F-O7F
Q, kW (MMBtu/h)	190 (0.648)	213 (0.727)	215 (0.734)
Fuel	Natural Gas	Natural Gas	Natural Gas
m_f, kg/s	$3.55 \cdot 10^{-3}$	$3.97 \cdot 10^{-3}$	$4.00 \cdot 10^{-3}$
U_f, m/s	300	335	338
d_f, mm	4.62	4.62	4.62
Re_f	$9.06 \cdot 10^{4}$	$1.01 \cdot 10^{5}$	$1.02 \cdot 10^{5}$
Oxidant	Oxygen	Air	Air
m_{ox}, kg/s	$1.41 - 1.55 \cdot 10^{-2}$	$7.45 \cdot 10^{-2}$	$7.45 \cdot 10^{-2}$
U_{ox}, m/s	226-249	266	266
d_{ox}, mm	7.67	17.1	17.1
Re_{ox}	$1.17 - 1.29 \cdot 10^{5}$	$3.07 \cdot 10^{5}$	$3.07 \cdot 10^{5}$
T_w, K	1373	1373	1371
Flue O_2, % (vol. wet)	2.28	2.05	2.07
Flue N_2, % (vol. wet)	2.12-75.7	74.3	74.2

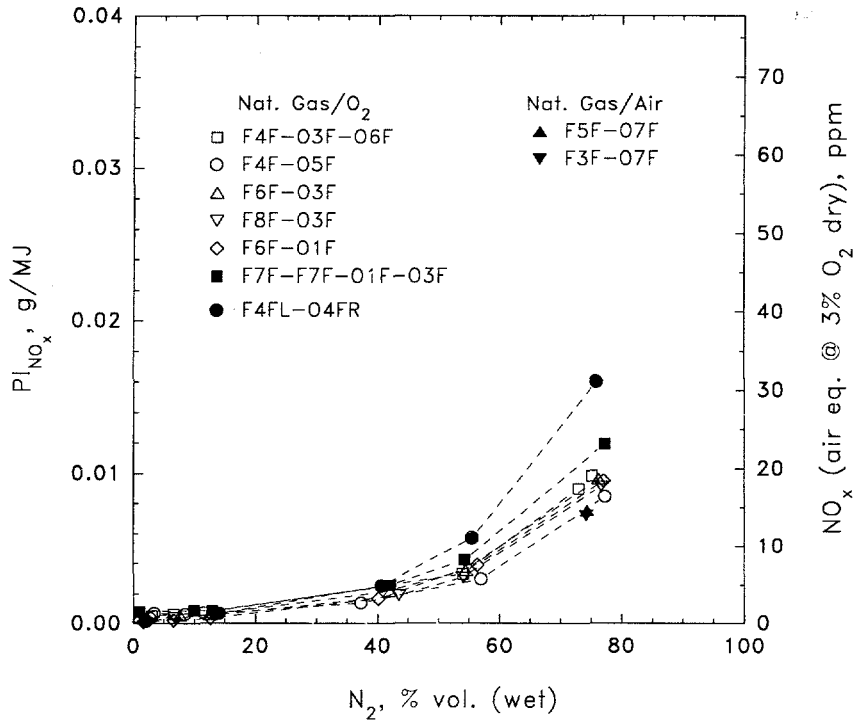

Fig. 22. NO_x emissions for a variety of burner arrangements in which both the fuel and oxidant emanate from the front face of the furnace. Both natural gas/oxygen and natural gas/air cases are shown.

The NO_x emissions are plotted as a function of furnace nitrogen content and burner arrangement in Fig. 22. For furnace nitrogen concentrations below 55%, the NO_x is lower than $5 \cdot 10^{-3}$ g/MJ (air eq. @ 3% O_2 dry - 10 ppm). The dependence of the NO_x emissions on furnace nitrogen content is linear up to nitrogen concentrations of 55%. Interestingly, the NO_x levels for the all of the co-firing burner arrangements are similar for a given furnace N_2 content, including the natural gas/air cases. In general, the CO emissions were low, typically less than 35 ppm. However, for several of the co-firing burner arrangements, CO excursions (detected at the furnace flue) up to approximately 200 ppm (dry) occurred in an apparent periodic manner. In addition, furnace pressure fluctuations were evident.

5.2.2 Burner Arrangement: Opposed-Firing Cases

A series of emission data were collected for burner arrangements in which the fuel and oxidant were introduced into the furnace from opposite ends of the furnace. Some important operational characteristics for the aforementioned cases are given in Tables 11a-b. The operational conditions of these tests were quite similar to those of the co-firing burner arrangements. The furnace wall temperature was held constant at 1371 K (2008°F) and the oxygen concentration at the flue was between 2-3% (vol. wet).

Table 11a. Opposed-Firing Burner Arrangements

Parameter	Case 10	Case 11	Case 12	Case 13
Burner Arrangement	F4F-O1R-O7R	F8F-O3R	F8F-O5R	F3F-O5R
Q, kW (MMBtu/h)	187 (0.638)	187 (0.638)	187 (0.638)	184 (0.630)
Fuel	Natural Gas	Natural Gas	Natural Gas	Natural Gas
m_f, kg/s	$3.49 \cdot 10^{-3}$	$3.48 \cdot 10^{-3}$	$3.48 \cdot 10^{-3}$	$3.44 \cdot 10^{-3}$
U_f, m/s	294	293	294	290
d_f, mm	4.62	4.62	4.62	4.62
Re_f	$8.90 \cdot 10^4$	$8.87 \cdot 10^4$	$8.88 \cdot 10^4$	$8.77 \cdot 10^4$
Oxidant	Oxygen (2 noz.)	Oxygen	Oxygen	Oxygen
m_{ox}/noz., kg/s	$1.40 - 1.62 \cdot 10^{-2}$	$1.41 - 1.61 \cdot 10^{-2}$	$1.40 - 1.61 \cdot 10^{-2}$	$1.33 - 1.53 \cdot 10^{-2}$
U_{ox}, m/s	218 - 251	227 - 257	225 - 258	213 - 246
d_{ox}, mm	5.51	7.67	7.67	7.67
Re_{ox}	$8.09 - 9.34 \cdot 10^4$	$1.17 - 1.33 \cdot 10^5$	$1.16 - 1.33 \cdot 10^5$	$1.10 - 1.27 \cdot 10^5$
T_w, K	1366	1389	1379	1370
Flue O_2, % (vol. wet)	3.02	2.50	2.49	2.56
Flue N_2, % (vol. wet)	0.90 - 73.5	1.13 - 74.6	1.16 - 75.6	1.68 - 77.0

Table 11b. Opposed-Firing Burner Arrangements

Parameter	Case 14	Case 15
Burner Arrangement	F7R-O7F	F3R-O7F
Q, kW (MMBtu/h)	215 (0.734)	215 (0.734)
Fuel	Natural Gas	Natural Gas
m_f, kg/s	$4.00 \cdot 10^{-3}$	$4.00 \cdot 10^{-3}$
U_f, m/s	337	338
d_f, mm	4.62	4.62
Re_f	$1.02 \cdot 10^{5}$	$1.02 \cdot 10^{5}$
Oxidant	Air	Air
m_{ox}, kg/s	$7.45 \cdot 10^{-2}$	$7.45 \cdot 10^{-2}$
U_{ox}, m/s	266	266
d_{ox}, mm	17.1	17.1
Re_{ox}	$3.07 \cdot 10^{5}$	$3.07 \cdot 10^{5}$
T_w, K	1357	1363
Flue O_2, % (vol. wet)	1.84	2.19
Flue N_2, % (vol. wet)	74.2	74.0

The NO_x emissions are plotted as a function of burner arrangement and furnace nitrogen content in Fig. 23. Natural gas and oxygen were the reactants for four of the cases, while natural gas and air were the reactants for two of the cases. In general, the NO_x emission characteristics for the natural gas/oxygen combination were similar. NO_x emissions below $8 \cdot 10^{-3}$ g/MJ ($\sim$15 ppm air eq. @ 3% O_2 dry) were observed for furnace nitrogen concentrations below 55%. Only in one case in which the fuel and oxidant lances were diagonally opposed (F8F-O3R) was the NO_x emission levels higher than the other cases. Relatively low NO_x readings were obtained with the natural gas/air cases. Again, the combustion event was characterized by furnace pressure oscillations; however, the periodic CO excursions were not evident for the opposed-firing burner arrangements.

Upon comparing as a group, the cases in which the fuel and oxidant were delivered into the furnace from the same face (see Fig. 22) to those cases in which the reactants were injected opposed to each other (see Fig. 23), the NO_x emissions were lowest for the former group (co-firing). In addition, all of the air cases exhibited very low NO_x emissions, comparable to the co-firing arrangements at high furnace nitrogen concentrations ($\sim$75% N_2).

The data in Figs. 22 and 23 are plotted on the same scale, and the co-firing NO_x levels are often 30-40% lower than the opposed-firing cases. Low emission levels for the air cases are due to the fact that the oxygen is already significantly diluted with nitrogen prior to entering the furnace in contrast to the case when pure oxygen is directly introduced into the furnace. Recall that dilution of the fuel and oxidant prior to combustion generally leads to low flame temperatures, and hence low NO_x emission levels.

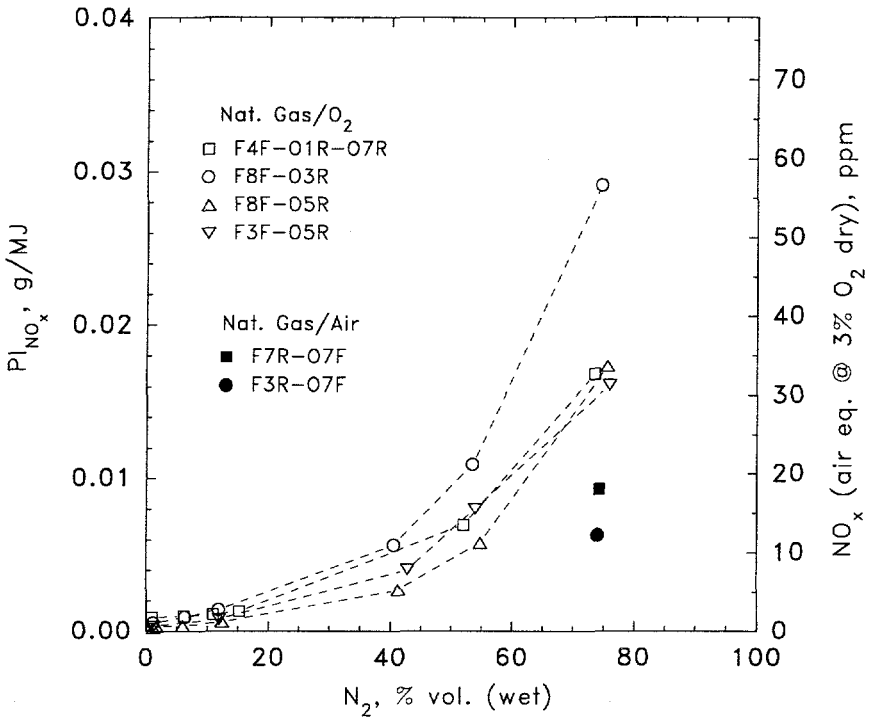

Fig. 23. NO_x emissions as a function of furnace nitrogen content for a variety of burner configurations in which the fuel and oxidant were injected from opposite ends of the furnace.

5.2.3 Furnace Temperature/Nitrogen Content

NO_x formation in strongly dependent on temperature and nitrogen availability. A series of tests were undertaken to establish the NO_x emission characteristics of the DOC burner as a function of furnace nitrogen content and furnace temperature. Specific operational parameters are given in Table 12. The burner arrangement selected for this test series was the F8F-O3F arrangement which was a geometric configuration that exhibited low NO_x (see Fig. 22). In fact, the F8F-O3F arrangement was used for many of the tests to be discussed. The firing rate was approximately 185 kW. The furnace wall temperature was varied from 1100 to 1550 K, the furnace nitrogen content was varied from 1 to 77% (vol. wet), and the oxygen concentration in the flue was held to a nominal value of 2.5% (vol. wet).

The sensitivity of NO_x pollutant formation for the F8F-O3F burner arrangement as a function of furnace wall temperature and nitrogen content is shown in Fig. 24. NO_x emissions under $3 \cdot 10^{-3}$ g/MJ (~9 ppm air equiv. @ 3% O_2 dry) were acquired throughout the entire test temperature range for furnace nitrogen levels under 40%. NO_x increased with increasing

Table 12. Furnace Temperature and Nitrogen Variation

Parameter	Case 16	Case 17	Case 4	Case 18
Burner Arrangement	F8F-O3F	F8F-O3F	F8F-O3F	F8F-O3F
Q, kW (MMBtu/h)	186 (0.635)	186 (0.635)	184 (0.628)	198 (0.676)
Fuel	Natural Gas	Natural Gas	Natural Gas	Natural Gas
m_f, kg/s	$3.47 \cdot 10^{-3}$	$3.47 \cdot 10^{-3}$	$3.43 \cdot 10^{-3}$	$3.69 \cdot 10^{-3}$
U_f, m/s	293	293	290	311
d_f, mm	4.62	4.62	4.62	4.62
Re_f	$8.85 \cdot 10^{4}$	$8.85 \cdot 10^{4}$	$8.76 \cdot 10^{4}$	$9.41 \cdot 10^{4}$
Oxidant	Oxygen	Oxygen	Oxygen	Oxygen
m_{ox}, kg/s	$1.34 - 1.53 \cdot 10^{-2}$	$1.35 - 1.47 \cdot 10^{-2}$	$1.36 - 1.55 \cdot 10^{-2}$	$1.45 - 1.67 \cdot 10^{-2}$
U_{ox}, m/s	215 - 245	216 - 236	217 - 249	232 - 267
d_{ox}, mm	7.67	7.67	7.67	7.67
Re_{ox}	$1.11 - 1.27 \cdot 10^{5}$	$1.12 - 1.22 \cdot 10^{5}$	$1.12 - 1.29 \cdot 10^{5}$	$1.20 - 1.38 \cdot 10^{5}$
T_w, K	1177	1260	1367	1525
Flue O_2, % (vol. wet)	3.12	2.71	2.94	2.76
Flue N_2, % (vol. wet)	0.87 - 77.0	1.27 - 76.6	1.46 - 76.7	1.75 - 75.7

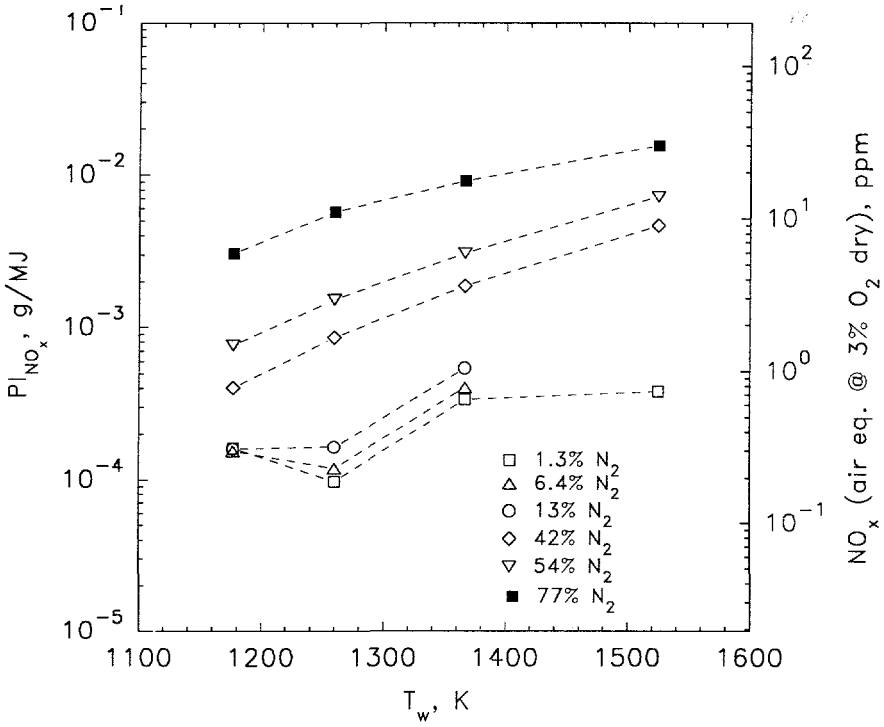

Fig. 24. The NO_x emissions plotted as a function of furnace nitrogen content (vol. wet) and furnace wall temperature, T_w.

nitrogen content and furnace wall temperature, as expected. For several of the low nitrogen levels (1.3 and 6.4%), the NO_x apparently decreased with an increase in furnace wall temperature (see Fig. 24). This effect is probably an artifact of the manner in which the furnace was heated prior to initiating DOC burner testing. As mentioned in the experimental section, the furnace was heated to above the reactant auto-ignition temperature using a low-NO_x burner. At times it was found that if a large amount of NO_x was generated during furnace heating, it took a relatively long time to purge the furnace of NO_x to single digit ppm levels.

The NO_x emission data shown in Figs. 22-24 allude to the fact that the DOC burner will be competitive in terms of NO_x emissions as compared to current-technology low-NO_x air burners, even for partial oxy-fuel conversions. In fact, as shown in Figs. 22-23, relatively low NO_x emissions resulted even when the natural gas and air were the primary reactants.

5.2.4 Firing Rate

The dependence of the NO_x formation rate on firing rate was tested to a limited extent. The two firing rates evaluated were 184 and 286 kW. For both of these cases, the burner arrangement (F8F-O3F), furnace temperature (1365 K) and oxygen concentration (2.60%) in the flue were all held constant. Once again, the furnace nitrogen content was varied from 1 to 77%. A further delineation of test conditions is given in Table 13.

As shown in Fig. 25, the measured NO_x emissions did not strongly depend on the firing rate. An increase in the firing rate results in an increase in jet momentum of both the fuel and oxidant; however, this increase did not seem to significantly alter the furnace mixing thus altering the pollutant emissions. In any event, testing at higher firing rates (i.e., pilot scale) is necessary to further evaluate the emission characteristics of the DOC burner.

Table 13. Firing Rate Variation

Parameter	Case 4	Case 19
Burner Arrangement	F8F-O3F	F8F-O3F
Q, kW (MMBtu/h)	184 (0.628)	286 (0.976)
Fuel	Natural Gas	Natural Gas
m_f, kg/s	$3.43 \cdot 10^{-3}$	$5.33 \cdot 10^{-3}$
U_f, m/s	290	272
d_f, mm	4.62	5.94
Re_f	$8.76 \cdot 10^{4}$	$1.06 \cdot 10^{5}$
Oxidant	Oxygen	Oxygen
m_{ox}, kg/s	$1.36 - 1.55 \cdot 10^{-2}$	$2.12 - 2.34 \cdot 10^{-2}$
U_{ox}, m/s	217 - 249	213 - 236
d_{ox}, mm	7.67	9.68
Re_{ox}	$1.12 - 1.29 \cdot 10^{5}$	$1.39 - 1.54 \cdot 10^{5}$
T_w, K	1367	1362
Flue O_2, % (vol. wet)	2.94	2.25
Flue N_2, % (vol. wet)	1.46 - 76.7	1.05 - 67.7

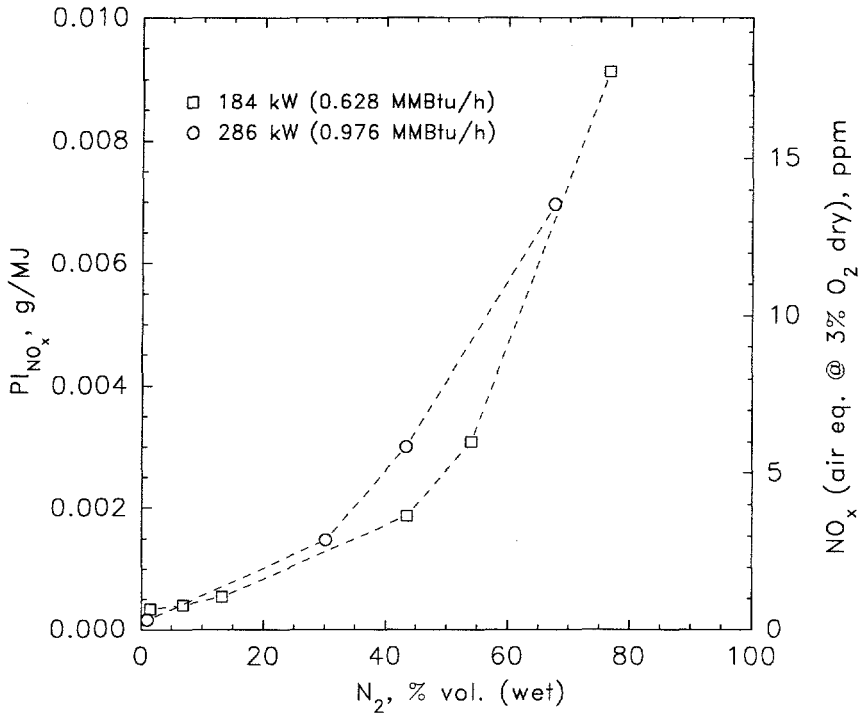

Fig. 25. The NO_x emissions plotted as a function of furnace nitrogen content and burner firing rate.

5.2.5 Fuel Injection Velocity

The sensitivity of NO_x formation to variation in the fuel injection velocity was investigated as well. The three injection velocities were 133, 179 and 290 m/s (see Table 14). For all three cases, the firing rate was kept constant, as was the furnace wall temperature ($\sim$1364 K) and the oxygen concentration (2.5% O_2 vol. wet) at the flue. The burner arrangement was F8F-O3F. For the range of fuel injection velocities tested, a significant change in NO_x emissions did not occur, as shown in Fig. 26.

5.2.6 Burner Type

The NO_x characteristics of three burner types were evaluated, including a coaxial-tube, a staged coaxial-tube and a DOC burner, as a function of furnace nitrogen content. Note that the firing rate, furnace temperature and oxygen concentration (at the flue) were all held constant, with the specific values given in Table 15. The coaxial-tube burner consisted of two concentric tubes with fuel flowing through the inner tube, and oxidant flowing through the outer annulus. The staged coaxial-tube burner consisted of a coaxial tube burner with oxidant staging. Approximately 70% of the oxidant was fed through the staging lance located in port 5F. For the DOC burner, both the fuel and oxidant were injected from the front face of the furnace (F8F-O3F arrangement). In Table 15, $m_{ox,ann}$ and other related flow parameters represent the oxidant flow through the annulus around the fuel tube.

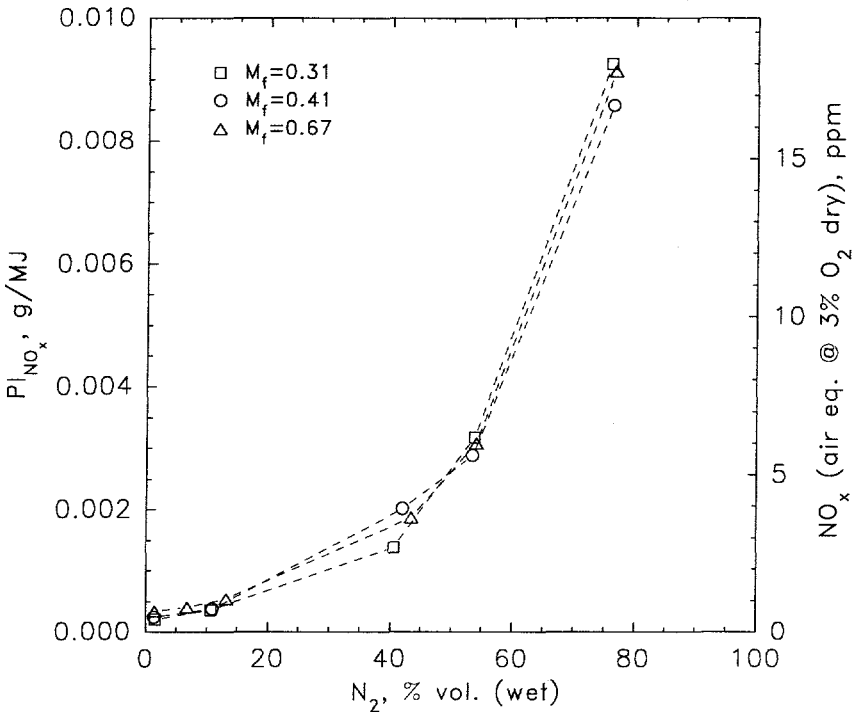

Fig. 26. The NO_x emissions plotted as a function of furnace nitrogen content and fuel Mach number, M_f.

Table 14. Fuel Injection Velocity Variation

Parameter	Case 20	Case 21	Case 4
Burner Arrangement	F8F-O3F	F8F-O3F	F8F-O3F
Q, kW (MMBtu/h)	187 (0.638)	187 (0.638)	184 (0.628)
Fuel	Natural Gas	Natural Gas	Natural Gas
m_f, kg/s	$3.48 \cdot 10^{-3}$	$3.49 \cdot 10^{-3}$	$3.43 \cdot 10^{-3}$
U_f, m/s	133	179	290
d_f, mm	6.86	5.94	4.62
Re_f	$5.99 \cdot 10^{4}$	$6.92 \cdot 10^{4}$	$8.76 \cdot 10^{4}$
Oxidant	Oxygen	Oxygen	Oxygen
m_{ox}, kg/s	$1.37 - 1.54 \cdot 10^{-2}$	$1.37 - 1.51 \cdot 10^{-2}$	$1.36 - 1.55 \cdot 10^{-2}$
U_{ox}, m/s	220 - 246	220 - 242	217 - 249
d_{ox}, mm	7.67	7.67	7.67
Re_{ox}	$1.14 - 1.28 \cdot 10^{5}$	$1.14 - 1.25 \cdot 10^{5}$	$1.12 - 1.29 \cdot 10^{5}$
T_w, K	1360	1366	1367
Flue O_2, % (vol. wet)	2.39	2.24	2.94
Flue N_2, % (vol. wet)	1.56 - 76.0	1.42 - 76.3	1.46 - 76.7

Table 15. Burner Type Variation

Parameter	Case 22	Case 23	Case 4
Burner Type	Coaxial-tube	Staged coaxial-tube	DOC
Burner Arrangement	F4F-O4F	F4F-O4F-O5F	F8F-O3F
Q, kW (MMBtu/h)	185 (0.631)	187 (0.638)	184 (0.628)
Fuel	Natural Gas	Natural Gas	Natural Gas
m_f, kg/s	$3.45 \cdot 10^{-3}$	$3.49 \cdot 10^{-3}$	$3.43 \cdot 10^{-3}$
U_f, m/s	81.5	82.4	290
d_f, mm	8.74	8.74	4.62
Re_f	$4.66 \cdot 10^{4}$	$4.71 \cdot 10^{4}$	$8.76 \cdot 10^{4}$
Oxidant	Oxygen	Oxygen	Oxygen
m_{ox}, kg/s (lance)	N/A	$1.03 \cdot 10^{-2}$	$1.36 - 1.55 \cdot 10^{-2}$
d_{ox}, mm	N/A	7.67	7.67
U_{ox}, m/s	N/A	164	217 - 249
$m_{ox,\,ann}$, kg/s (annulus)	$1.39 \cdot 10^{-2}$	$4.29 \cdot 10^{-3}$	N/A
$d_{ox,ann,in}$, mm	33.4	33.4	N/A
$d_{ox,ann,ou}$, mm	66.9	66.9	N/A
$U_{ox,ann}$, m/s	3.91	1.2	N/A
T_w, K	1371	1368	1367
Flue O_2, % (vol. wet)	2.19	2.19	2.94
Flue N_2, % (vol. wet)	1.08 - 14.3	1.34 - 10.5	1.46 - 76.7

In general, the NO_x emissions of the coaxial-tube burner were about an order of magnitude greater than those of the staged coaxial-tube burner, and the NO_x emissions of the staged coaxial-tube burner were about an order of magnitude greater than those of the DOC burner, as shown in Fig. 27. However, for low nitrogen levels ($<10\%$), the NO_x emissions are quite low for both the staged coaxial-tube and DOC burners (<10 ppm air equivalent at 3% O_2 dry).

5.2.7 Species Measurement

In-furnace species measurements were made to unveil the mixing and combustion processes occurring within the furnace for several of the DOC burner arrangements. In particular, the concentration of oxygen, methane and carbon monoxide were of primary interest for the reactant combination of natural gas and oxygen. Detailed species concentration measurements were made within the laboratory-scale furnace (see Fig. 7) for four different burner arrangements. Information regarding the burner/furnace operating parameters is given in Table 16. For all of the furnace probing measurements, the furnace temperature and flue oxygen concentration were held approximately constant at 1369 K and 2.5% (vol. wet), respectively. The four burner arrangements consisted of two co-firing cases (F6F-O1F and F4FL-O4FR), and two opposed-firing cases (F6F-O7R and F6F-O1R). For all arrangements,

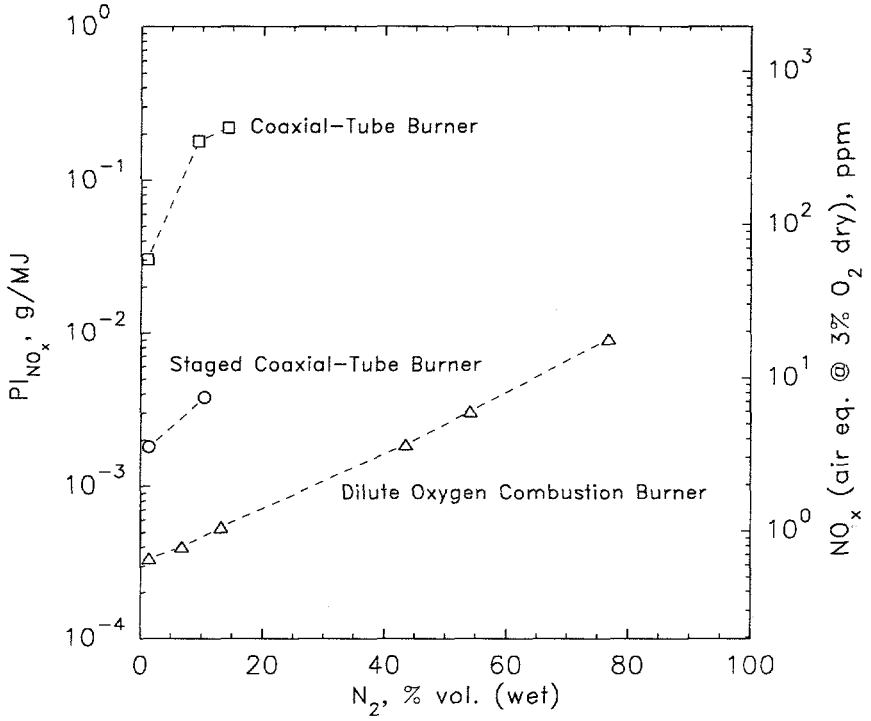

Fig. 27. The NO_x emissions plotted as a function of furnace nitrogen content for three burner types.

nitrogen was not supplied to the furnace and species measurements were made along three planes of the furnace corresponding to the planes in which the lower (L), middle (M) and upper (U) sample ports lie in (see Fig. 8). In each plane, the species measurement locations are marked by solid circles, with the measured concentrations listed next to each circle. The species contour levels were interpolated (Kriging method) based on the measurements [83, 84]. The coordinate system associated with these measurements is given in Fig. 8. The axial distance, x, along the furnace has been nondimensionalized with the furnace length, L (=3.2 m), while the transverse dimension, z, has been nondimensionalized with the furnace radius, R (=0.457 m). In addition, the location of the fuel and oxidant input streams as well as the flue are shown in the graphs to follow. Burner arrangements having similar geometric configurations were evaluated in terms of NO_x emissions as a function of nitrogen content (see Figs. 22-23).

The results for the burner arrangement F6F-O1F are discussed first. Information regarding the oxygen distribution within the lower, middle and upper furnace planes is shown in Fig. 28. For this burner arrangement, detailed probing was performed near the fuel and oxygen jets. Because of the large number of points in the jet vicinity, oxygen concentration values in these region are not shown in Fig. 28, but given in Figs. 29 and 30.

Table 16. Laboratory-Scale Furnace Species Measurements

Parameter	Case 24	Case 25	Case 26	Case 27
Burner Arrangement	F6F-O1F	F4FL-O4FR	F6F-O7R	F6F-O1R
Q, kW (MMBtu/h)	194 (0.662)	189 (0.645)	188 (0.642)	189 (0.645)
Fuel	Natural Gas	Natural Gas	Natural Gas	Natural Gas
m_f, kg/s	$3.6 \cdot 10^{-3}$	$3.53 \cdot 10^{-3}$	$3.51 \cdot 10^{-3}$	$3.52 \cdot 10^{-3}$
U_f, m/s	305	298	296	297
d_f, mm	4.57	4.57	4.57	4.57
Re_f	$9.21 \cdot 10^{4}$	$9.00 \cdot 10^{4}$	$8.96 \cdot 10^{4}$	$8.97 \cdot 10^{4}$
Oxidant	Oxygen	Oxygen	Oxygen	Oxygen
m_{ox}, kg/s	$1.39 \cdot 10^{-2}$	$1.39 \cdot 10^{-2}$	$1.40 \cdot 10^{-2}$	$1.41 \cdot 10^{-2}$
U_{ox}, m/s	222	222	225	227
d_{ox}, mm	7.67	7.67	7.67	7.67
Re_{ox}	$1.15 \cdot 10^{5}$	$1.15 \cdot 10^{5}$	$1.17 \cdot 10^{5}$	$1.17 \cdot 10^{5}$
T_w, K	1369	1371	1370	1368
Flue O_2, % (vol. wet)	2.82	2.05	2.53	2.15
Flue N_2, % (vol. wet)	0.00	0.00	0.00	0.00
# Sample Points	80	48	23	21

Evident from the data in the lower furnace plane was the lack of oxygen over a large area of the furnace ($-1 < z/R < 1$; $0 < x/L < 0.5$). Note that the fuel lance was in this plane. This effect was evident in the middle furnace plane as well. Oxygen was injected in the upper furnace plane, and the oxygen concentration measured at the flue exit was 2.82% (vol. wet). In general, the interpolation procedure for generating the different oxygen contours yielded believable trends.

The measured CO concentrations for the F6F-O1F arrangement are shown in Fig. 31, with the detailed CO distribution near the reactant inputs given in Figs. 29 and 30. The extensive furnace probing revealed a predominance of CO (0.5 ~ 1%) present in half of the furnace. The high CO concentrations were associated with the lower and middle furnace planes. Recall from Fig. 28 that this is the same region in which very little oxygen was present.

The measured distribution of CH_4 is shown in Fig. 32 and that of H_2 in Fig. 33. Recall that natural gas was used as the fuel, which contained 95.6% CH_4 and 0.0% H_2 (see Table 4). Thus, the measured hydrogen is from the breakdown of the natural gas. Both methane and hydrogen were found in measurable quantities in the front half (near the lances) of the furnace. The hydrogen concentrations were on the same order as the CO concentrations.

Detailed in-furnace species measurements were taken for the F4FL-O4FR burner arrangement, a co-firing arrangement having a lance separation distance of 152 mm. Measurements of O_2, CO and CH_4 for this arrangement are given in Figs. 34-36, respectively. Succinctly, similar trends observed for the F6F-O1F case were observed for this arrangement. For example, once again, there is a predominance of CO (see Fig. 35) distributed throughout

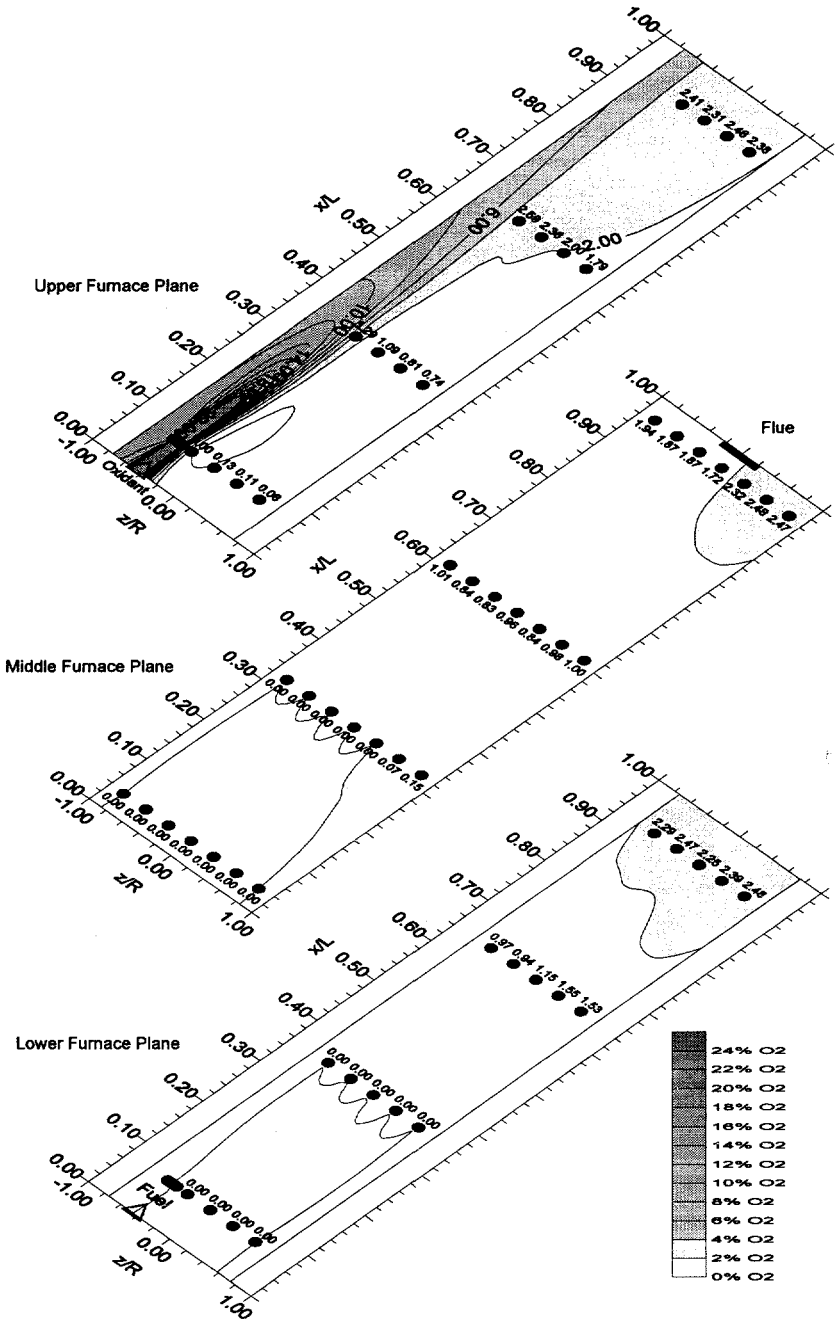

Fig. 28. Oxygen concentration measurements (% vol. wet) as a function of furnace location for the co-firing burner arrangement F6F-O1F. The solid circles represent the measurement locations with the measured O_2 values listed next to them. The contours were interpolated from the measurements.

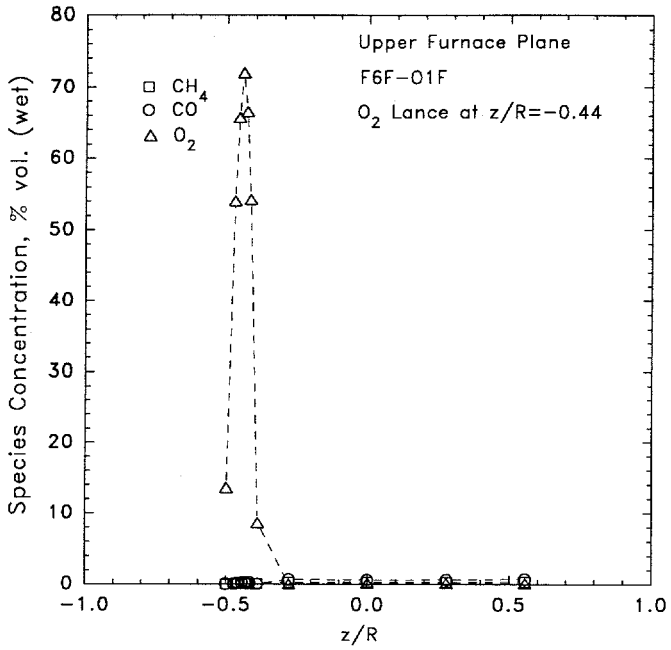

Fig. 29. Measured species concentrations as a function of z/R at $x/L=0.071$ for the upper furnace plane. The burner arrangement is F6F-O1F.

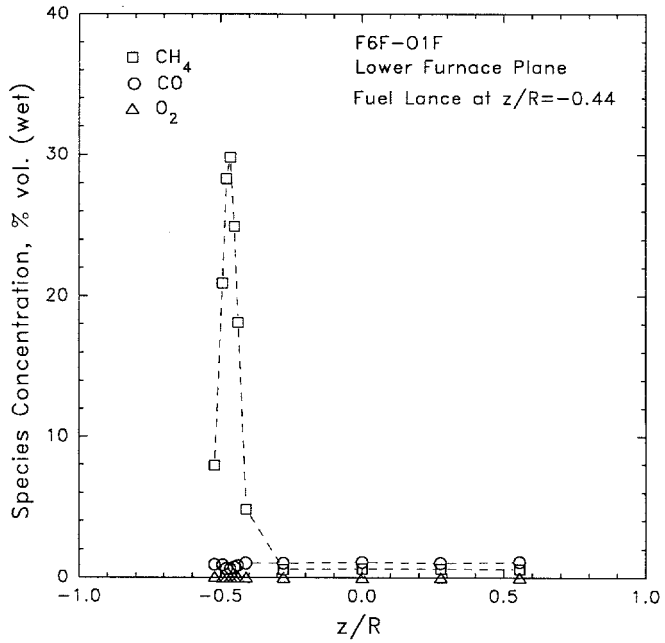

Fig. 30. Measured species concentrations as a function of z/R at $x/L=0.071$ for the lower furnace plane. The burner arrangement is F6F-O1F.

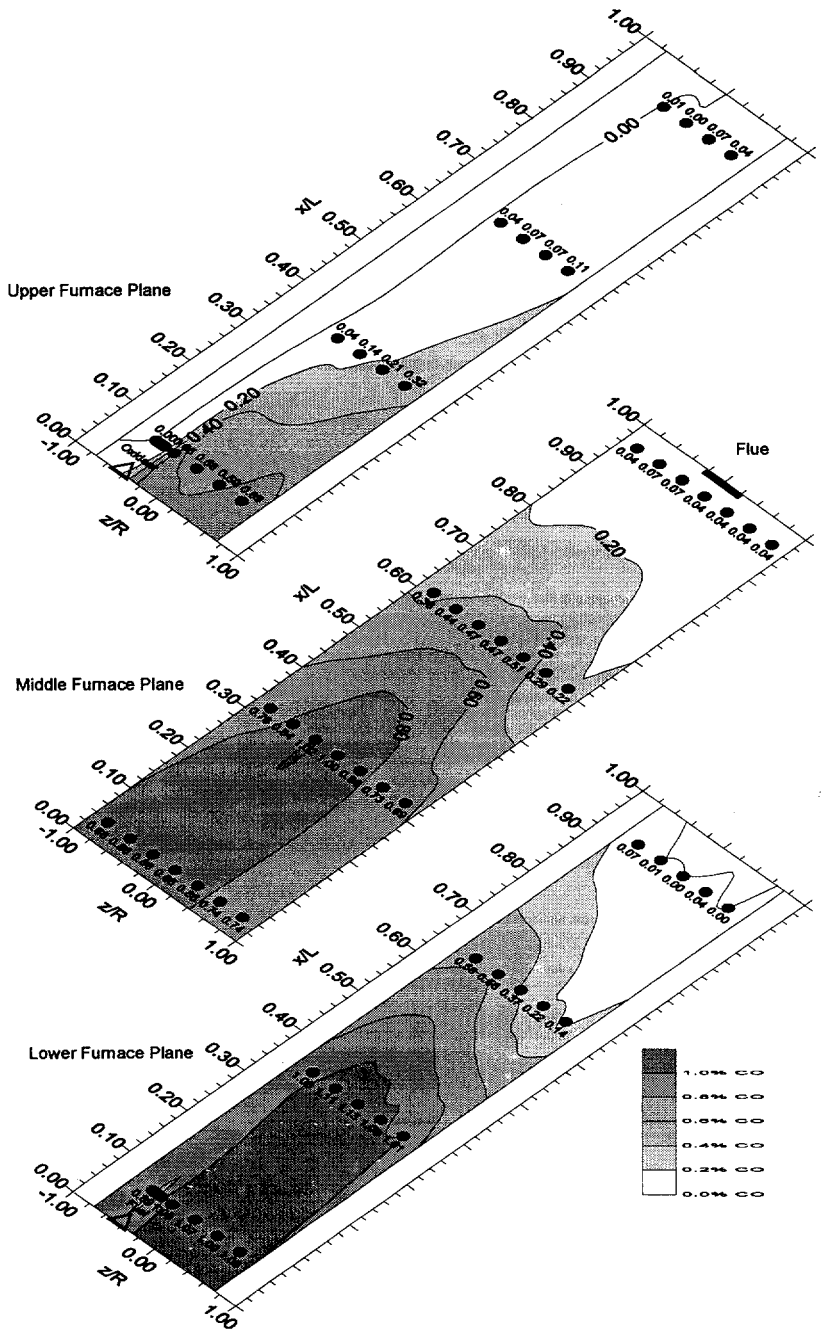

Fig. 31. Carbon monoxide concentration measurements (% vol. wet) as a function of furnace location for the co-firing burner arrangement F6F-O1F. The solid circles represent the measurement locations with the measured CO values listed next to them. The contours were interpolated from the measurements.

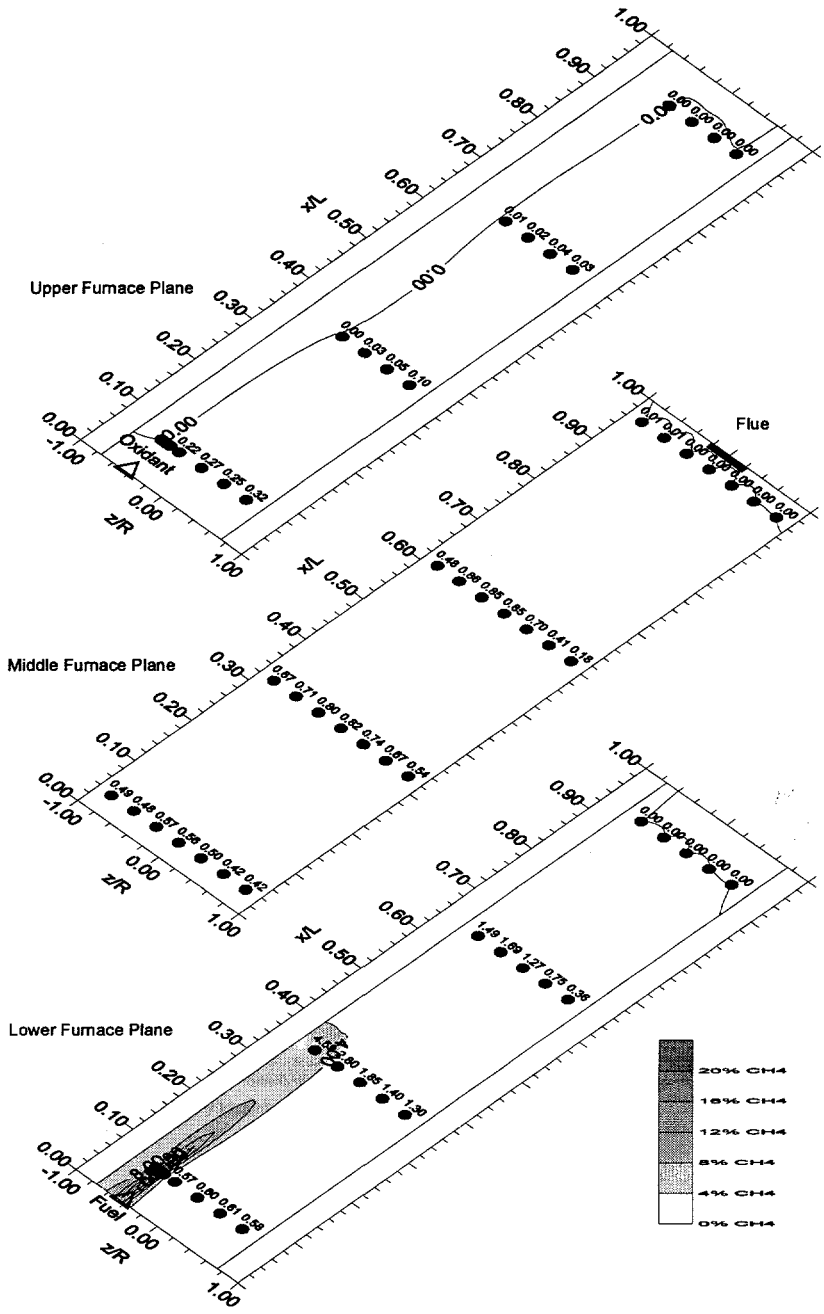

Fig. 32. Methane concentration measurements (% vol. wet) as a function of furnace location for the co-firing burner arrangement F6F-O1F. The solid circles represent the measurement locations with the measured CH_4 values listed next to them. The contours were interpolated from the measurements.

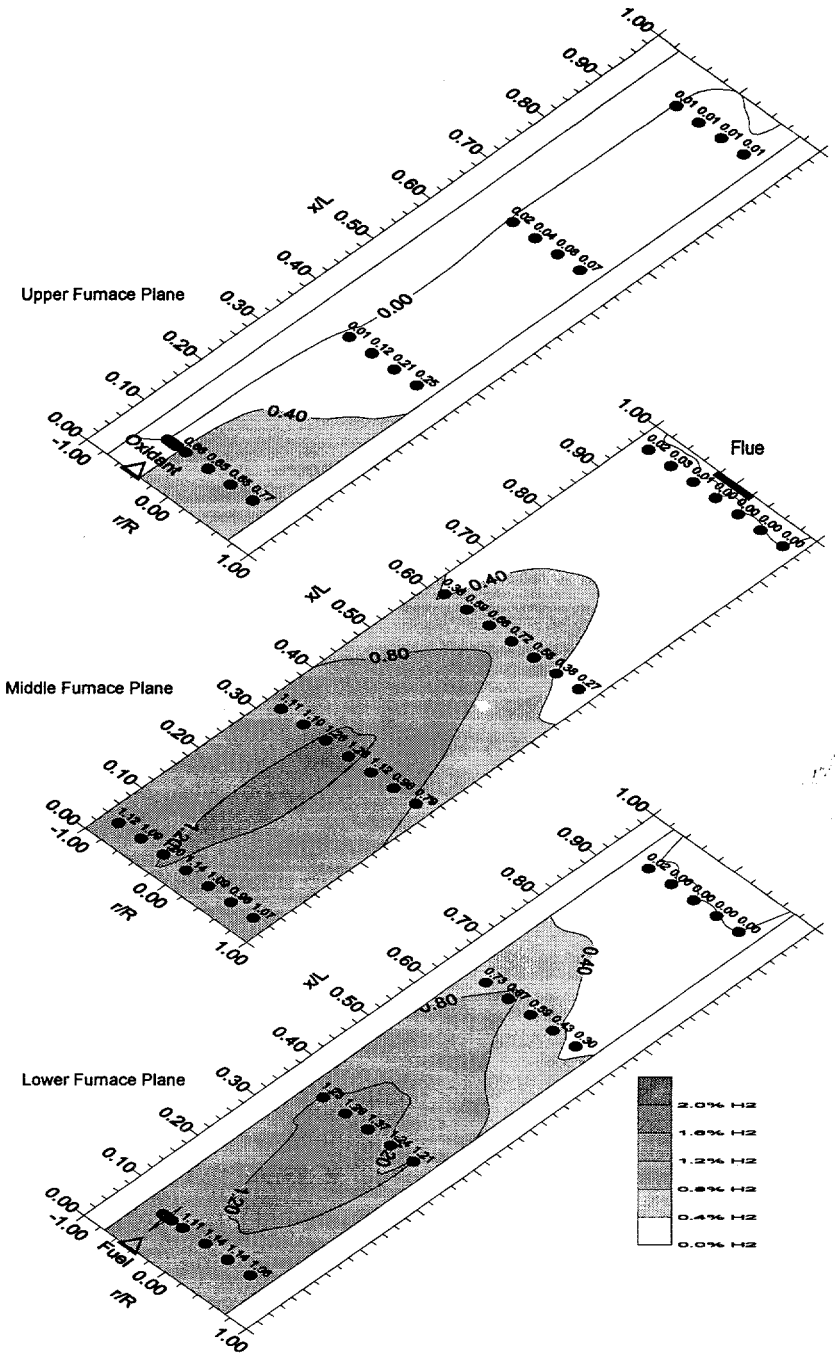

Fig. 33. Hydrogen concentration measurements (% vol. wet) as a function of furnace location for the co-firing burner arrangement F6F-O1F. The solid circles represent the measurement locations with the measured H_2 values listed next to them. The contours were interpolated from the measurements.

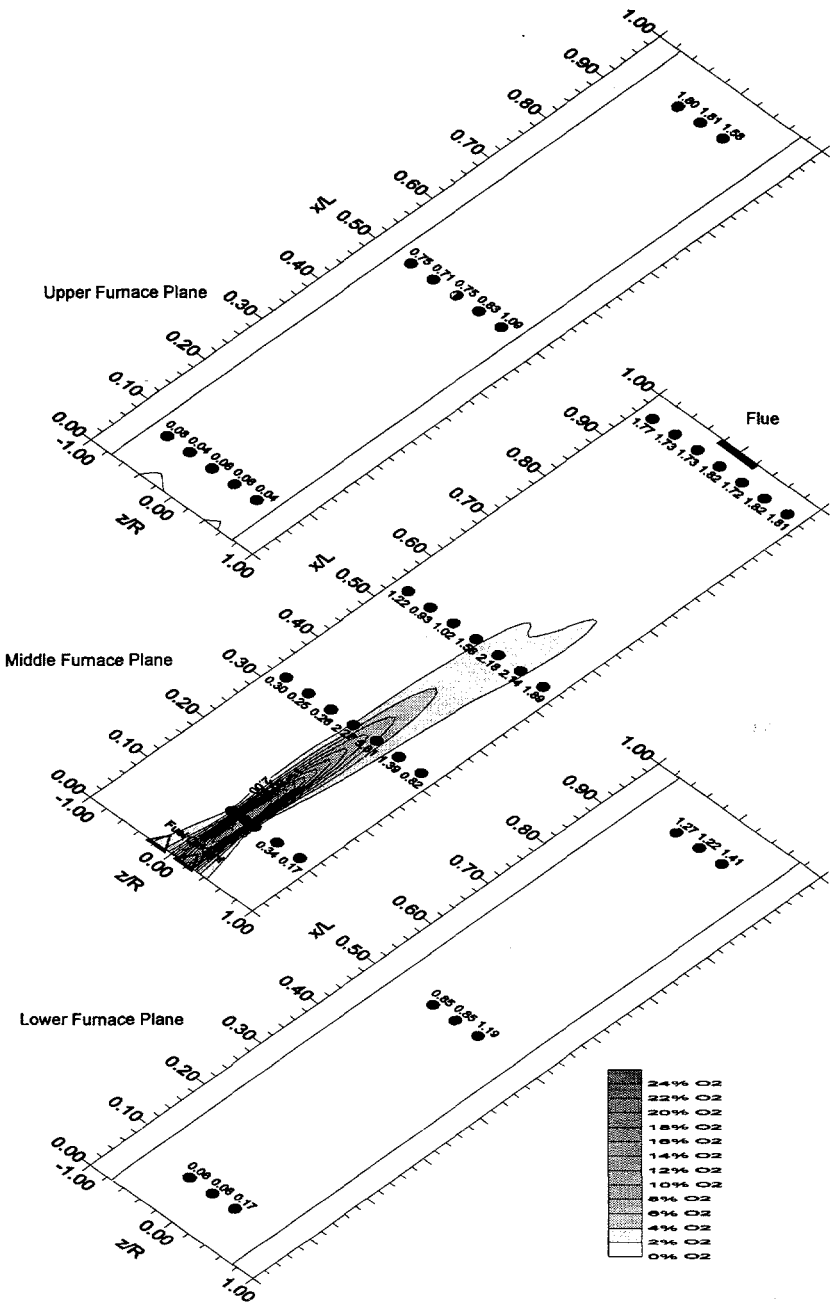

Fig. 34. Oxygen concentration measurements (% vol. wet) as a function of furnace location for the co-firing burner arrangement F4FL-O4FR. The solid circles represent the measurement locations with the measured O_2 values listed next to them. The contours were interpolated from the measurements.

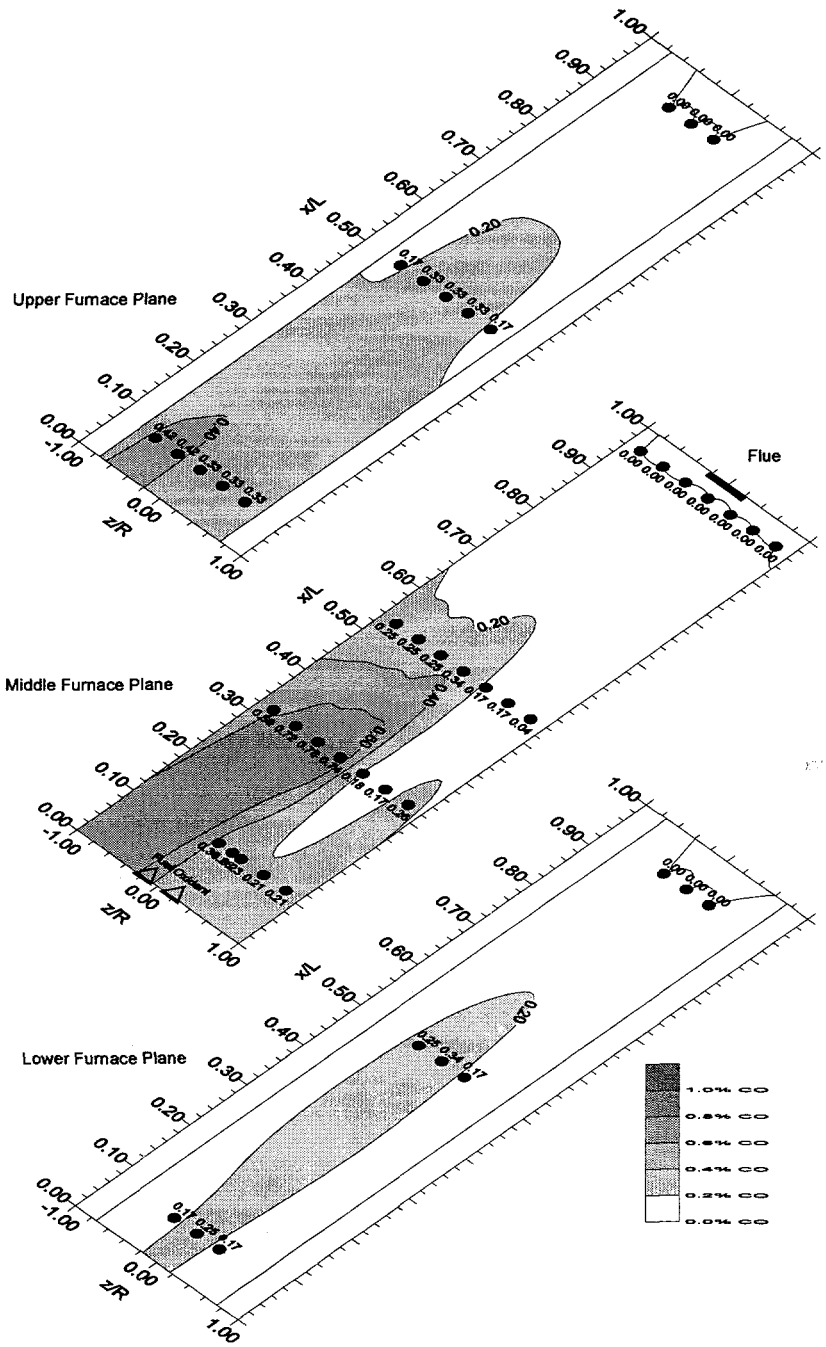

Fig. 35. Carbon monoxide concentration measurements (% vol. wet) as a function of furnace location for the co-firing burner arrangement F4FL-O4FR. The solid circles represent the measurement locations with the measured CO values listed next to them. The contours were interpolated from the measurements.

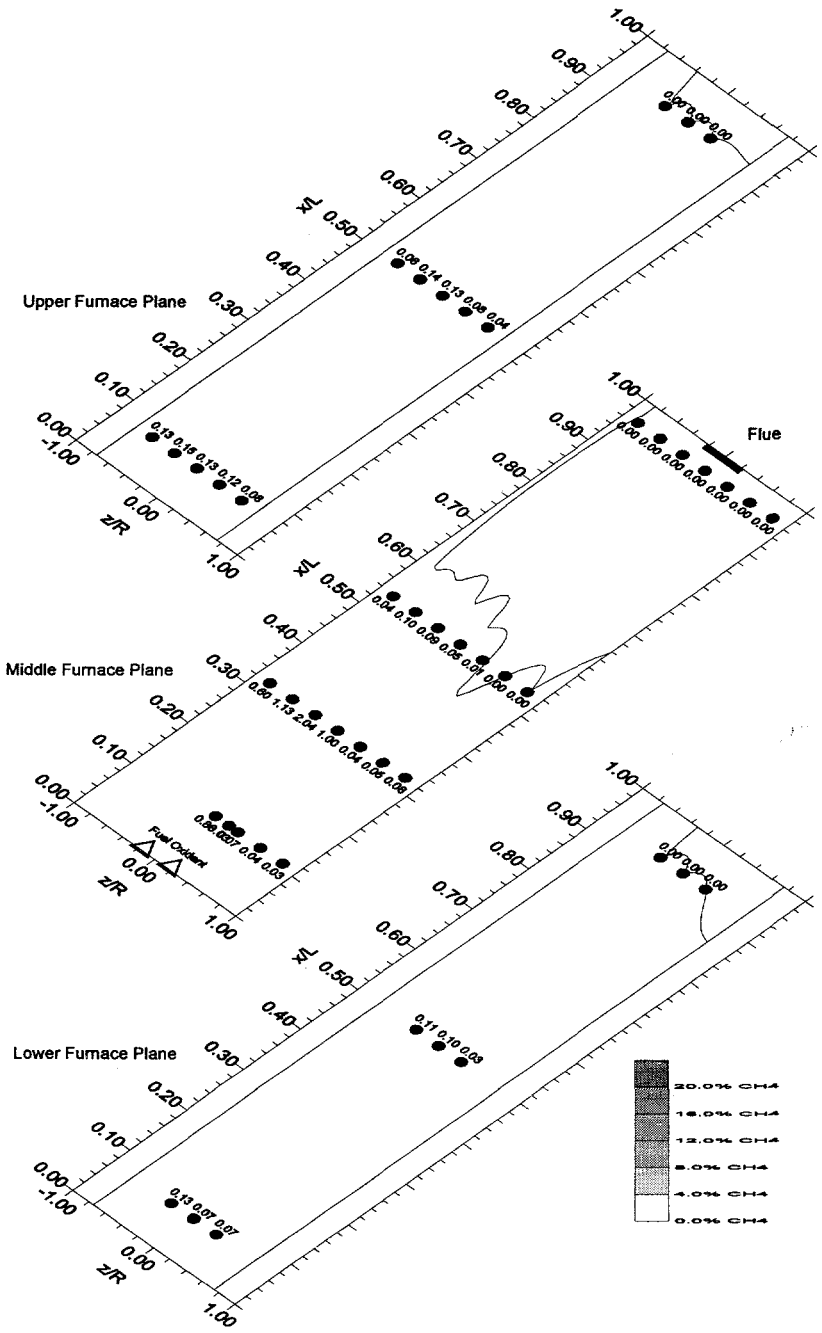

Fig. 36. Methane concentration measurements (% vol. wet) as a function of furnace location for the co-firing burner arrangement F4FL-O4FR. The solid circles represent the measurement locations with the measured CH_4 values listed next to them. The contours were interpolated from the measurements.

the front half of the furnace; however, this spread is not as encompassing as observed for the F6F-O1F arrangement (see Fig. 31). It is also interesting to note that the NO_x emissions for the F4FL-O4FR arrangement were higher than cases similar to the F6F-O1F arrangement.

Species measurements for the burner arrangement F6F-O7R (opposed-firing case) were taken, with information pertaining to the oxygen distribution within the furnace shown in Fig. 37. For this burner arrangement, the fuel and oxidant streams were directly opposed to each other. Within the lower furnace plane, the measured oxygen concentration is relatively high in the vicinity of the oxygen lance. For this case, the measured oxygen concentration at the flue was 2.53% (vol. wet). Note that oxygen is present in the vicinity of the fuel lance (2.72%). This phenomenon was not observed for the previously discussed co-firing burner arrangements, in which very little oxygen was present in the vicinity of the fuel jet (see Figs. 28 and 34).

In the middle furnace plane, the oxygen levels are somewhat similar with high oxygen concentrations near the front face of the furnace ($x/L \sim 0$). The trend of higher oxygen levels on opposite sides of the furnace from the oxidant lance arose quite frequently during the furnace probing tests. For example, the upper furnace plane has oxygen concentrations which are higher at $x/L \sim 0$ than near the flue, $x/L \sim 1$. Note that very little CO (Fig. 38) and CH_4 (Fig. 39) were measured within the furnace for this burner arrangement, which is in sharp contrast to the co-firing measurement results. In general, the F6F-O7R arrangement was characterized by higher NO_x emissions than the F6F-O1F arrangement.

The final burner arrangement in which detailed species measurements were made within the furnace was F6F-O1R. For this case, the fuel and oxidant lances were on opposite sides of the furnace, and diagonally-opposed. Measurements of oxygen concentration within the furnace along with interpolated oxygen contours for three furnace planes are shown in Fig. 40.

The oxygen lance delivers oxygen into the furnace in the upper furnace plane. High oxygen concentrations were evident near the oxygen lance. Once again, higher oxygen levels were measured along the opposite furnace wall, $x/L \sim 0$, from where the oxygen lance was located. The measured oxygen concentration at the flue was 2.15% (vol. wet). A rather high concentration of oxygen was evident in the vicinity of the fuel jet (5.40%). Measurements of CO and CH_4 for this case are given in Figs. 41-42.

The in-furnace oxygen distribution for both opposed-firing cases were similar, and different from the co-firing cases discussed earlier. For the F6F-O1F case, the measured oxygen levels rarely exceeded the oxygen concentration in the flue, whereas both opposed-firing cases (F6F-O7R and F6F-O1R) have regions of high oxygen levels. It was also earlier noted that NO_x emissions were typically higher for the opposed-firing cases than the co-firing cases (see Figs. 22-23). Thus, it is evident that higher NO_x levels result when the fuel stream is in a higher oxygen-content environment, as expected.

5.2.8 Furnace Pressure Measurements

The stability associated with the DOC burner was evaluated by making furnace pressure measurements as a function of furnace temperature and burner arrangement. Before attempting any measurements, the resonant or natural frequencies associated with the laboratory-scale furnace were calculated assuming a flue gas atmosphere within the furnace

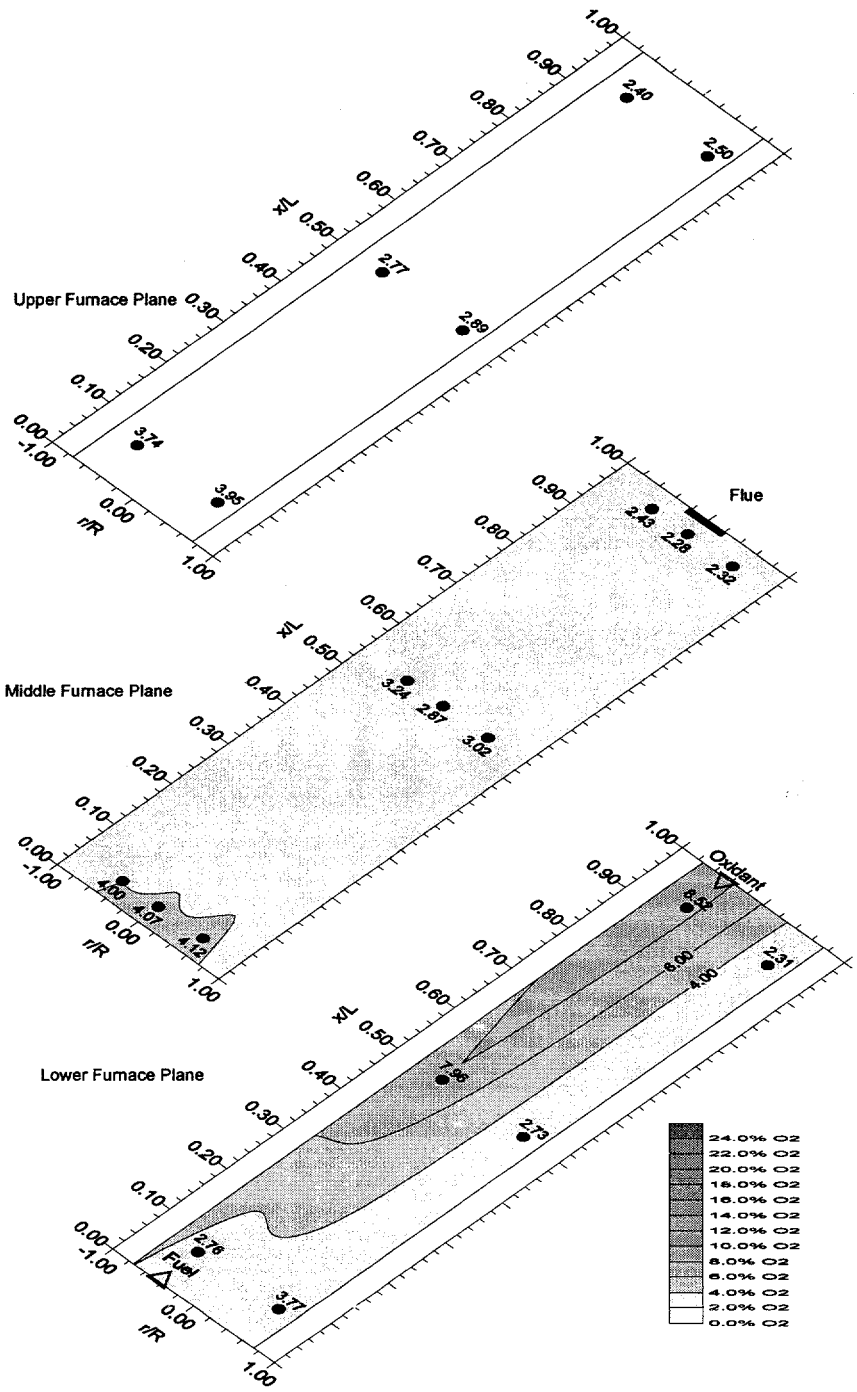

Fig. 37. Oxygen concentration measurements (% vol. wet) as a function of furnace location for the opposed-firing burner arrangement F6F-O7R. The solid circles represent the measurement locations with the measured O_2 values listed next to them. The contours were interpolated from the measurements.

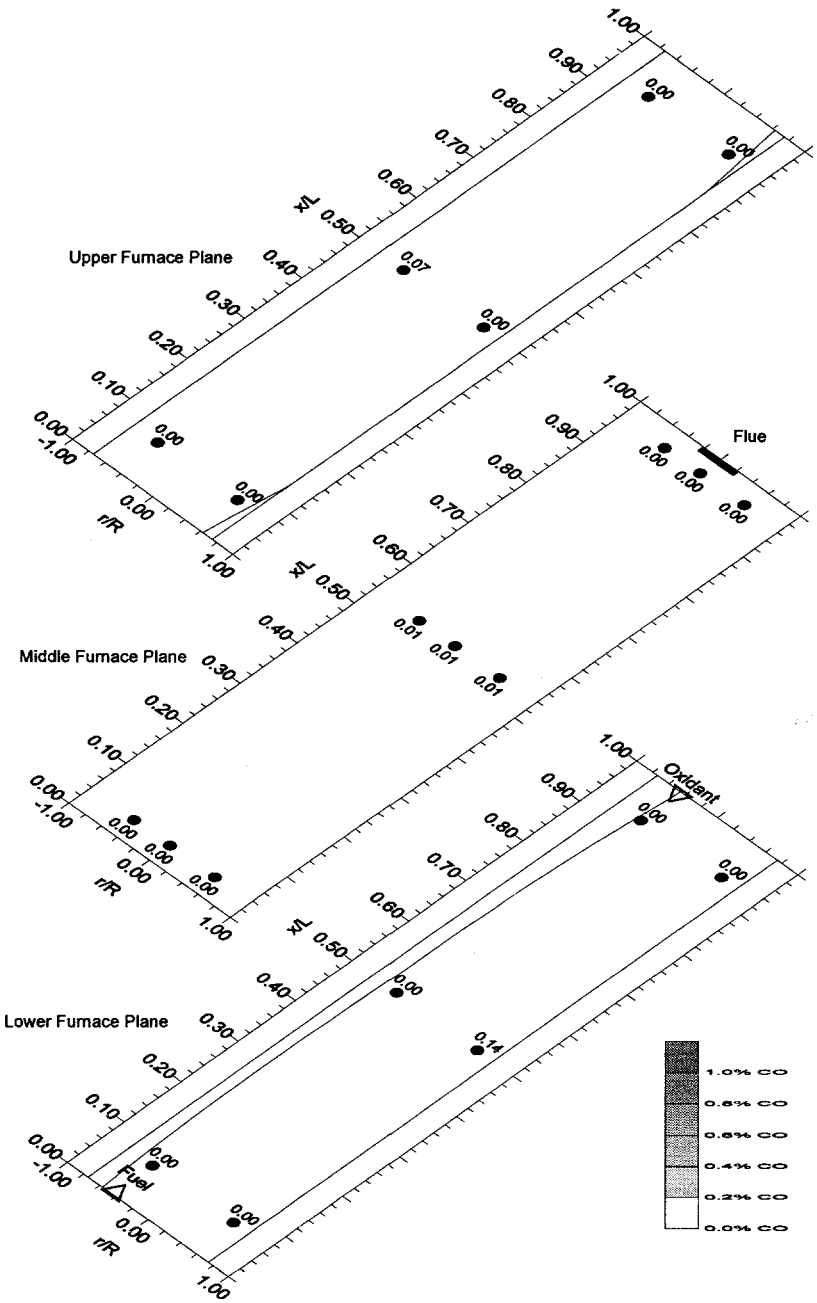

Fig. 38. Carbon monoxide concentration measurements (% vol. wet) as a function of furnace location for the opposed-firing burner arrangement F6F-O7R. The solid circles represent the measurement locations with the measured CO values listed next to them. The contours were interpolated from the measurements.

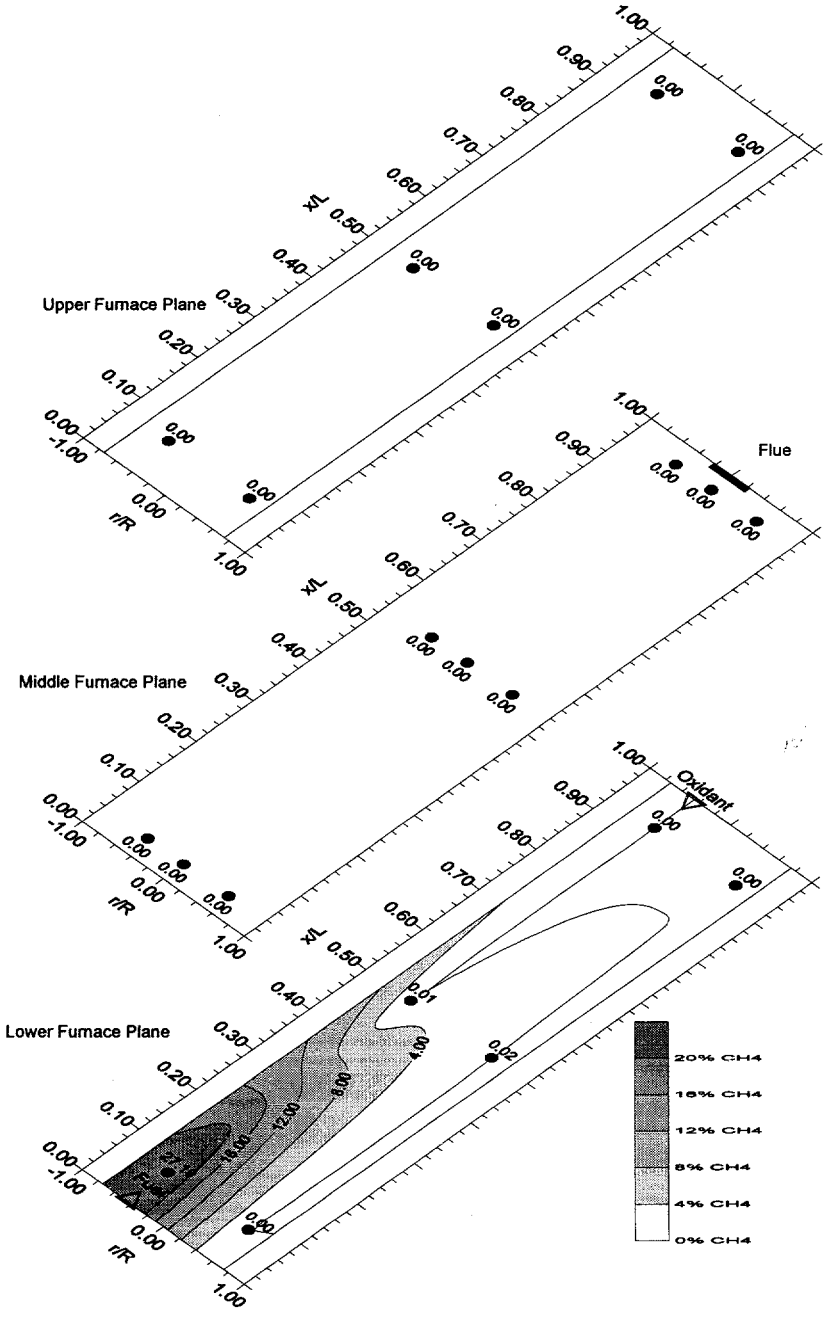

Fig. 39. Methane concentration measurements (% vol. wet) as a function of furnace location for the opposed-firing burner arrangement F6F-O7R. The solid circles represent the measurement locations with the measured CH_4 values listed next to them. The contours were interpolated from the measurements.

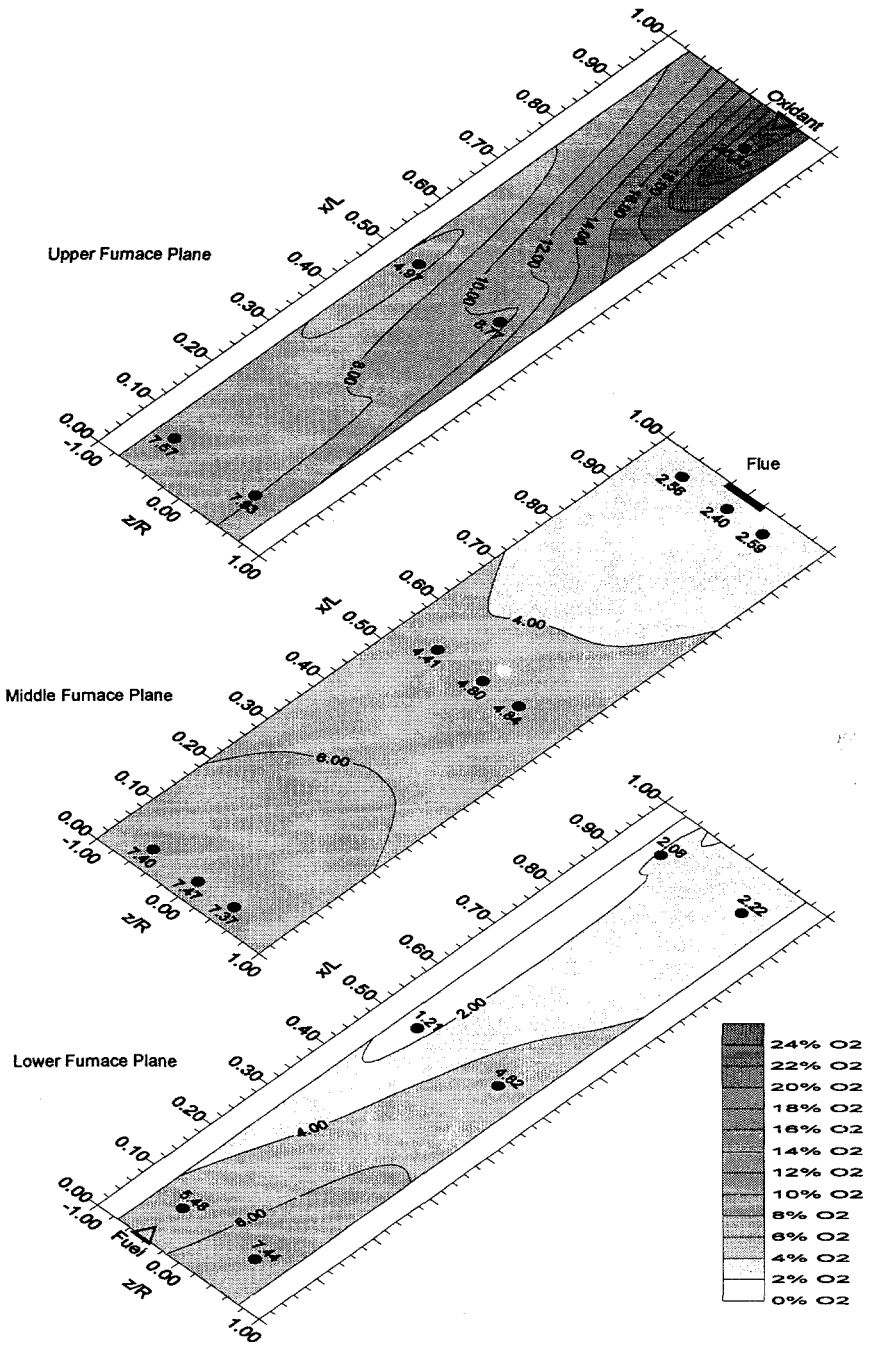

Fig. 40. Oxygen concentration measurements (% vol. wet) as a function of furnace location for the opposed-firing burner arrangement F6F-O1R. The solid circles represent the measurement locations with the measured O_2 values listed next to them. The contours were interpolated from the measurements.

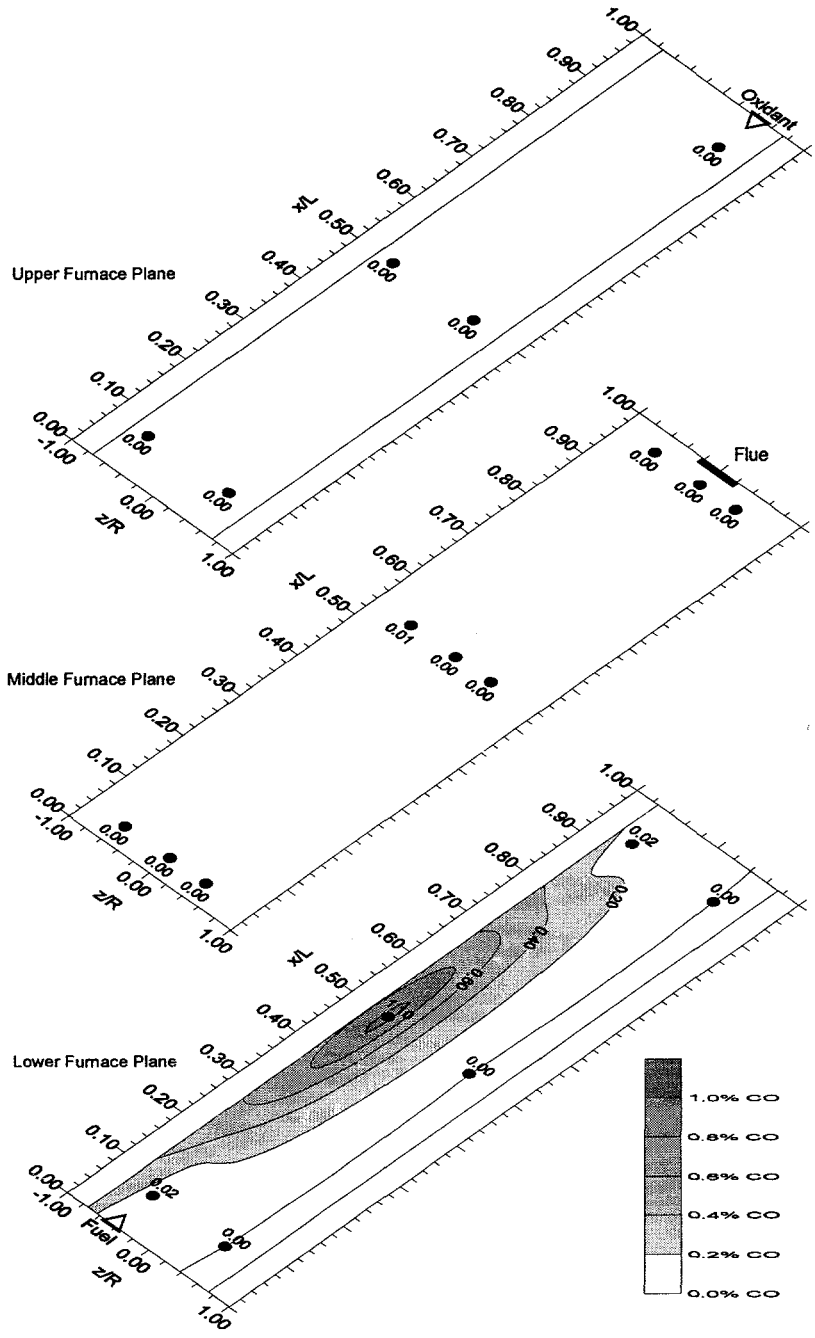

Fig. 41. Carbon monoxide concentration measurements (% vol. wet) as a function of furnace location for the opposed-firing burner arrangement F6F-O1R. The solid circles represent the measurement locations with the measured CO values listed next to them. The contours were interpolated from the measurements.

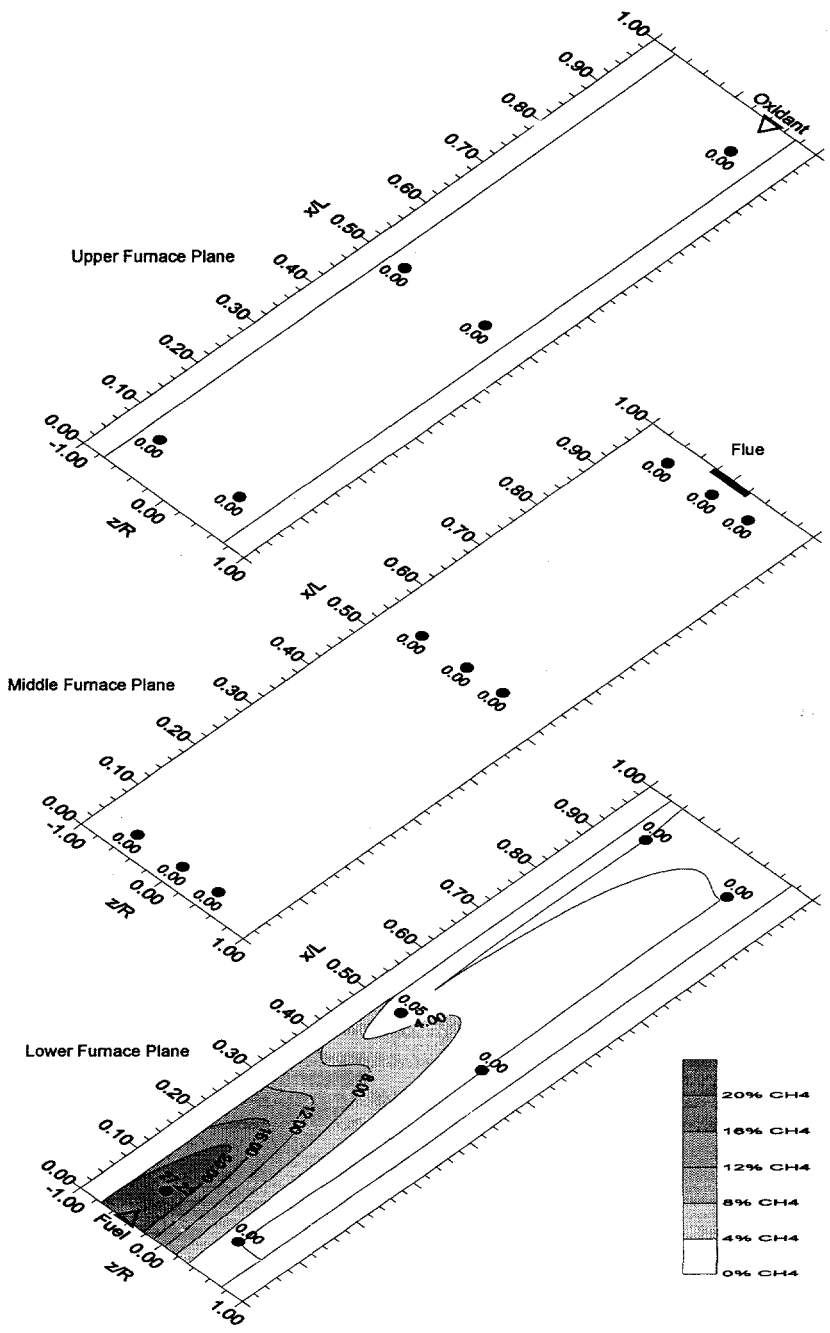

Fig. 42. Methane concentration measurements (% vol. wet) as a function of furnace location for the opposed-firing burner arrangement F6F-O1R. The solid circles represent the measurement locations with the measured CH_4 values listed next to them. The contours were interpolated from the measurements.

(32.5% CO_2, 65% H_2O, 2.5% O_2) and gas temperatures of 1346 K (1964°F) and 1513 K (2264°F), with the results shown in Table 17. Recall that n_z denotes the order of the longitudinal modes, m the tangential modes and n the radial modes. Note that only a selection of chamber resonant frequencies are listed in Table 17.

Table 17. Laboratory-Scale Furnace Resonant Modes

Longitudinal (n_z)	Tangential (m)	Radial (n)	f (1346 K), Hz	f (1513 K), Hz
0	0	0	0	0
1	0	0	116	123
2	0	0	232	245
3	0	0	347	368
0	1	0	475	503
1	1	0	489	518
2	1	0	528	560
3	1	0	588	624
0	2	0	788	835
1	2	0	796	844
2	2	0	821	870
3	2	0	861	913
0	0	1	988	1,048
1	0	1	995	1,055
2	0	1	1,015	1,076
3	0	1	1,048	1,111
0	3	0	1,084	1,149
1	3	0	1,090	1,155
2	3	0	1,108	1,175
3	3	0	1,138	1,206
1	1	1	1,380	1,463
2	1	1	1,394	1,478
3	1	1	1,418	1,504
1	2	1	1,734	1,838

Furnace pressure measurements were made for two co-firing arrangements, F4FL-O4FR and F6F-O1F at a furnace temperature of 1346 K (1964°F). In addition, furnace pressure measurements for the F6F-O1F arrangement were made at a furnace temperature of 1513 K (2264°F). The furnace pressure oscillations were sampled at 10 kHz over 0.82 s using the PCB 106B pressure transducer. A fast-Fourier transform (FFT) computer program [85, 86] was used to reduce the pressure-time data. Several amplitude-frequency plots for the aforementioned conditions are shown in Figs. 43a-c. Due to the adapters used to attach the

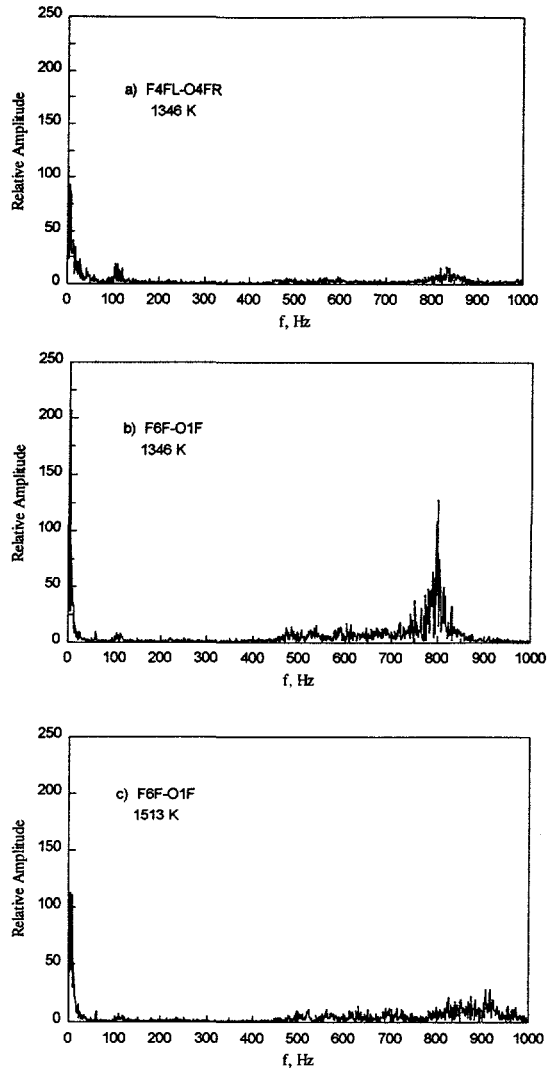

Fig. 43a-c. Frequency content of furnace pressure measurements as a function of burner arrangement and furnace wall temperature.

transducer to the furnace, amplitude losses were expected, thus the amplitude values given in Figs. 43a-c are on a relative scale.

Upon reviewing Figs. 43a-c, there is evidence of low frequency (< 15 Hz), high-amplitude patterns within the furnace, frequencies significantly lower than the calculated resonant modes associated with the laboratory-scale furnace (see Table 17). These low frequency peaks indicate the presence of large-scale, periodic mixing cells. Careful inspection of Figs. 43a-c revealed the presence of a few select chamber resonant modes. In all three plots, a peak was detected at about 110 Hz, which is close to the calculated first longitudinal mode (n_z=1, m=0, n=0). A series of strong peaks between 800-900 Hz were also evident in

all three cases. Specifically, the largest of these peaks were at 833 Hz for the F4FL-O4FR/1346 K case, 800 Hz for the F6F-O1F/1346 K case and 915 Hz for the F6F-O1F/1513 K case. Based on the resonant mode calculations, the aforementioned measured frequencies appear to be combined mode(s) involving the second tangential mode and the first to third longitudinal modes.

Upon comparing each of the different cases shown in Figs. 43a-b, the F4FL-O4FR arrangement resulted in a more stable combustion event as compared to the F6F-O1F arrangement based on the amplitudes of the strongest peaks. This is not unexpected, since the separation distance of the F4FL-O4FR arrangement was 152 mm (6 in.) compared to 610 mm (24 in.) for the F6F-O1F arrangement. The F4FL-O4FR arrangement resembles a more traditional burner. Intuitively, a large separation distance between fuel and oxidant injection points would result in a less stable combustion event, an observation that is born out in the measurements.

The effect of furnace temperature on combustion stability for burner arrangement F6F-O1F was surmised from the results shown in Figs. 43b-c. In fact, an increase in furnace temperature leads to an increase in combustion stability based on the reduction in amplitude by at least a factor of two of the various peaks.

Clearly, examining in detail any furnace pressure oscillations can lead to useful information characteristic of the combustion process associated with a particular burner. The results presented here are by no means complete, and should be expanded to other burner arrangements (e.g., opposed-firing cases) and further analyzed to isolate the source of the both the low-frequency (< 15 Hz) and high-frequency peaks.

6.0 SUMMARY

The project goal is to achieve an economically viable burner that produces NO_x emissions at the single-digit ppm level under typical high-temperature furnace (e.g., steel reheat furnace) conditions, in addition to meeting other constraints, such as furnace temperature uniformity. To meet this objective, a series of fundamental and applied tests were undertaken to develop the dilute oxygen combustion (DOC) burner. In addition, the economic advantages/disadvantages and the potential market penetration of the DOC burner were addressed in a market survey.

The fundamental aspects of the burner development project involved examining the flame characteristics of a natural gas turbulent jet in a high-temperature ($\sim$1366 K) oxidant (7-27% O_2 vol. wet). Specifically, the mass entrainment rate, the flame lift-off height, the velocity field and major species field of the jet were evaluated as a function of surrounding-gas temperature and composition. The measured entrainment rate of the fuel jet decreased with increasing oxygen content in the surrounding high-temperature oxidant, and was well represented by the d^+ scaling correlation found in the literature. The measured flame lift-off height decreased with increasing oxygen content and increasing temperature of the surrounding gas. An increase in surrounding-gas oxygen content and/or temperature inhibited the velocity decay within the jet periphery as a function of axial distance as compared to isothermal turbulent jets. The velocity measurements were only broadly represented by the d^+ scaling correlation.

Several DOC burner configurations were tested in a laboratory-scale furnace at a nominal firing rate of 185 kW ($\sim$0.63 MMBtu/h). The flue gas composition was recorded as a function of furnace nitrogen content, furnace temperature, burner geometric arrangement, firing rate, and fuel injection velocity. NO_x emissions increased with increasing furnace nitrogen content and furnace temperature, but remained relatively insensitive to variations in fuel injection velocity and firing rate. A NO_x emission level of $5 \cdot 10^{-3}$ g/MJ (10 ppm-air equivalent at 3% O_2 dry) has been achieved using the DOC burner with natural gas and oxygen as the reactants for a furnace temperature of 1533 K (2300°F) and a furnace nitrogen content of 40%. Note that nitrogen was injected separately into the furnace to simulate furnace leakage. In fact, NO_x emissions below $5 \cdot 10^{-4}$ g/MJ (1 ppm-air equivalent at 3% O_2 dry) are possible using the oxy-fuel DOC burner for minimal furnace nitrogen levels (<1%) and for furnace temperatures less than 1533 K (2300°F). CO emissions were typically low (<35 ppm). Detailed in-furnace species measurements revealed the importance of the interior furnace circulation patterns, as influenced by fuel and oxidant injection schemes, on pollutant emissions. The combustion stability traits of several DOC burner arrangements were ascertained through furnace pressure measurements, with increased stability occurring as furnace temperature increased and as the separation distance between fuel and oxidant inputs decreased.

Based on current market conditions, oxy-fuel conversion of batch steel reheat furnaces with a DOC burner is justified on the basis of lower utility costs alone. However, conversion of continuous steel reheat furnaces, which are responsible for most steel production, requires additional economic incentives, such as further fuel savings, increased furnace productivity, or emission credits.

7.0 REFERENCES

[1] Kobayashi, H., "Segregated Zoning Combustion," U.S. Patent 5076779, December 31, 1991.

[2] *1994 AISI Annual Statistical Report*, AISI, Washington DC, pp. 84-85, 1995.

[3] Ibid., p. 83.

[4] *The Making, Shaping, and Treating of Steel*, W.T. Lankford, Jr., N.L. Samways, R.F. Craven, and H.E. McGannon, eds., Herbick and Held, Pittsburgh, pp.856-859, 1985.

[5] Kobayashi, H., "Oxygen Enriched Combustion System Performance Study - Vol. II - Market Assessment," DOE/ID/12597-3, U.S. Department of Energy, Idaho Falls, ID, p. 4, September 1988.

[6] *1994 AISI Annual Statistical Report*, op.cit., p. 79.

[7] *The Making, Shaping, and Treating of Steel*, op.cit., p. 129.

[8] Prabhu, D. U., and Cilione, P. F., "1990 Clean Air Act Amendments: Technical/ Economic Impact on U.S. Coke and Steelmaking Operations," *Iron and Steel Engineer*, pp. 33-43, January 1992.

[9] Reed, R. J., Combustion Handbook, 3rd Ed., Vol. I, North American Manufacturing, Cleveland, pp. 36-37, 1986.

[10] *1994 AISI Annual Statistical Report*, op.cit., p. 4.

[11] Ibid., p.73.

[12] *Directory of Iron and Steel Plants*, AISE, Pittsburgh, pp. 95-205, 1995.

[13] Farrell, L. M., Pavlack, T. T., and Rich, L., "Operating and Environmental Benefits of Oxy-Fuel Combustion in the Steel Industry," 12th PTD Conference Proceedings, ISS, Warrendale, PA, pp. 185-199, 1993.

[14] Erdman, T., "Bigger. Better. Faster. (And Smarter.)," *33 Metalproducing*, pp. 57-60, and 78, June 1996.

[15] Ritt, A., "The Benefits of Hot-Charging Slabs," *New Steel*, pp. 34-37 and 44, July 1996.

[16] Teng, H. and Huang, T.-S., "Control of NO_x Emissions through Combustion Modifications for Reheating Furnaces in Steel Plants," *Fuel*, Vol. 75 No. 2, pp. 149-155, 1996.

[17] Kobayashi, H., Silver, L. S., Kwan, Y., and Chen, S. L., "NO_x Emission Characteristics of Industrial Burners and Control Methods under Oxygen Enriched Combustion Conditions," presented at 9th Members Conference, International Flame Research Foundation, 1989.

[18] Anon., "High-Performance Low-NO_x Industrial Burner," Gas Research Institute Technical Brief, September 1995.

[19] Mieth, J. A. and Karell, M., "Emission Reduction Credits (ERC's)," *Environmental Engineers, Scientists and Planners*, Malcolm Pirnie, Inc., 1996.

[20] Bluestein, J., "Air Regulatory Outlook for Combustion Processes," American Flame Research Committee International Symposium, Baltimore, MD., Sept. 30-Oct. 2, 1996.

[21] Ricou, F. P. and Spalding, D. B., "Measurements of Entrainment by Axisymmetrical Turbulent Jets," *Journal of Fluid Mechanics*, Vol. 9, pp. 21-32, 1961.

[22] Dahm, W. J. A. and Dimotakis, P. E., "Measurements of Entrainment and Mixing in Turbulent Jets," *AIAA Journal*, Vol. 25, No. 9, pp. 1216-1223, September 1987.

[23] Liepmann, D. and Gharib, M., "The Role of Streamwise Vorticity in the Near-Field Entrainment of Round Jets," *Journal of Fluid Mechanics*, Vol. 245, pp. 643-668, 1992.

[24] Trabold, T. A., Esen, E. B. and Obot, N. T., "Entrainment by Turbulent Jets Issuing From Sharp-Edged Inlet Round Nozzles," *Transactions of the ASME*, Vol. 109, pp. 248-254, Sept. 1987.

[25] Becker, H. A. and Yamazaki, S., "Entrainment, Momentum Flux and Temperature in Vertical Free Turbulent Diffusion Flames," *Combustion and Flame*, Vol. 33, pp. 123-149, 1978.

[26] Dahm, W. J. A., Personal communication, October 1, 1996.

[27] Delichatsios, "Transition from Momentum to Buoyancy-Controlled Turbulent Jet Diffusion Flames and Flame Height Relationships," *Combustion and Flame*, Vol. 92, pp. 349-364, 1993.

[28] Zhou, X. C. and Gore, J. P., "Air Entrainment Flow Field Induced by a Pool Fire," *Combustion and Flame*, Vol. 100, pp. 52-60, 1995.

[29] Delichatsios, M. A., "Air Entrainment into Buoyant Jet Flames and Pool Fires," *Combustion and Flame*, Vol. 70, pp. 33-46, 1987.

[30] Cetegen, B. M., Zukoski, E. E. and Kubota, T., "Entrainment in the Near and Far Field of Fire Plumes," *Combustion Science and Technology*, Vol. 39, pp. 305-331, 1984.

[31] Weckman, E. J. and Sobiesiak, A., "The Oscillatory Behaviour of Medium-Scale Pool Fires," 22nd Symposium (International) on Combustion, The Combustion Institute, pp. 1299-1310, 1988.

[32] Gebhart, B., Jaluria, Y., Mahajan, R. L. and Sammakia, B., Buoyancy-Induced Flows and Transport - Reference Edition, Hemisphere Publishing Corp., New York, 1988.

[33] Briggs, D. A., Ferziger, J. H., Koseff, J. R. and Monismith, S. G., "Entrainment in a Shear-Free Turbulent Mixing Layer," *Journal of Fluid Mechanics*, Vol. 310, pp. 215-241, 1996.

[34] Soteriou, M. C., Knio, O. M. and Ghoniem, A. F., "Manipulation of the Growth Rate of a Variable Density, Spatially Developing Mixing Layer via External Modulation," AIAA paper 91-0081, 29th Aerospace Sciences Meeting, Reno, NV, Jan. 7-10, 1991.

[35] Lutz, A. E., "Chemical Kinetics of Air Toxics and NO_x in a Turbulent Diffusion Flame Burner," American Flame Research Committee International Symposium, Monterey, CA, Oct. 15-18, 1995.

[36] Beèr, J. M and Chigier, N. A., Combustion Aerodynamics, Applied Science Publishers Ltd., London, p. 17, 1972.

[37] Dahm, W. J. A., Personal communication, November 21, 1996.

[38] Kalghatgi, G. T., "Lift-Off Heights and Visible Lengths of Vertical Turbulent Jet Diffusion Flames in Still Air," *Combustion Science and Technology*, Vol. 41, pp. 17-29, 1984.

[39] Takahashi, F. and Schmoll, W. J., "Lifting Criteria of Jet Diffusion Flames,"23rd Symposium (International) on Combustion, The Combustion Institute, pp. 677-683, 1990.

[40] Vanquickenborne, L. and Van Tiggelen, A., "The Stabilization Mechanism of Lifted Diffusion Flames," *Combustion and Flame*, Vol. 10, pp. 59-69, 1966.

[41] Janicka, J. and Peters, N., "Prediction of Turbulent Jet Diffusion Flame Lift-Off Using a PDF Transport Equation," 19th Symposium (International) on Combustion, The Combustion Institute, pp. 367-374, 1982.

[42] Muñiz, L. and Mungal, M. G., "Velocity Measurements in Lifted-Jet Diffusion Flames," Paper 96F-113, 1996 Western States Section Meeting of The Combustion Institute, Univ. of Southern California, Oct. 28-29, 1996.

[43] Kalghatgi, G. T., "Blow-Out Stability of Gaseous Jet Diffusion Flames. Part I: Still Air," *Combustion Science and Technology*, Vol. 26, pp. 233-239, 1981.

[44] Dahm, W. J. A. and Dibble, R. W., "Coflowing Turbulent Jet Diffusion Flame Blowout," 22nd Symposium (International) on Combustion, The Combustion Institute, pp. 801-808, 1988.

[45] Mastorakos, E., Taylor, A.M.K.P., and Whitelaw, J.H., "Extinction of Turbulent Counterflow Flames with Reactants Diluted by Hot Products," *Combustion and Flame*, Vol. 102, pp. 101-114, 1995.

[46] Peters, N., "Partially Premixed Diffusion Flamelets in Non-Premixed Turbulent Combustion," 20th Symposium (International) on Combustion, The Combustion Institute, pp. 353-360, 1984.

[47] Tieszen, S. R., Stamps, D. W. and O'Hern, T. J., "A Heuristic Model of Turbulent Mixing Applied to Blowout of Turbulent Jet Diffusion Flames," *Combustion and Flame*, Vol. 106, pp. 442-466, 1996.

[48] Pitts, W. M., "Importance of Isothermal Mixing Process to the Understanding of Lift-Off and Blowout of Turbulent Jet Diffusion Flames," *Combustion and Flame*, Vol. 76, pp. 197-212, 1989.

[49] Schlichting, H., Boundary-Layer Theory, McGraw-Hill, 7th Ed., NY, pp. 747-750, 1979.

[50] Turns, S. R., An Introduction to Combustion - Concepts and Applications, McGraw-Hill, Inc., NY, pp. 375-377, 1996.

[51] Durrani, T. S. and Greated, C. A., Laser Systems in Flow Measurement, Plenum Press, 1977.

[52] Durst, F., Melling, A. and Whitelaw, J.H., Principles and Practice of Laser-Doppler Anemometry, Academic Press, Inc., NY, 1981.

[53] Combustion Measurements, N. A. Chigier, ed., Hemisphere Publishing Corp., Philadelphia, pp. 21-50, 1991.

[54] Takagi, T., Shin, H. D. and Ishio, A., "Properties of Turbulence in Turbulent Diffusion Flames," *Combustion and Flame*, Vol. 40, pp. 121-140, 1981.

[55] Takagi, T., Shin, H. D. and Ishio, A., "A Study on the Structure of Turbulent Diffusion Flame: Properties of Fluctuations of Velocity, Temperature, and Ion Concentration," *Combustion and Flame*, Vol. 41, pp. 261-271, 1981.

[56] Sislian, J. P., Jiang, L.-Y. and Cusworth, R. A., "Laser Doppler Velocimetry Investigation of the Turbulence Structure of Axisymmetric Diffusion Flames," Progress in Energy and Combustion Science, N. A. Chigier, ed., Vol. 14, pp. 99-146, 1988.

[57] Dugue, J. and Weber, R., "Laser Velocimetry in Semi-Industrial Natural Gas, Oil and Coal Flames by Means of a Water-Cooled LDV Probe," 6th International Symposium on Application of Laser in Anemometry in Fluid Mechanics, Lisbon, Portugal, 1992.

[58] Bowman, C. T., "Control of Combustion-Generated Nitrogen Oxide Emissions: Technology Driven By Regulation," 24th Symposium (International) on Combustion, The Combustion Institute, pp. 859-878, 1992.

[59] Irwin, J. G., and Williams, M. L., "Acid Rain: Chemistry and Transport," *Environmental Pollution*, Vol. 50, pp. 29-59, 1988.

[60] Turns, S. R., An Introduction to Combustion - Concepts and Applications, McGraw Hill, Inc., New York, pp. 472-513, 1996.

[61] Miller, J. A and Bowman, C. T., "Mechanism and Modeling of Nitrogen Chemistry in Combustion," Prog. Energy Combust. Sci., Vol. 15, Pergamon Press, pp. 287-338, 1989.

[62] Fenimore, C. P., "Formation of Nitric Oxide in Premixed Hydrocarbon Flames," 13th Symposium (International) on Combustion, The Combustion Institute, pp. 373-380, 1970.

[63] Turns, S. R. and Bandaru, R. V., "Oxides of Nitrogen Emissions from Turbulent Hydrocarbon/Air Jet Diffusion Flames," GRI Report 92/0470, 1992.

[64] Driscoll, J. F. and Dahm, W. J. A., "Diffusion and Reaction Layer Structure and NO_x Reduction in Turbulent Natural Gas Flames," GRI Report 91/0144, 1991.

[65] Turns, S. R., An Introduction to Combustion - Concepts and Applications, McGraw Hill, Inc., New York, pp. 475-480, 1996.

[66] Putnum, A. A., Combustion Driven Oscillations in Industry, Elsevier, 1971.

[67] Richards, G. A., Gemmen, R. S. and Yip, M. J., "A Test Device for Premixed Gas Turbine Combustion Oscillations," DOE/METC Technical Note 1027, March 1996.

[68] Liquid Propellant Rocket Instability, D. T. Harrje and F. H. Reardon, eds., NASA SP-194, 1972.

[69] Morse, P. M., Vibration and Sound, American Institute of Physics for the Acoustical Society of America, 1976, pp. 397-399.

[70] Folsom, B. A. and Courtney, C. W., "Chemiluminescent Measurement of Nitric Oxide in Combustion Products," Energy and Environmental Research Corporation, Santa Ana, CA 92705.

[71] Matthews, R. D., Sawyer, R. F. and Schefer, R. W., "Interferences in Chemiluminescent Measurement of NO and NO_2 Emissions from Combustion Systems," *Environmental Science and Technology*, Vol. 11, No. 12, pp. 1092-1096, November 1977.

[72] Clemens, N. T. and Paul, P. H., "Effects of Heat Release on the Near Field Flow Structure of Hydrogen Jet Diffusion Flames," *Combustion and Flame*, Vol. 102, pp. 271-284, 1995.

[73] Takeno, T., "Transition and Structure of Jet Diffusion Flames," Invited Lecture, 25th Symposium (International) on Combustion, The Combustion Institute, 1994.

[74] Yamashita, H., Kushida, G. and Takeno, T., "A Numerical Study of the Transition of Jet Diffusion Flames," *Proceedings of the Royal Society of Londan A*, 431, p. 301, 1990.

[75] Chen, L.-D., Roquemore, W. M., Gross, L. P., and Vilimpoc, V., "Voriticity Generation in Jet Diffusion Flames," *Combustion Science and Technology*, Vol. 77, pp. 41-57, 1991.

[76] Takagi, T., Shin, H.-D. and Ishio, A., "Local Laminarization in Turbulent Diffusion Flames," *Combustion and Flame*, Vol. 37, pp. 163-170, 1980.

[77] Dring, R. P., "Sizing Criteria for Laser Anemometry Particles," *Journal of Fluids Engineering*, Vol. 104, March, pp. 15-17, 1982.

[78] Philippart, K. D., "Diagnostic Developments for Velocity and Temperature Measurements in Uni-Element Rocket Environments," Master's Thesis, Department of Aerospace Engineering, The Pennsylvania State University, pp. 68-85, 1995.

[79] Anon., Aerometrics Phase Doppler Particle Anaylzer System Manual, 1996.

[80] Craig, R. R., Nejad, A. S., Hahn, E. Y. and Schwartzkopf, K. G., "Approach for Obtaining Unbiased Laser Doppler Velocimetry Data in Highly Turbulent Flows," *Journal of Propulsion and Power*, Vol. 2, Nov.-Dec., 1986. pp. 541-545.

[81] Winter, A.R., Graham, L. J. W. and Bremhorst, K., "Effects of Time Scales on Velocity Bias in LDA Measuremnets Using Sample and Hold Processing," *Experiments in Fluids*, Vol. 11, 1991, pp. 147-152.

[82] Johnson, D. A., Modarress, D. and Owen, F. K., "An Experimental Verification of Laser-Velocimeter Sampling Bias and Its Correction," *Journal of Fluids Eng.*, Vol. 106, Sept., 1988, pp. 5-12.

[83] Surfer for Windows User's Guide, Golden Software, Inc., 1994.

[84] Cressie, N. A. C., "The Origins of Kriging," *Mathematical Geology*, Vol. 22, pp. 239-252.

[85] Press, W. H., Flannery, B. P., Teukolsky, S. A. and Vetterling, W. T., Numerical Recipes. The Art of Scientific Computing, Cambridge University Press, NY, 1986, pp. 381-453.

[86] Vetterling, W. T., Teukolsky, S. A., Press, W. H. and Flannery, B. P., Numerical Recipes Example Book (FORTRAN), Cambridge University Press, NY, 1985, pp. 120-131.